A SEARCH FOR HEAVY NEUTRINO DECAYS IN A NEUTRINO BEAM

A DESSERTATION

by

Yoshitake YAMAGUCHI

1990

Submitted to the Faculty of Science of Osaka University
in Partial Fulfillment of the Requirement
for the Degree of Philosophy

ACKNOWLEDGMENTS

This neutrino experiment has been performed by many people since 1978 while I joined in 1984. I would like to extend a general thank you to all of the collaborators at BNL, Brown, KEK, Osaka, Stony Brook, Pennsylvania and Tokyo(INS), who worked on the construction, debugging and maintenance of the detector and make this experiment successful. I would also like to thank the Accelerator Department personnel who worked hard to deliver the neutrino beam to our detector, the Applied Mathematics Department personnel who worked hard to handle a great many tapes.

Most of all I would like to thank my thesis adviser Professor Y.Nagashima, who introduced me to this experiment and encouraged me to accomplish this work.

I would especially like to thank to Prof. Yoichiro Suzuki who worked most closely with me throughout my three years Ph.D course. His encouragement and helpful advises developed my ability as a high energy physicist. Dr. Yoshimasa Kurihara who worked also most closely with me in the physics analysis, and even in daily life. I would like to express my thanks to his useful discussions and constant encouragements.

I would also like to extend my gratitude to Professor S.Sugimoto for his advises and encouragements at Osaka University.

I am very grateful to Dr. D.H.White and Dr. M.J.Murtagh for their hospitality and useful discussions at BNL. I would also like to thank to Dr. Dave Hedin, Dr. Eric Stern and Miss Ferrn Coyle, who gave me many helpful information about Monte Carlo.

I would like to give my appreciation to Professors E.W.Beier, D.Cutts, R.E.Lanou, A.K.Mann and M.D.Marx, who gave me helpful advises, and kept encouraging me.

I am also indebted to Mr. Ted Erickson, Mr. Marty Van Lith, Mr. Mich Newcomer and Dr. Milind Duwan worked closely with me in the maintenance of the calorimeter system of our detector.

A special thanks goes to Dr's. K.Amako, K.Abe, S.Kabe, Y.Kurihara, T.Shinkawa, Y.Suzuki, S.Tatsumi and S.Terada for scanning a great many data and stimulas discussions.

This work was supported in part by the Japanese Ministry of Education, Science and Culture and the U.S.Department of Energy through the Japan-U.S.A. Cooperative Research Project on High Energy Physics.

ABSTRACT

Results of an experiment carried out at the Brookhaven National Laboratory (BNL) exposed to a neutrino beam with a fine-segmented massive detector are presented. We have searched for "μe" events which consist of a muon and an electron emanating from the same vertex, which could be interpreted as a production and subsequent decay of a massive neutrino in the mode of $\pi/K \rightarrow \nu_H + \ell$, $\nu_H \rightarrow \mu e \nu_\ell (\ell=\mu,e)$. Existence of such events would indicate a new physics beyond the Standard Model (Glashow-Weinberg-Salam Model).

We have observed no evidence of such a heavy neutrino. New upper limits on lepton-mixing matrix elements $|U_{H\mu}|^2$ and $|U_{He}|^2$ as a function of the heavy neutrino mass were obtained. We did not confirm anomalous "μe"-pairs reported by the Aachen-Padova group.

TABLE OF CONTENTS

Chapter 1. INTRODUCTION 1

§1.1 Overview 1

§1.2 Massive Neutrinos 3

§1.3 Search for a Heavy Neutrino Decay 9
(subject of this experiment)

Chapter 2. EXPERIMENTAL APPARATUS 12

§2.1 Introduction 12

§2.2 Neutrino Beam 12

2.2.1 The beamline 12

2.2.2 Neutrino sources 14

§2.3 Detector Overview 15

2.3.1 Calorimeter 16

2.3.2 Proportional drift tube (PDT) 19

§2.4 Electronics 20

§2.4 Data Acquisition 22

Chapter 3. DATA REDUCTION 24

§3.1 Signal Extraction 24

3.1.1 Event reconstruction (NUE) 25

3.1.2 "μe"-filter 26

3.1.3 Eye scanning and kinematical cuts 27

§3.2 Backgrounds 34

3.2.1 π^o background 34

3.2.2 Dalitz decay of π^o 38

3.2.3 ν_e-induced interaction 39

3.2.4 Charmed baryon (Λ_c^+) production 41

3.2.5 Charge exchange process 43

§3.3 Final Events (Excess) 44

Chapter 4. RESULTS ON SEARCHES FOR ν_H AND ANOMALOUS μe EVENTS 45

§4.1 Heavy Neutrino Searches and Limits on Mixing Matrix Elements 45

4.1.1 Decay probability of the heavy neutrinos 46

4.1.2 Heavy neutrino spectrum 48

4.1.3 Acceptance 49

4.1.4 Upper limits 51

§4.2 Anomalous "μe" Search 54

Chapter 5. RESULTS AND DISCUSSIONS 56

APPENDIX A

APPENDIX B

REFERENCES

LIST OF TABLES

Table 2.1 : Summary of the E734 detector.

Table 2.2 : Properties of the liquid scintillator mixture.

Table 3.1 : The final numbers of the three samples.

Table 3.2 : The excesses of μe events and the number of subtracted γ's.

Table 3.3 : The excesses of the three samples for three different conversion lengths. This is used to estimate ambiguity of the conversion length.

Table 3.4 : The number of $\mu\gamma$ events and the background due to Dalitz decay.

Table 3.5 : The number of background from ν_e events.

Table 3.6 : The various branching ratios of Λ_c^+.

Table 3.7 : The resultant number of background events coming from each decay process of Λ_c^+ the acceptance together with branching ratios.

Table 3.8 : The background events of each process and the remaining number of events corresponding to the three final samples.

Table 4.1 : Our results on the upper limits for each mixing matrix elements, $|U_{H\mu}|^2$ and $|U_{He}|^2$ at 90% C.L..

FIGURE CAPTIONS

Figure 1.1 : The limit at 90% C.L. on the $\nu_\mu \rightarrow \nu_e$ oscillation, in the Δm^2 vs. $\sin^2 2\theta$ plane, obtained in our experiment at BNL [1.17].

Figure 1.2 : The limits at 90% C.L. on $|U_{H\mu}|^2$ and $|U_{He}|^2$ as a function of the neutrino mass, obtained by the secondary peaks search experiments and the beam dump experiments, are shown in (A) and (B) respectively : (a) the CHARM Collaboration from the beam dump experiment [1.24] ; (b) the BEBC Collaboration from the beam dump experiment [1.25] ; (c) the KEK/Tokyo Group from $K \rightarrow \nu e$ decay [1.21] ; (d) the decay $\pi \rightarrow \nu e$ at TRIUMP [1.23] ; (e) the study of $K \rightarrow \mu\gamma$ decay at KEK [1.20].

Figure 1.3 : Feynmann diagrams of the heavy neutrino production processes for (a) $\pi^+ \rightarrow e^+\nu_H$, (b) $\pi^+ \rightarrow \mu^+\nu_H$, (c) $K^+ \rightarrow e^+\nu_H$, (d) $K^+ \rightarrow \mu^+\nu_H$. The mixing matrix elements $|U_{H\ell}|$, ℓ = e or μ, contribute to the heavy neutrino production processes.

Figure 1.4 : Feynmann diagrams of the heavy neutrino decay processes for (a) $\nu_H \rightarrow \mu^- e^+ \nu_e$, (b) $\nu_H \rightarrow \mu^+ e^- \nu_e$, and muon decay process (c) $\mu^+ \rightarrow e^+ \nu_e \bar{\nu}_\mu$. The mixing matrix elements $|U_{H\ell}|$, ℓ = e or μ, contri-

bute to the heavy neutrino decay processes, (a) and (b).

Figure 2.1 : The Alternating Gradient Synchrotron (AGS) at Brookhaven National Laboratory. Protons are accelerated to 200 MeV by the linac and are injected into the Brookhaven AGS. Then the beam is accelerated to an energy of 28.3 GeV. To produce the wide band neutrino beam, the beam (about 10^{13} protons) is extracted by a fast-extracted-beam mode and transported to a neutrino production target at every 1.4 seconds.

Figure 2.2 : The layout of the magnetic horn system. The horns themselves are cylindrically symmetric with the proton target, enclosed in the entrance to the first horn.

Figure 2.3 : The enhancement of the neutrino flux by using the horn system. The upper curve is the ratio of the yield of neutrinos with the horn current on to that with the horn current off. The lower curve shows the same ratio for the opposite polarity particles.

Figure 2.4 : The whole view of the neutrino beamline. The beamline and decay region are shown with the magnetic horns and the detector.

Figure 2.5 : The distribution of event times for events in the neutrino detector, reflecting the bunch structure of the A.G.S. beam. The AGS has twelve proton bunches circulating, and extraction is accomplished in a single revolution.

Figure 2.6 : (a) The measured spectrum of ν_μ determined from quasielastic events together with the calculated result. (b) The calculated spectrum of ν_μ with the component contributions.

Figure 2.7 : (a) The measured spectrum of ν_e determined from quasielastic events together with the calculated result. (b) The calculated spectrum of ν_e with the component contributions.

Figure 2.8 : The E734 neutrino detector assembly which consists of the 112 main modules followed by the gamma catcher and the magnetic spectrometer.

Figure 2.9 : Front view of the calorimeter plane, each segmented into 16 (25 cm × 425 cm in area × 8 cm thick) cells viewed by photomultipliers at both ends.

Figure 2.10: A typical PMT's response to minimum ionizing particles as a function of distance from the PMT. The data points are fit by A·(exp(-x/B) + C).

Figure 2.11: The distribution of the reciprocal of the light attenuation constant (λ^{-1}) for all the calorimeter cells in one-fourth of the detector.

Figure 2.12: The measured energy distribution (dE/dX) of the calorimeter for minimum ionizing particles.

Figure 2.13: The time difference distribution of the calorimeter determined by the difference between the time measured by the PMT from individual cells(t_{scin}) and the calculated time from a fit to all scintillator times along a long track(t_{fit}).

Figure 2.14: Partially exploded view of a proportional drift tube (PDT) plane showing internal construction.

Figure 2.15: The spatial resolution of the PDT evaluated by use of the horizontal cosmic rays.

Figure 2.16: The overall angular resolution as a function of electron energy. The upper curve is the kinematical limit of the $\nu_\mu e$ interaction. The lower curve was measured resolution with test beam electrons.

Figure 2.17: The pulse hight distribution of the PDT measured by using the horizontal cosmic rays. The dE/dX is obtained by induced charge corrected by its path length in the cell.

Figure 2.18: Schematic of the signal processing electronics for a single calorimeter cell (Q-card).

Figure 2.19: Schematic of the electronics for time measurement of calorimeter cell signals (T-card).

Figure 2.20: Schematic of the analog and digital electronics for a PDT cell.

Figure 2.21: Blockdiagram of the complete E734 data acquisition system.

Figure 3.1 : Typical events in our detector, (a) A long muon track and (b) an electromagnetic shower. The neutrino beam enters at the left of the page. Shown are the two views xz and yz. The large boxes in the yz view are scintillator cells and the small boxes are PDT cells. The xz view contains only PDT hits.

Figure 3.2 : Data reduction flow to extract a signal for the heavy neutrino. As shown in this flow, the software filter ("μe"-filter) was first applied to the events and then double-scanned all events. Kinematic cuts (described in detail in subsection 3.1.3) were applied to the events which survived the filter and the scanning.

Figure 3.3 : Example of the time clustering. Each time cluster (TCL) contained time-related calorimeter hits were supposed to come from a single event.

Figure 3.4 : The distribution of the total visible energy versus shower energy by using the data which survived the eye scanning.

Figure 3.5 : Example of μe event. Both the shower pattern and the muon-like track are originating from the same vertex.

Figure 3.6 : Example of $\mu\gamma$ event. The shower pattern appears downstream of the vertex and is associated with the original point of the muon-like track.

Figure 3.7 : Example of π^o backgraound event. Two shower patterns appear downstream of the vertex and are associated with the original point of the muon-like track.

Figure 3.8 : Data reduction flow of the two-shower sample. The surviving events after the "μe"-filter were scanned to select two-shower sample. Criteria of the scanning for the two-shower sample were the same as those for single-shower sample except the requirement of two electromagnetic showers in an event.

Figure 3.9 : Example of the reaction $\nu_\mu n \rightarrow \mu^- p\pi^o$ simulating μe event. The reaction produces a short track of the proton accompanying π^o, where one decay γ converts close to the vertex and the other one is lost, simulates μe event.

Figure 3.10: Conversion distance distribution of the single-shower sample I (the dotted line shows the distribution from the π^o background).

Figure 3.11: Conversion distance distribution of the single-shower sample II (the dotted line shows the distribution from the π^o background).

Figure 3.12: Conversion distance distribution of the ν_H sample (the dotted line shows the distribution from the π^o background).

Figure 3.13: Conversion distance distribution of the two-shower sample (the dotted line shows the distribution from the π^o background).

Figure 3.14: Conversion distance distribution of the single-shower sample before 1 GeV cut.

Figure 3.15: Schematic view of the background event from Dalitz decay, having a proton track with one decay γ lost.

Figure 3.16: The cross sections for (a) $\nu_e N \rightarrow e^- N \pi^+$ (N = p or n) and (b) $\nu_\mu N \rightarrow \mu^- N \pi^+$ (N = p or n), based on the Rein-Sehgal model.

Figure 3.17: Data reduction flows of Monte Carlo for (a) $e^- p \pi^+$ and (b) $e^- n \pi^+$.

Figure 3.18: The cross section of $\nu_\mu n \rightarrow \mu^- \Lambda_c$

Figure 4.1 : The behavior of $\overline{\rho}$ as a function of m_{ν_H} for the decay modes (a) $\pi^+ \to \mu^+ \nu_H$, (b) $\pi^+ \to e^+ \nu_H$, (c) $K^+ \to \mu^+ \nu_H$ and $K^+ \to e^+ \nu_H$. The rates of the π/K decay into the electron and heavy neutrino are enhanced (i.e. $\rho >> 1$) except at small mass region where helicity suppression takes effect, while the decay into massless neutrinos is strongly suppressed.

Figure 4.2 : The heavy neutrino spectra divided by the mixing matrix element $\phi_{\nu_H}/|U_{He}|^2$ for $K^+ \to e^+ \nu_H$ for several masses from 200 to 470 MeV.

Figure 4.3 : The heavy neutrino spectra divided by the mixing matrix element $\phi_{\nu_H}/|U_{H\mu}|^2$ for $K^+ \to \mu^+ \nu_H$ for several masses from 200 to 370 MeV.

Figure 4.4 : The acceptance for the heavy neutrinos for several masses from 200 to 470 MeV. In the low energy region the acceptance is limited by the 1 GeV energy cut, while in the high energy region it is limited by the requirement of the 0.05 radian opening angle between the muon and electron.

Figure 4.5 : The variation of the acceptance for heavy neutrinos caused by shifts of energy cut estimated as the systematic error.

Figure 4.6 : The variation of the acceptance for heavy neutrinos caused by shifts of opening angle cut estimated as the systematic error.

Figure 4.7 : The flux averaged acceptance with systematic errors estimated from the energy and opening angle variations for (a) $K^+ \to e^+ \nu_H$ and (b) $K^+ \to \mu^+ \nu_H$.

Figure 4.8 : (A) Upper limits at 90% C.L. for the mixing matrix elements in the $|U_{H\mu}|^2$ and $|U_{He}|^2$ space. In this figure the region outside the contour of 90% C.L. upper limit in the $|U_{H\mu}|^2$ and $|U_{He}|^2$ space is excluded. The individual upper limits of 90% C.L. for the mixing matrix elements $|U_{H\mu}|^2$ and $|U_{He}|^2$ are shown in (B) and (C) respectively together with the results from other experiments : (a) limits obtained by the CERN PS191 experiment from $K \to \nu e$ and $\pi \to \nu e$ decay [4.3] ; (b) the CHARM Collaboration from the beam dump experiment [1.24] ; (c) the CHARM Collaboration from the wide band experiment [4.4] ; (d) the BEBC Collaboration from the beam dump experiment [1.25] ; (e) the KEK/ Tokyo Group from $K \to \nu e$ decay [1.21] ; (f) the decay $\pi \to \nu e$ at TRIUMP [1.23] ; (g) the study of $K \to \mu\gamma$ decay at KEK [1.20] ; (h) solar neutrinos [4.5] ; (i) from $K \to \overline{\nu\nu}\nu\mu$ decay at LBL [4.6] ; (j) from the study of the branching ratio of $K \to \nu e$ [4.7] (see also ref.[1.19]).

Chapter 1. INTRODUCTION

§1.1 Overview

An existence of a neutrino was first postulated by Pauli in 1930 [1.1]. Pauli introduced the neutrino in order to explain the continuous spectrum of electrons emitted in nuclear β decay. The neutrino was assumed to be a fermion having 1/2 spin, no charge, and given a mass nearly zero but not exactly zero originally.

A direct neutrino induced interaction,

$$\bar{\nu}_e + p \rightarrow e^+ + n \qquad (1\text{-}1)$$

was first observed by Reines and Cowan in 1956 [1.2], over twenty years after the Pauli's suggestion. Since then, fundamental properties of the neutrinos have been studied extensively. For example, helicity of the electron neutrino (ν_e) was measured by Goldhaber et al. in 1958 [1.3] and that of the muon neutrino (ν_μ) was measured by Backenstoss et al. in 1961 [1.4]. The fact that ν_e and ν_μ are two different particles ($\nu_e \neq \nu_\mu$) was discovered by the Columbia group at BNL in 1962 [1.5].

The minimal standard electroweak model proposed by Glashow, Weinberg and Salam in 1960's [1.6] predicted the existence of neutral current interactions. In 1973 two neutral current interactions of neutrinos such as

$$\nu_\mu(\bar{\nu}_\mu) + e \rightarrow \nu_\mu(\bar{\nu}_\mu) + e \qquad (1\text{-}2)$$

$$\nu_\mu(\bar{\nu}_\mu) + N \rightarrow \nu_\mu(\bar{\nu}_\mu) + X \qquad (1\text{-}3)$$

were observed by a bubble chamber group at CERN [1.7] and confirmed the important prediction of the model. In addition, direct discovery of the intermediate vector bosons $W^{\pm}$ and Z^{o} by UA1 and UA2 groups at CERN $P\bar{P}$ collider in 1983 [1.8] firmly confirmed this minimal version of the standard gauge model of the electroweak interactions. In this model, however, there is no positive principle of the mass of neutrinos.

Some of grand unified theories (GUTs) [1.9], which require violation of lepton number as well as baryon number conservation, allow existence of non zero neutrino masses. The left-right symmetric model [1.10] developed as an extension model of the electroweak interaction, which restores parity conservation at high energy, assumes finite mass of the neutrinos implicitly. Furthermore massive neutrinos could provide solutions to some cosmological and astrophysical problems such as, the dark matter in the universe and galaxy, and the solar neutrino puzzle [1.11]. Massive neutrinos could play an important role both in the fields of particle physics and in astrophysics.

In spite of the extensive experimental and theoretical studies, the fundamental properties of the neutrinos, especially the mass of neutrinos, are still open questions. Therefore, a search for massive neutrinos has been of great interest and one of the promising probes to look into new physics beyond the standard

model and to find a solution of those astrophysical problems.

§1.2 Massive Neutrinos

If neutrinos have masses, then their weak eigenstates like ν_e, ν_μ and ν_τ need not to be the same as their mass eigenstates like ν_1, ν_2 and ν_3 [1.12]. In general, these two eigenstates of the neutrinos are related through unitary mixing matrices $U_{\ell i}$:

$$\nu_\ell = \sum_{i=1}^{n} U_{\ell i} \nu_i \quad , \ \ell = e, \mu, \tau, \cdots, \qquad (1\text{-}4)$$

where ν_ℓ and ν_i denote the weak and the mass eigenstates, respectively.

The present upper limits on the masses of known three neutrino flavors are :

$$\begin{aligned} m_{\nu_e} &\leqq 18 \text{ eV} \\ m_{\nu_\mu} &\leqq 250 \text{ keV} \\ m_{\nu_\tau} &\leqq 35 \text{ MeV} \end{aligned} \qquad (1\text{-}5)$$

respectively [1.13]. In general the present mass limit on ν_ℓ ($\ell = e, \mu, \tau$), obtained by the direct searches for neutrino mass, can be interpreted as a mass limit on ν_i ($i = 1,2,3$) if the mixing matrix $U_{\ell i}$ is almost diagonal, i.e., $|U_{jj}| >> |U_{jk}|$, $j \neq k$, supposing that the mass of ν_i's is monotonically increasing, i.e., $m(\nu_i) \leqq m(\nu_{i+1})$.

There are other kinds of phenomena induced through the non

zero off-diagonal mass-mixing matrix elements, which are also sensitive to neutrino masses. When the mass differences between various neutrino species are large enough, neutrinos could decay into lighter particles. While in the case of the small mass differences, i.e., smaller than 100 eV or so, the effect may manifest itself in a phenomenon of the so-called neutrino oscillation between different flavors. Therefore, the off-diagonal elements including higher generations, $|U_{\ell i}| << 1$, $i=1,2,3,..,n$, can be explored through those phenomena. The experiments to search for those phenomena may be called indirect searches for neutrino masses.

Before we explain about a search for heavy neutrino decays which is the present subject of this paper, we quickly review other experimental techniques, directly or indirectly, to search for masses of neutrinos.

1. Precise and direct measurements of the mass of electron neutrinos

The end point electron energy spectrum in a tritium β decay $^3H \rightarrow {}^3He + e^- + \bar{\nu}_e$ has been most widely employed in order to detect the neutrino mass directly. An experiment carried out by Lubimov et al. at ITEP claimed a finite neutrino mass [1.14]:

$$14 \leqq m_\nu \leqq 46 \text{ eV/c}^2 \qquad (1\text{-}6)$$

But several other experiments have reported the new upper limits on $m_{\bar{\nu}_e}$ such as $m_\nu < 18$ eV/c^2 [Zurich/SIN], $m_\nu < 27$ eV/c^2 [Los Alamos] and $m_\nu < 32$ eV/c^2 [INS(Tokyo)] [1.15], which have

not supported the above ITEP result.

A neutrinoless double-beta decay $(\beta\beta)_{0\nu}$, $(Z,A) \rightarrow (Z+2,A) + e^+ + e^-$ provides a sensitive experiment for both Majorana mass and lepton number violation. So far no such process has been observed and the upper limit on the averaged Majorana mass is $\langle m_\nu \rangle < 1.1$ eV [1.16].

2. Neutrino oscillation

The neutrino oscillation experiments have a good sensitivity to small neutrino masses and moderate sensitivity to the mixing angle.

If we consider a neutrino oscillation between two lepton generations for simplicity, the weak eigenstates ν_e and ν_μ relate to the mass eigenstates ν_1 and ν_2 as :

$$\begin{aligned} \nu_e &= \nu_1 \cos\theta + \nu_2 \sin\theta \\ \nu_\mu &= -\nu_1 \sin\theta + \nu_2 \cos\theta \end{aligned} \qquad (1\text{-}7)$$

where θ is the mixing angle.

Then the probability that the neutrino which was originally ν_e appears as ν_μ at distance L (in meter) is

$$P(\nu_e \rightarrow \nu_\mu) = \sin^2 2\theta \cdot \sin^2(1.27 \cdot \Delta m^2 \cdot L/E) \qquad (1\text{-}8)$$

where Δm^2 is the difference of the neutrino masses squared in eV^2, and E is the neutrino energy in MeV. Figure 1.1 shows 90% C.L. limits on $\nu_\mu \rightarrow \nu_e$ oscillations, in the Δm^2 vs. $\sin^2 2\theta$ plane,

obtained in our experiment at BNL [1.17].

The present limits on Δm^2 for maximum mixing, and on $\sin^2 2\theta$ for large Δm^2, are [1.18]:

$$\begin{array}{lll} \nu_\mu \rightarrow \nu_e & \Delta m^2 < 0.018\ eV^2 \\ & \sin^2 2\theta < 0.0032 \\ \nu_\mu \rightarrow \nu_x & \Delta m^2 < 0.29\ eV^2 \\ & \sin^2 2\theta < 0.015 \\ \nu_e \rightarrow \nu_x & \Delta m^2 < 0.018\ eV^2 \\ & \sin^2 2\theta < 0.07 \end{array} \qquad (1\text{-}9)$$

According to eq.(1-4) and (1-7), $|\cos\theta|$ is the diagonal matrix element $|U_{e1}|$ or $|U_{\mu 2}|$, and $|\sin\theta|$ is the off-diagonal matrix element $|U_{e2}|$ or $|U_{\mu 1}|$. Therefore the limit of $\sin^2 2\theta < 0.0032$ could be reinterpreted $|U_{e2}|^2$ or $|U_{\mu 1}|^2 < 8.0 \times 10^{-4}$.

3. Secondary peaks search

A class of experiments was proposed by R.E.Shrock [1.19] searching for heavy neutrinos by measuring the energy spectrum of the lepton in two-body decays in $\pi \rightarrow e\nu_H$, $\pi \rightarrow \mu\nu_H$, $K \rightarrow e\nu_H$ and $K \rightarrow \mu\nu_H$. If the ν_H is produced, the energy spectrum of these charged leptons should exhibit a discrete peak displaced from the place expected in the normal two-body decay.

The first experiment to search for heavy neutrinos emitted in $K^+ \rightarrow \mu^+\nu$ decay was performed at the National Laboratory for High Energy Physics (KEK) [1.20] and obtained an upper limit of

$0.5 \sim 2 \times 10^{-5}$ for the mixing ratio between ν_μ and a heavy neutrino, $|U_{H\mu}|^2$, for a mass range of 160 ~ 230 MeV/c². In this experiment, the spectrum of the muon range in the stopped K^+ decay was measured to search for a discrete line associated with the heavy neutrino emission in $K_{\mu 2}$ decay. The best limit on $|U_{H\mu}|^2$ in this type of experiment was obtained by a dedicated experiment using a high resolution magnetic spectrograph at KEK [1.21]. The experiment obtained an upper limit of $10^{-4} \sim 9\times10^{-7}$ for a wide mass range of 70 ~ 300 MeV/c².

The upper limit on $|U_{H\mu}|^2$ in a small mass region below 50 MeV/c² can be obtained by using $\pi_{\mu 2}$ decay. The best limit was given by SIN group as $10^{-2} \sim 3 \times 10^{-5}$ in the mass range of 1 ~ 20 MeV/c² [1.22].

Similarly, the upper limit on $|U_{He}|^2$ can be obtained by using the K_{e2} and π_{e2} decays. KEK group reported the upper limit of $|U_{He}|^2 < 10^{-6} \sim 10^{-5}$ through the K_{e2} decays in the mass range of 100 ~ 500 MeV/c² [1.21]. In the mass range of 10 ~ 100 MeV/c², the upper limits of $10^{-7} \sim 10^{-5}$ were obtained by SIN and Triumpf groups [1.23].

4. Beam dump experiments

A proton beam is dumped onto a high density target which absorbs nearly all the secondary π's and K's before they decay. Heavy neutrinos have been assumed to be produced in a semileptonic decay of charged and neutral D mesons, and in a leptonic decay of charged D's. Beam dump experiments search for a decay

of such neutrinos in a neutrino detector. The mass eigenstate ν_3 in particular has been assumed to be produced in charmed F meson decays. The beam dump experiment can probe a larger kinematic range of neutrino mass up to $(m_D - m_e)$.

The CHARM Collaboration has performed searches for decays of heavy neutrinos produced by dumping 400 GeV protons in a Cu target at CERN SPS [1.24]. They obtained an upper limit on $|U_{3e}|^2$ to the order of 10^{-10} for a heavy neutrino associated with τ lepton by searching for a decay mode of $\nu_3 \rightarrow e^+e^-\nu_e$ in the mass range of $10 \sim 250$ MeV and the upper limits of $|U_{He}|^2, |U_{H\mu}|^2 < 10^{-7}$ for the neutrino masses around 1.5 GeV by searching for the decay modes $e^+e^-\nu_e$, $\mu^+e^-\nu_e$ and $\mu^+\mu^-\nu_\mu$ [1.24].

The BEBC bubble chamber group has also performed a search for heavy neutrino decays in a proton beam dump experiment at CERN [1.25]. They obtained upper limits $|U_{H\mu}|^2$, $|U_{He}|^2 < 10^{-6} \sim 10^{-7}$ for the mass range of $0.5 \sim 1.75$ GeV, and also limits on $|U_{3\mu}|^2 < 10^{-7} \sim 10^{-8}$, $|U_{3e}|^2 < 10^{-9} \sim 10^{-10}$ for the mass eigenstate ν_3 in particular in the mass range of $150 \sim 190$ MeV/c^2 [1.25]. The results of the secondary peaks search experiments and the beam dump experiments are summarized in Figure 1.2.

§1.3 Search for a Heavy Neutrino Decay (Subject of this experiment)

A number of experiments have been performed by applying complementary techniques in order to search for massive neutrinos. The precise and direct measurement of the mass of light neutrinos do not have a sensitivity to the off-diagonal mixing matrix elements. The experiment searching for neutrino oscillations among different flavors has a sensitivity on the off-diagonal elements squared to the order of $10^{-4} \sim 10^{-2}$ and on the mass difference below 100 eV. The secondary peaks search and beam dump experiments can give the smaller values on the mixing matrix elements squared to the order of around 10^{-2} than the neutrino oscillation experiments, but in the mass range from several MeV to several hundred MeV.

Another approach which we have adopted and is potentially more sensitive is to look for the heavy neutrinos contaminated in a ordinary neutrino beam. The principle of the detection is as follows. According to the equation (1-4), the heavy neutrino ν_H as a mass eigenstate, is possibly produced from the same source of ν_e, ν_μ or ν_τ through the mixing matrix, if it is allowed kinematically. Then the produced heavy neutrinos may decay into lighter particles while traveling in the beam. In our experiment, the heavy neutrinos are supposed to be produced through the decays of $\pi^+ \to \ell^+\nu_H$ and $K^+ \to \ell^+\nu_H$, ℓ = e or μ, and to decay into the electron, muon and ordinary neutrino, i.e. $\nu_H \to \mu e \nu_\ell$, ℓ = e or μ. Feynmann diagrams of the heavy neutrino production process from π^+ and K^+ are shown in Figures 1.3.(a) - (d). Figure

1.4.(a) and (b) show the subsequent decay process of the heavy neutrinos. This method is similar in physics to the secondary peak search, because the heavy neutrinos is produced in the decay of Kaons or pions. In comparison with the secondary peaks search, however, this experiment has much higher sensitivity on the mixing matrix elements squared, $|U_{H\mu}|^2$ and $|U_{He}|^2$. On the other hand, technical approach is very much like as the beam dump experiment because it tries to detect the decay products of the heavy neutrinos using a massive neutrino detector. Beam dump experiments in the past were carried out using high energy ($\sim$ 100 - 200 GeV) neutrino beam line at CERN and hence the distance between the production target and the detector was 5 times longer than ours which used low energy neutrino beam line at BNL. Because of this, our apparatus has larger acceptance and has a potential to obtain higher sensitivity than the previous experiments.

In this thesis the results of an experiment performed by using the neutrino beam at the Brookhaven National Laboratory AGS (Alternating Gradient Synchrotron) are presented. The main goal of this experiment was to search for heavy neutrinos which were produced by the decays of K's and π's and subsequently decayed in a particular decay mode of $\nu_H \rightarrow \mu e \nu_\ell$, ℓ = e or μ. Failure to observe such events improves upper limits on the mixing matrix elements squared $|U_{H\ell}|^2$, ℓ = e or μ.

We also performed a more general search looking for anomalous μe events in final states, which are not necessarily related to heavy neutrinos. The aim of this search was to study the

anomaly reported by the Aachen-Padova group at CERN PS in 1981 [1.26]. They claimed an excess of μe events with a rate relative to all charged current reactions of $(6.9 \pm 2.5) \times 10^{-5}$. Since their experiment, using the CERN PS wide band neutrino beam with an averaged energy of 2.2 GeV, is similar to ours, the existence of the anomalous μe events can be tested by this search if it exists.

In chapter 2 we present the experimental apparatus. Chapter 3 describes how to extract signals and discusses about the background subtractions. In chapter 4 results are given and discussions are presented.

Chapter 2. EXPERIMENTAL APPARATUS

§2.1 Introduction

The experiment has been performed by using a horn focused wide band neutrino beam with an average beam energy of 1.4 GeV at the Brookhaven Alternating Gradient Synchrotron (AGS).

The detector was primarily designed to detect reactions of the weak neutral current,

$$\nu_\mu(\bar{\nu}_\mu)e^- \rightarrow \nu_\mu(\bar{\nu}_\mu)e^- \text{ and } \nu_\mu(\bar{\nu}_\mu)p \rightarrow \nu_\mu(\bar{\nu}_\mu)p, \qquad (2\text{-}1\text{-}1)$$

and the weak charged current reactions [2.1],

$$\nu_\mu n \rightarrow \mu^- p \text{ and } \nu_\mu p \rightarrow \mu^+ n \ . \qquad (2\text{-}1\text{-}2)$$

Therefore the detector ensures a good ability to identify heavy neutrino signals consisting a muon and an electron as decay products.

§2.2 Neutrino Beam

2.2.1 The beamline

Protons are accelerated to 200 MeV by a linac and are injected into the Brookhaven AGS. Then the beam is accelerated to an energy of 28.3 GeV [Figure 2.1]. The beam (about 10^{13} protons) is extracted by a fast-extracted-beam mode (FEB) and transported to a neutrino production target at every 1.4 seconds.

The target is a sapphire ($A\ell_2O_3$), 6.4 mm in diameter and 45

cm long. It has a low Z with relatively high density. The density and Z of sapphire are 4 (g/cm^3) and 50, respectively. A material with low Z and the relatively high density makes pion reabsorption lower and the efficiency of secondary particles production high.

Secondary particles produced by the proton interactions at the target are focused by the two horn system as shown in Figure 2.2. Two horns are cylindrically symmetric and generate a pulsed magnetic field. For neutrino running, the horns focus positive particles and defocus negative particles. For antineutrino running, the horn polarity is reversed. This system increases the flux of neutrinos about a factor of 10. In Figure 2.3 we show the enhancement in the neutrino flux produced by using this horn system. Also in Figure 2.3 is shown the effect of the horn system for "wrong sign" particles.

Following the production target and the horn system, there is a 50 m long drift space, called a decay region, where most of pions and kaons decay. Hadron- and muon-shield consisting of earth and steel of 30 m long begins at the end of the decay region. The muon shield is made from segmented steels. A few counters for measuring the beam position, intensity and timing, are inserted between the steels. The whole view of the neutrino beamline is shown in Figure 2.4.

The time structure of the beam, measured by neutrino quasi-elastic interactions, is shown in Figure 2.5. The beam, preserving RF time structure, arrives at the target in 12 bunches 224 ns apart. The width of each bunch is about 30 ns. This time struc-

ture of the beam makes the cosmic ray backgrounds considerably small.

2.2.2 Neutrino sources

The predominant decay modes of pions and kaons are ;

$$\pi^+ \rightarrow \mu^+ + \nu_\mu \quad , \quad \text{Branching Ratio} = 1.00 \qquad (2\text{-}2\text{-}1)$$

and

$$K^+ \rightarrow \mu^+ + \nu_\mu \quad , \quad \text{Branching Ratio} = 0.64 \qquad (2\text{-}2\text{-}2)$$

The energy of neutrinos from the modes (2-2-1) and (2-2-2) is given by ;

$$E_\nu = \frac{m_\pi^2 - m_\mu^2}{2(E_\pi - P_\pi \cos\theta_\nu)}$$

$$\cong E_\pi \cdot (1 - m_\mu^2/m_\pi^2) \cdot \frac{m_\pi^2}{P_\pi^2 \theta_\nu^2 + m_\pi^2} \qquad (2\text{-}3\text{-}1)$$

and

$$E_\nu = \frac{m_K^2 - m_\mu^2}{2(E_K - P_K \cos\theta_\nu)}$$

$$\cong E_K \cdot (1 - m_\mu^2/m_K^2) \cdot \frac{m_K^2}{P_K^2 \theta_\nu^2 + m_K^2} \qquad (2\text{-}3\text{-}2)$$

respectively, where E_ν is the laboratory energy and θ_ν is the emission angle of the neutrino.

Only neutrinos emitted close to the forward direction reach the detector located at about 100 m downstream from the production target. Suppose $\theta_\nu = 0$ and $E_\pi >> m_\pi$, E_ν becomes $\doteqdot E_\pi/2$ for the decay mode $\pi^+ \rightarrow \mu^+ \nu_\mu$, and E_ν becomes $\doteqdot E_K$ for the decay mode $K^+ \rightarrow \mu^+ \nu_\mu$. Therefore the high energy part of the neutrino spectrum mainly comes from K^+ decay.

There are also some ν_e's which come mainly from the decays. In higher energy region, these ν_e's mainly come from :

$$K^+ \rightarrow \pi^o + e^+ + \nu_e \quad , \quad \text{Branching Ratio} = 0.05 \qquad (2\text{-}4)$$

and

$$K_L^0 \rightarrow \pi^- + e^+ + \nu_e \quad , \quad \text{Branching Ratio} = 0.39 \qquad (2\text{-}5)$$

The ν_e/ν_μ ratio is about 3×10^{-3} on an average for the entire beam spectrum. The measured and calculated spectra of ν_μ and ν_e are shown in Figures 2.6 (a), (b) and Figures 2.7 (a) and (b), respectively [1.17].

§2.3 Detector Overview

The main detector consists of vertical planes of liquid scintillator, each segmented into 16 (25 cm × 425 cm in area × 8 cm thick) cells viewed by photomultipliers at both ends and two crossed planes of proportional drift tubes, each plane being divided into 54 (7.6 cm × 420 cm in area × 3.8 cm thick) cells [Figure 2.8]. In Table 2.1 characteristics of the detector is

given. Two planes of drift tubes with x and y coordinates and a plane of liquid scintillator constitute a module. The main detector, which consists of 112 modules, weighs 172 tons. One radiation length and one nuclear collision length of the main detector corresponds 4.6 and 6.4 modules, respectively. The total mass of the liquid scintillator amounts to 75% of the total detector weight. A 30 ton shower counter (gamma-catcher) of 12 radiation lengths depth, which consists of 10 calorimeter planes having a sheet of 1 radiation thick lead converter between each two planes, is placed immediately downstream of the main detector which is followed by a magnetic spectrometer of 1.8 m × 1.8 m × 0.46 m aperture. The former provides a better containment of electromagnetic showers, while the latter is used in the study of the neutrino induced quasi-elastic reactions in the very low q^2 region and the measurement of the wrong sign neutrino contamination present in the incident neutrino beam.

The fine segmentation (1792 scintillator cells and 12096 proportional drift cells) and the pulse height and the timing characteristics of the elements provide determination of event topology, identification of electromagnetic showers.

2.3.1 Calorimeter

The design of the calorimeter was determined in order to meet the experimental requirements as follows :

1. Active target-detector.
2. Good time resolution of approximately 2 nsec.

3. Good dE/dX energy resolution of $\sigma/E \lesssim 25\%/\sqrt{E_e}$.

4. Good sensitivity to energy deposition as low as 5 MeV.

5. Capability for measuring multiple hits.

As shown in Figure 2.9, each calorimeter plane consists of 16 vertical cells separated optically and mechanically. Each cell contains a mixture of 50% mineral oil and 50% liquid scintillator NE235A inside a cell of $7.63 \times 25.4 \times 422$ cm^3 made by extruded acrylic of 0.5 cm thick. The properties of the liquid scintillator are given in Table 2.2. The black injection molded acrylic end cap was mounted at each end. Inside the surface of the cap was coated with a light reflective aluminized film. Both sides of each cell were viewed by Amperex 2212 photomultiplier (PMT) tubes . The PMTs were calibrated and the gain was adjusted with an internal divider.

Performance of Calorimeter

When a charged particle passes through the calorimeter, the liquid scintillator emits light with an intensity proportional to the energy deposited. The intensity of the emitted light is attenuated by scattering and absorption in the liquid scintillator cells. To calibrate this light attenuation as a function of the distance of the charged particle from the PMT, cosmic rays which passed the calorimeter vertically were used.

The position x, where the cosmic ray traversed, was calculated by :

$$x = L/2 + (T_1 - T_2)/2v \qquad (2\text{-}6)$$

where L is the distance between the two PMT's, T_1 and T_2 are the time of both PMT's respectively, and v is "the light velocity" in the liquid scintillator including the effect of the internal reflection.

The ADC (Analog to Digital Convertor) output of the i-th PMT Q_i^{out} is assumed to be given by :

$$Q_i^{out}(x) = A_i \cdot (\exp(-x/B_i) + C_i) \qquad (2\text{-}7)$$

where A_i,B_i and C_i are parameters to be fixed experimentally. B_i is the attenuation length.

A typical PMT's response to minimum ionizing particles as a function of distance from the PMT is shown in Figure 2.10. Typically, the attenuation length is around 170 cm [Figure 2.11].

The energy deposit in a calorimeter cell is calculated by the following formula :

$$E = E_{min} \cdot \frac{(Q_L + Q_R)}{(Q_{L_{min}} + Q_{R_{min}})} \qquad (2\text{-}8)$$

where E_{min} is the averaged energy deposit of minimum ionizing particles, Q_L and Q_R are outputs from the left and right PMT, $Q_{L_{min}}$ and $Q_{R_{min}}$ are the calculated outputs of the left and right PMT for the minimum ionizing particles at the position where the

particle traverses. The measured energy distribution for minimum ionizing particles is shown in Figure 2.12. The time difference between the time measured by a PMT and the calculated time from a fit to times along a long track is shown in Figure 2.13.

To monitor the timing of PMT, a fiber optics system, which gives light from a spark gap driven by Nano Pulser Model 437A, Xenon Corp., was employed. The timing and the energy deposition were calibrated by using vertical and horizontal cosmic ray muons.

2.3.2 Proportional drift tube (PDT)

PDTs were used as tracking chambers covering large area with high spatial resolution and used also for measuring dE/dX of the charged particle. Each module of the main detector has two PDT planes an X and Y PDT plane.

Each PDT plane consists of 54 identical cells, as shown in Figure 2.14. The size of a PDT cell is $3.81 \times 7.62 \times 427$ cm^3. The cells were made by aluminium. A 90% argon and 10% methane gas mixture (P10 gas) was used for the chamber. The stainless steel anode wire was 75 μm in diameter. The tension of wire was set around 400 g. The PDTs were operated at approximately 2.5 kV.

Performance of PDT

The PDTs were operated in a proportional region. The relation between the incident position of a charged particle and the

drift time was measured.

Spatial resolution and the dE/dX of PDT are evaluated by use of the horizontal cosmic rays. The spatial resolution was found to be 1.5 mm as shown in Figure 2.15. The overall angle resolution was also obtained to be 16 mrad/$\sqrt{E_e}$ as shown in Figure 2.16. The resolution of the dE/dX was 60% at FWHM [Figure 2.17].

The gas gain of the PDTs was stabilized by measuring the amplitude of a 23 keV X-ray peak from a ^{109}Cd source which is placed on a small PDT having the same geometry as the one of the main detector in the input gas system and then continuously adjusting the high voltage.

§2.4 Electronics

The design of the electronics of this experiment was determined to meet the following features :

1. A large number of channels ; 1792 × 2 PMT's and 12096 PDT's.
2. A low event rate ; one neutrino interaction / pulse.
3. Simultaneous calibration run with data taking ; cosmic ray events for calibrations are taken while taking neutrino events opening a gate between neutrino pulse.

The electronics was designed to operate in a triggerless mode, a gate of 10 μs was opened for an each AGS pulse and collected data from the PMT and PDT hits.

Calorimeter Electronics

Signals from 8 PMT channels for 4 scintillator cells are processed on two printed circuit boards. Eight analog signals are processed on one board (Q-card) and eight timing signals are processed on other board (T-card). A block diagram of the Q-card is shown in Figure 2.18. The Q-card has integrate and hold electronics and discriminators. The discriminators for all channels in 32 modules have a common programmable threshold. Any signal above threshold in either the left or right channel opens a gate about 800 ns long for integration of the signal in both the left and right channels. The gate begins when the RESTORE signal is disabled and ends when the HOLD signal asserted. While the gate is opened, the signal is integrated and the amplitude is measured from the baseline to the peak of the charge integral.

A block diagram of the T-card is shown in Figure 2.19. The T-card processes the signal and records a coarse time by counting a 25 MHz master clock and a fine time with 1 ns resolution within the 40 ns clock width. As soon as one fine time circuit has fired, the second circuit is automatically enabled so that another discriminator signal will begin the analog fine time processing. Accordingly, two fine times and up to thirteen additional coarse times for 16 PMTs can be recorded.

PDT Electronics

The PDT electronics boards are mounted on the PDT frames. A scheme of electronics of the PDT readout are shown in Figures 2.20.

Eight channels of the PDT are processed on one card. There are 14 such cards in an X-Y pair of PDT planes. Each signal from a PDT anode wire is amplified. An additional gain (x11) is provided by a linear amplifier and a gated integrator stores the resulting signal as a voltage on a capacitor on the A-card. The "S gate" is a 6 μs gate for the integrator and the "P gate" is used to reset the capacitor. The processing of time information is done on the D-card.

Each channel has two independent counters, which are referenced to a 50 MHz pulse train derived from the 100 MHz master oscillator and precisely synchronized to the scintillator electronics clock. A signal from the discriminator enables the first counter (T1) and a second pulse enables the second counter (T2). These counters count whenever the clock gate is on and stop counting at the end of the clock pulse train. Thus the time measurement has a common stop. The least count of 10 ns which corresponds to about 0.3 mm drift distance is achieved by using the clock phase information.

§2.5 Data Acquisition

A skematic diagram of the data acquisition system is shown in Figure 2.21. All PMTs and PDT wires were connected to separate front end electronics which contained a clock and sample-and-holds. The charge correspoding to deposited energy was stored in the sample-and-hold being multiplexed. The purpose of recording two times was to determine whether there was second hit within the same event from a muon decay.

The front end electronics on each plane, either a calorimetor plane or PDT plane, were locally controlled by a plane controller or crate controller for calorimeter, which set a flag if there was any hit in the plane. It also interfaced signals between front end electronics and a scanner.

Three scanners, two for PDTs and one for calorimeter, were connected to the PDP11/03. Each scanner, which has an ADC, collects and encodes data, and stores them into PDP11/03. In the data acquisition system there are four microprocessors, each of which controls one fourth of the whole detector. They are connected to PDP11/34 to which stored data are sent through direct memory access modules(BR11B). The PDP11/34 controls and monitors the over all data taking process.

A program MULCH, which is a modified version of the program MULTI developed at Fermilab and runs on the PDP11/34, handles the control of the detector. The information concerning the beam condition from a beam monitor system is read by the PDP11/34 through CAMAC.

Raw data from the detector is buffered and saved on magnetic tapes by the PDP11/34, then passed to the off-line analysis on the central computer CDC7600.

Chapter 3. DATA REDUCTION

§3.1 Signal Extraction

The data presented here contains 5.34×10^5 beam bursts corresponding to 3.78×10^{18} protons on neutrino production target (P.O.T.) and is a part of what was used for the precise determination of $\sin^2\theta_W$ from pure leptonic $\nu_\mu e \rightarrow \nu_\mu e$ reactions [2.1]. The period of the data acquisition was from November 21, 1981 to January 19, 1982. The raw data was processed first through an event reconstruction program (NUE) on the central computer CDC7600 at the Brookhaven National Laboratory (BNL) and about 200 data summary tapes (DST's) were produced.

Signal we are looking for is a "μe" event, which appears as one long track and one electromagnetic shower originating from the same vertex. A typical long muon track and electromagnetic shower event observed in our detector is shown in Figure 3.1.(a) and (b), respectively. (An example of "μe" event is shown in Figure 3.5.)

The data reduction flow to extract a signal for the heavy neutrino, is shown in Figure 3.2. As shown in this flow, we applied a "μe"-filter (denoted as software filter in the figure) on the events and then double-scanned all events. Kinematic cuts, described in subsection 3.1.3, were applied to the events which survived the filter and the scanning.

The HITAC M280HX at KEK, VAX 11/780 at BNL and FACOM M360R at Osaka University were used for processing the data.

3.1.1 Event reconstruction (NUE)

As we collected the data in a triggerless mode, sometimes two events overlap in the same beam spill. The two main roles of the NUE are to separate those events by using the information of the calorimeter, which we call time clustering, and then to reconstruct tracks.

Time clustering

If the sum of the energy deposited within a 40 ns time width was above 20 MeV, then the calorimeter hits contained in this time window were defined to belong to the same time cluster (TCL). Therefore, each TCL contained time-related hits, which were supposed to come from a single event. An example of the time clustering is shown in Figure 3.3. Three independent neutrino interactions happened in the same beam bunch were separated clearly by this clustering logic. The probability, that more than one event happens in the same TCL was less than 2 %.

Tracking

After the time clustering, the PDT hits in XZ and YZ-views were associated to the calorimeter hits. Then the PDT hits in each view were formed into two dimensional track segments. Three dimensional tracks were reconstructed by using those two dimensional tracks which matched in both views.

3.1.2 "μe"-filter

This filter was developed to remove obvious non-candidates. Prior to applying the following cuts, the vertex cell where the reaction took place was determined as follows. The most upstream plane in a most upstream three consecutive calorimeter plane hits was defined as the vertex module. The cell having a hit in the vertex plane was defined as the vertex cell.

1. Fiducial Cuts

Loose fiducial cuts were applied to reject the beam associated front entering muons and side entering cosmic rays by using the calorimeter hit information. We rejected events,

(a) if the vertex plane was in the first 5 modules or in the last 10 modules of the main detector.

(b) if the vertex cell was in the first or last cell of the calorimeter plane (cell#-1 or 16).

2. Event Size Cut

We rejected events with less than 15 calorimeter planes hits within the first 20 modules starting from the vertex. And events with more than 4 consecutive missing hits of the calorimeter planes in the first 20 modules were also rejected. This cut was aimed to select events having a long muon.

3. Minimum Energy Cut

The total visible energy deposited in the calorimeters of an

event must be greater than 1 GeV. This minimum energy cut was applied because background events coming from the reaction $\nu_\mu n \rightarrow \mu^- p \pi^o$ become serious in the lower shower energy region. The visible energy means the fraction of the deposited energy that is detected and measured in the calorimeter. Due to the presence of non-active materials like Alminum of the PDTs and lucite of the calorimeter tubes, 73 % of the energy of an electromagnetic shower is visible. Therefore the visible energy of 1 GeV is equivalent to the corrected total energy of 1.43 GeV.

From the initial data of 5.34×10^5 bursts, 61,000 events passed the "μe"-filter. Reduction rate of this step was about 10 %. Efficiency of the "μe"-filter was found to be $.99 \pm .01$.

Figure 3.4 shows a distribution of the total visible energy versus shower energy by using the data which survived the eye scanning. According to this figure, if 1 GeV cut of the total visible energy was changed to 1.1 GeV, then one event was lost out of 126 events in the shower energy region greater than 1 GeV. Therefore the systematic error due to the energy calibration was less than 1%.

3.1.3 Eye scanning and kinematical cuts

The resulting events which had survived the "μe"-filter were double-scanned by physicists. In the scanning, only events with one muon-like track and one shower-like pattern were selected. Shower-like pattern was identified by the hit pattern of X and Y-PDT's and calorimeter cells. The shower can originate from the

vertex ("μe" event), which is shown in Figure 3.5. The shower pattern can also appear downstream of the vertex as long as it appears to be associated with the original point of the muon-like track ("$\mu\gamma$" event). An example is shown in Figure 3.6.

The "$\mu\gamma$" event were used to determine the π^0 background described in the next section. Candidates for $\nu_H \rightarrow \mu e \nu_\ell$ (ℓ=e or μ) were expected to have only a muon and an electron shower originating from a common vertex, but events initially with an additional short track at the vertex were also kept for more general search of "μe" productions.

Criteria of the scanning were as follows ;

1. there must be one track with a length of more than 20 modules measured in terms of calorimeter planes, which corresponds about 3 collsion lengths, showing neither interaction nor scattering in the detector (muon track candidates),

2. there must be an electromagnetic shower having a size of more than 10 modules pointing back to the vertex (e or γ candidates),

3. additional short tracks at the common vertex were allowed, provided that their length was less than 5 modules, because there was a possibility of nuclear reactions,

4. isolated calorimeter hits (extra stubs) having more than 2 modules anywhere in the detector were rejected as overlap-

ping events, and

5. the vertex PDT cell, which was defined as having a PDT hit behind the vertex plane and closest to the vertex cell, was restricted to be between 7th and 50th PDT cell in both XZ and YZ-views to reject side entering muons.

We have calculated the scanning efficiency for each scanner by using flags set at the double scanning. Then the overall efficiency of 0.962 ± 0.030 was obtained. Systematic errors of the scanning efficiency were studied in the following way. According to the calculated individual scanning efficiency, the two lowest scanning efficiencies were 0.562 and 0.654. In the double scanning, any pair of scanners scanned at most 20 % of the whole data. If the two scanners with the lowest efficiency scanned 20 % of the whole data, then 3 % of the data would have been lost. Therfore 3 % systematic error was set for the scanning efficiency. Since this error is conservative, it could well cover the uncertainty of the scanning.

After the scanning, projected angles in both XZ and YZ-view were measured. The angle resolution was studied by using the Monte Carlo events and was found to be 0.02 radian. Then the following kinematic variables were obtained.

1. The muon angle with respect to the beam direction (long track) in both XZ- and YZ-view.
2. Angle of the shower in both XZ- and YZ-view.
3. Muon length in module numbers.

4. Distance between the common vertex and the beginning of the shower in the modules. (Conversion Distance)

5. Visible energy of the shower was calculated by

$$E_{shower} = E_{total} - E_{\mu} \qquad (3\text{-}1)$$

where E_{shower}, E_{total} and E_{μ} are the shower energy, total energy of the TCL and the kinetic energy of the muon in MeV, respectively. The kinetic energy of the muon E_{μ} was obtained by

$$E_{\mu} = E_{min} \cdot L_{\mu}/\cos\theta_{\mu} \qquad (3\text{-}2)$$

where E_{min} is deposited energy in a module by the muon which is a minimum ionizing particle and roughly equals to 12 MeV per module, L_{μ} is the muon length in module numbers and θ_{μ} is the polar angle of the muon.

After those measurements, bad data having too many or no CAMAC records which were mainly due to the hardware errors of the microprocessors, were rejected.

In the next step, only events having a muon-like track without any interaction or scattering. The projected kink angles in both XZ and YZ-views were required to be less than 5 degrees. The resulting events were reduced down to 404 events by applying additional minimum opening angle cut of 0.05 radian. This cut was aimed to make a clear determination of the shower conversion point. Further kinematical cut, muon length of 4 collision lengths, was applied and a primary sample of 387 events was obtained from 5.34×10^5 bursts (3.78×10^{18} P.O.T.).

It contains two different classes of events, 140 "μe"-event

in which a shower is connected to the vertex and 247 "$\mu\gamma$"-event in which a shower is not connected to the vertex. Since the identification of the showers was more definitive in higher energy region, the cut of 1 GeV was implemented on the sample. After the above energy cut, we obtained 123 samples of single-shower events in total (**single-shower sample I**), of which 46 events were of "μe" type while 77 events were of "$\mu\gamma$" type.

From that, subsample was obtained by applying 2 GeV shower energy cut (**single shower sample II**). The resulting 49 contained 18 "μe" and 31 "$\mu\gamma$" events.

To obtain a sample to be used for a search for the heavy neutrino decays, further scanning on the single shower sample I was performed. Since the heavy neutrino decay does not produce any spurious tracks at the vertex other than a single muon and a single shower, then the events having an additional track longer than two modules at the vertex were threw away. The resulting ν_H sample contained 43 events (ν_H **sample**), in which there were 17 "μe" and 26 "$\mu\gamma$" events.

The final numbers of the three samples are summarized in Table 3.1.

We summarize the category of the final event samples used for searches for heavy neutrinos and anomalous μe events :

1. Single-shower sample I (E_{sh} > 1 GeV)

This sample was selected by applying loose cuts, and used to search for general anomalous μe events. Events classified into this sample show a long straight track and an electromagnetic shower in the final state. The energy of the shower was required

to be greater than 1 GeV. Events with an additional short track at the vertex, of which length was less than 5 modules, were kept.

2. Single-shower sample II (E_{sh} > 2 GeV)

This sample is a subset of the sample I with higher energy cut of 2 GeV. This was used to make direct comparison with anomalous μe events reported by Faissner et al. [1.26].

3. ν_H sample (E_{sh} > 1 GeV with clean vertex)

This sample was selected for a search of heavy neutrino decays. Only events showing a clean vertex are selected from the sample I.

In addition, we selected events which contain one muon-like track and two shower-like patterns. They were used as a control sample to study π^o background, which will be discussed in the next chapter. An example is shown in Figure 3.7. The data used for this event selection contains 2.87×10^5 bursts (2.02×10^{18} P.O.T.), which is a part of the data used to obtain the single-shower sample.

The data reduction flow of the two-shower sample is shown in Figure 3.8. The surviving 34,000 events after the "μe"-filter were scanned for this purpose. Criteria of the scanning for the two-shower sample were the same as those for the single-shower sample except we required two electromagnetic showers in an event. After the eye scanning, we obtained 157 events (Two-shower sample), which contain 314 γ's since each event has two γ's. Out of 314 γ's, only 311γ's remained after applying the opening angle cut of 0.05 radian.

§3.2 Backgrounds

There are several sources of background which mimic μe events. Main sources of the backgrounds come from charged current π^0 production, including Dalitz decay of π^0. And also ν_e-induced charged current π^+ production channels contribute to a background. Contributions from semileptonic decays of charmed particles and ν_μ-induced charged current π^+ production were found to be negligible.

In the following the detailed descriptions for each background are given.

3.2.1 π^0 background

The major background from the reaction $\nu_\mu n \rightarrow \mu^- p \pi^0$ was determined empirically. The reactions producing a short track of the proton accompanying π^0, where one decay γ converts close to the vertex and the other one is lost, simulate μe events, as shown in Figure 3.9.

Since a γ which converts close to the vertex can hardly be distinguished from an electron shower, the distribution of the distance between the vertex and the beginning of the shower (conversion distance) is plotted. The conversion distance of γ's is supposed to be on an exponential line. Since an electron is emitted from the vertex, the conversion distance of the electron is zero.

Figures 3.10, 3.11, 3.12 and 3.13 show the conversion distance distributions of the single-shower sample I, II, ν_H sample

and the two-shower sample that is used to estimate the γ background in the first bin in which the true electrons exist as excess events. In these figures three modules are combined to make one bin.

One parameter fitting applied to the data between 2nd and 6th bin of the conversion distance distribution, with a calculated conversion length of 5.94 modules, extrapolated to the first bin, gives us the number of background coming from γ's in the first bin.

The following formula with one free parameter N_o is assumed;

$$Y = N_o \cdot EXP(- X/\lambda) \qquad (3\text{-}3)$$

where N_o is a normalization factor, λ and X are the conversion length and the conversion distance of γ measured in an unit of module. Since the contribution of the vertex module is half a module on an average, the number of γ's contained in the first bin can be obtained by integrating (3-3) from X = 0 to X = 2.5.

$$N_\gamma^{1st\ bin} = \frac{N_o}{3} \int_o^{2.5} EXP(- X/\lambda) \, dX$$

$$= \frac{\lambda N_o}{3} \cdot (1 - EXP(-2.5/\lambda)) \qquad (3\text{-}4)$$

The nomalization factor $N_o/3$ instead of N_o reflects the fact that three modules are combined for one bin.

We extracted μe events by subtracting those π^o background

by using the formula,

$$N_e = (N_{all}^{1st\ bin} \pm \Delta N_{all}^{1st\ bin}) - (N_{\gamma}^{1st\ bin} \pm \Delta N_{\gamma}^{1st\ bin})$$

$$= (N_{all}^{1st\ bin} - N_{\gamma}^{1st\ bin}) \pm ((\Delta N_{all}^{1st\ bin})^2 + (\Delta N_{\gamma}^{1st\ bin})^2)^{1/2} \qquad (3\text{-}5)$$

,where

$$\Delta N_{all}^{1st\ bin} = (N_{all}^{1st\ bin})^{1/2}$$

and

$$\Delta N_{\gamma}^{1st\ bin} = N_{\gamma}^{1st\ bin} \cdot (1/\int_{n_f}^{n_\ell} N_o \cdot EXP(- X/\lambda) \, dX)^{1/2}$$

(n_f, n_ℓ : the first and last bin used in the fitting). The first error is statistical and the second one reflects error due to the fitting procedure.

The excesses of μe events thus obtained are given in Table 3.2, together with the number of subtracted γ's in the first bin.

The dotted lines in Figures 3.10, 3.11, 3.12 and 3.13 show the contribution from the π^o background, which were obtained from the one parameter fitting.

The resulting excesses in all the three samples listed in Table 3.2 are 2.7, 1.7 and 2.0 standard deviation effects, which will be further studied in the following sections. In the two-shower sample the excess is consistent with zero. This proves that the background having one muon-like track and two showers really comes from the muon associated π^o production and causes no contribution to the excess.

In order to estimate the uncertainty of the γ conversion

length, of which the designed value is 5.94 modules, we performed a two parameter fitting for the conversion distance distributions by assuming both N_0 and λ as free parameters in the formula of eq.(3-3). Two samples, one before 1 GeV cut [Figure 3.14] and the other with two showers [Figure 3.13] were used in this study, since they were independent and had relatively high statistics. The resulting conversion length are 6.12 $\pm$ 0.63 and 6.66 $\pm$ 0.81 modules respectively.

Accordingly, the assigned systematic error of 15% to the conversion length covers those uncertainty. This results in systematic error of 25% for the excess events. The number of excesses of the three different samples for assumed three conversion lengths are shown in Table 3.3.

3.2.2 Dalitz decay of π^o

Dalitz decay of π^o produced by $\nu_\mu n \rightarrow \mu^- p \pi^o$ interactions,

$$\begin{aligned} \nu_\mu + n &\rightarrow \mu^- + p + \pi^o \\ &\rightarrow e^+ + e^- + \gamma \end{aligned} \qquad (3\text{-}6)$$

could contribute a background, having a proton track of length less than 5 modules, with one decay γ lost [Figure 3.15]

Assuming all the γ events in the shower sample, denoted by $N_{\mu\gamma}$, come from the reactions $\nu_\mu n \rightarrow \mu^- p \pi^o$, the number of Dalitz decay in the sample can be estimated by

$$N_{Dalitz} = Br(\pi^o \rightarrow e^+ e^- \gamma) \cdot \frac{N_{\mu\gamma}}{2\varepsilon_\gamma(1-\varepsilon_\gamma)} \cdot (1-\varepsilon_\gamma) \qquad (3\text{-}7)$$

,where $Br(\pi^o \rightarrow e^+ e^- \gamma)$ is the branching ratio of 1.2 % and ε_γ is the detection efficiency of a γ,

$$\varepsilon_\gamma = 0.6 \pm 0.3 \qquad (3\text{-}8)$$

including the geometrical acceptance of the detector which was estimated by a Monte Carlo. For single-shower sample I,

$$\begin{aligned} N_{\mu\gamma} &= (123 \pm 11.1) - (24.5 \pm 9.0) \\ &= 98.5 \pm 15.5 \text{ events.} \end{aligned} \qquad (3\text{-}9)$$

The results for three samples are given in Table 3.4.

3.2.3 ν_e-induced interaction

Charged current pion productions by electron neutrinos,

$$\nu_e + p \rightarrow e^- + p + \pi^+ \qquad (3\text{-}10)$$

$$\nu_e + n \rightarrow e^- + n + \pi^+, \qquad (3\text{-}11)$$

where pion fakes muon, may contribute to the background, although electron neutrino flux (ϕ_{ν_e}) is small compared to the muon neutrino flux (ϕ_{ν_μ}) as shown in Figures 2.6 and 2.7. Their contribution was estimated using the Monte Carlo simulations.

The numbers of those events corresponding to our data sample were calculated to be

$$N_{e^-p\pi^+} = 810.5 \text{ events} \qquad (3\text{-}12\text{-}1)$$

and

$$N_{e^-n\pi^+} = 292.5 \text{ events.} \qquad (3\text{-}12\text{-}2)$$

The cross sections for $\nu_e N \rightarrow e^- N \pi^+$ (N=p or n) were assumed to be the same as $\nu_\mu N \rightarrow \mu^- N \pi^+$ (N=p or n), which are based on the Rein-Sehgal model [3.1], and shown in Figure 3.16.(a) and (b) as a function of the neutrino energy. Flux integrated cross sections for each reaction $\nu_e N \rightarrow e^- N \pi^+$ (N=p or n) are calculated to be

$$\int_{E_\nu^{th}}^{10} \phi_{\nu_e} \cdot \sigma(e^- p \pi^+)\, dE_\nu = 7.42 \times 10^{-35} \quad (/10^{13}\text{P.O.T.}) \qquad (3\text{-}13\text{-}1)$$

$$\int_{E_\nu^{th}}^{10} \phi_{\nu_e} \cdot \sigma(e^- n \pi^+)\, dE_\nu = 3.40 \times 10^{-35} \quad (/10^{13}\text{P.O.T.}), \qquad (3\text{-}13\text{-}2)$$

where E_{ν}^{th}, the threshold energy, is 0.15 GeV.

As shown in Figures 3.17.(a) and (b), 4000 Monte Carlo events in each of these two channels were passed through the same data reduction processes. The constraint on the length of a track to be longer than 4 collision lengths considerably reduced the background of this kind. The number of background from ν_e reactions were obtained by

$$N_{bg} = N_{ob} \times \frac{N_{e^-p(n)\pi^+}}{4000 \times 0.6} \qquad (3\text{-}14)$$

, where N_{ob} is the surviving events after the reduction. The value of 0.6 is the ratio of the fiducial volume to the full detector. The results are given in Table 3.5. Errors show systematic uncertainties, i.e., 15% coming from the neutrino flux uncertainty and 10% from the number of targets (p or n), 20% from the cross sections of single pion productions, 10% from P.O.T. and the statistics of the Monte Carlo.

3.2.4 Charmed baryon (Λ_c^+) production

A charged charmed baryon (Λ_c^+) production with a subsequent semileptonic decay into an electron appears as genuine μe events. The background from Λ_c^+ production is greatly suppressed because the events with more than two long tracks at the vertex were rejected. The integrated neutrino flux above the Λ_c^+ production threshold (E_ν^{th} = 2.56 GeV assuming $m_{\Lambda_c^+}$ = 2282 MeV) was evaluated to be only 10% of the total.

The number of Λ_c^+ produced in the detector was calculated to be

$$N_{\Lambda_c^+} = 1325 \pm 380 \text{ events.} \qquad (3\text{-}15)$$

The cross section of $\nu_\mu n \rightarrow \mu^- \Lambda_c^+$ and various branching ratios are adopted from theoretical calculations [3.2] and are given in Figure 3.18 and Table 3.6, respectively. The flux integrated cross section of $\nu_\mu n \rightarrow \mu^- \Lambda_c^+$ was calculated to be

$$\int_{E_\nu^{th}}^{\infty} \phi_{\nu_\mu} \cdot \sigma(\mu^- \Lambda_c^+) \cdot dE_\nu = 1.54 \times 10^{-34} \quad [/10^{13} \text{P.O.T.}]. \qquad (3.16)$$

The errors shown in Table 3.7 include the systematic uncertainties from ϕ_{ν_μ}, $\sigma(\mu^- \Lambda_c^+)$, the number of neutrons and P.O.T., of which the values are 15%, 20%, 10% and 10%, respectively.

Subsequent decays such as

$$\nu_\mu n \rightarrow \mu^- \Lambda_c^+$$

$$\rightarrow \Lambda^o e^+ \nu_e$$

$$\rightarrow p\pi^- \qquad (3.17.1)$$

$$\rightarrow n\pi^o \qquad (3.17.2)$$

$$\rightarrow ne^+\nu_e \qquad (3.17.3)$$

were then evaluated. The resultant numbers of background events coming from each decay process of Λ_c^+ were given in Table 3.7 together with the acceptance and branching ratios. The systematic error of the acceptance and branching ratio amounted to be 52.2%.

3.2.5 Charge exchange process

Charged current $\pi^{\pm}$ production in which produced pion undergoes a charge exchange reaction producing π^{o} fakes an electron shower originating from the vertex. The contribution of this process was estimated by generating Monte Carlo events.

The cross sections $\sigma(\mu^{-}p\pi^{+})$ and $\sigma(\mu^{-}n\pi^{+})$, used to calculate the number of $\mu^{-}p\pi^{+}$ and $\mu^{-}n\pi^{+}$ events are based on the Rein-Sehgal model [3.1]. To meet the scanning criteria, a cut of 5 degree on θ_{γ}, measured angle with respect to the π^{+} incident direction, was applied. We have not observed any event satisfied this angle cut. The background coming from the charge exchange process was found to be negligible.

§3.3 Final Events (Excesses)

The background events of each process and the remaining number of events for the three final samples are summarized in Table 3.8. The remaining backgrounds in the excess μe events after subtracting the π^0 backgrounds are 7.8 ± 2.0, 3.6 ± 1.2 and 4.5 ± 1.3 events for the single-shower sample I, II and ν_H sample, respectively. The final excesses, which were corrected for the efficiency of the filter and the scanning, are

17.5 ± 9.5 ± 6.4 events (shower sample I),

6.9 ± 6.2 ± 2.8 events (shower sample II) and

6.8 ± 5.8 ± 3.1 events (ν_H sample),

respectively. The first errors mean the statistical uncertainty and the second ones mean the systematic uncertainty. Considering the statistical and systematic errors, these results are consistent with null excess. Therefore we conclude we have obseved no significant excess or anomaly beyond the level expected from the known processes.

Chapter 4. RESULTS ON SEARCHES FOR ν_H AND ANOMALOUS μe EVENTS

§4.1 Heavy Neutrino Searches and Limits on Mixing Matrix Elements

Not having observed any significant evidence of the heavy neutrino decay, upper limits were set on the mixing matrix elements squared $|U_{He}|^2$ and $|U_{H\mu}|^2$. Here, the general descriptions with respect to the production and decay of the heavy neutrinos are given.

The energy of the AGS proton beam (30 GeV) is not high enough to produce charmed particles. Therefore only pions and kaons are possible origins of heavy neutrinos. Thus the mass of the heavy neutrinos are constrained to be below $m_\pi - m_\ell$ and $m_K - m_\ell$, ℓ = e or μ, respectively. The decay $\pi^+ \rightarrow \mu^+ \nu_H$ does not contribute, because the maximum mass of the produced neutrino is $m_{\pi^+} - m_{\mu^+} = 34$ MeV which is lower than $m_\mu + m_e = 106$ MeV, for $\nu_H \rightarrow \mu e \nu_\ell$ (ℓ = e or μ) decay. The contribution from the decay $\pi^+ \rightarrow e^+ \nu_H$ is negligible due to the small acceptance of our apparatus to the heavy neutrino mass below 180 MeV to be described in the subsection 4.1.3. Accordingly, only the decay of ν_H produced from K^+ was searched for.

Feynmann diagrams of the heavy neutrino production processes from π^+ and K^+ are already shown in Figures 1.3.(a)-(d). The Feynmann diagrams of the decay $\nu_H \rightarrow \mu e \nu_\ell$, ℓ = e or μ, are shown in Figures 1.4.(a) and (b). The mixing matrix elements $|U_{H\ell}|$, ℓ = e or μ, contribute to the decay process as well as to the

production processes. In order to derive the upper limits, the heavy neutrino flux and the acceptance of the decay particles, which will be described in the following subsections in detail, are needed.

4.1.1 Decay probability of the heavy neutrinos

If we substitute $\nu_H \rightarrow \mu$, $\mu \rightarrow \nu$ in Figure 1.4.(a), then the decay $\nu_H \rightarrow \mu e \nu_\ell$ are identical to the muon decay shown in Figure 1.4.(c), except for the fact that the muon mass in the final state of the heavy neutrino decay is not negligible and affects the decay rate. The proper life time of ν_H, τ_{ν_H}, is obtained by using the muon proper life time τ_μ [1.19],

$$\tau_{\nu_H} = \tau_\mu \cdot (m_\mu / m_{\nu_H})^5 / |U_{H\ell}|^2 \cdot f(m_\mu / m_{\nu_H}) \qquad (4\text{-}1)$$

where $f(X) = 1 - 8X^2 + 8X^6 - X^8 - 12X^4 \ln X^2$ is the phase space factor, which is monotonically increasing as m_{ν_H} increase. Since we are looking for small values of $|U_{H\ell}|^2$, eq.(4-1) ensures that heavy neutrinos are not disapeared in the flight path ($\sim$ 100 m) from the production target to our detector.

The probability of the decay $\nu_H \rightarrow \mu e \nu_\ell$ with the energy E_{ν_H} within our detector is given by :

$$P = \frac{m_{\nu_H}}{E_{\nu_H}} \cdot \frac{L}{c\tau_{\nu_H}} \quad \text{for} \quad c\tau_{\nu_H} >> L \qquad (4\text{-}2)$$

where τ_{ν_H} is the proper life time obtained in eq.(4-1), L[m] is the length of our detector. The factor of m/E is the effect of the Lorentz boost. It is clear from eq.(4-2) that the lower the energy of ν_H, the more abundant the decays of ν_H is.

The number of heavy neutrino decays expected in the detector is written as :

$$N_{decay} = \int \phi_{\nu_H}(E_{\nu_H}, m_{\nu_H}) \cdot P \cdot \varepsilon(E_{\nu_H}, m_{\nu_H}) dE_{\nu_H} \qquad (4\text{-}3)$$

where P is given by eq.(4-2). ϕ_{ν_H} is the energy spectrum of heavy neutrinos to be obtained by eq.(4-5) in the subsection 4.1.2. ε is the detector acceptance for the decays of $\nu_H \to \mu e \nu_\ell$. More explicitly eq.(4-3) is written as :

$$N_{decay} = \sum_{M=\pi,K} \sum_{\ell=e,\mu} \sum_{\ell'=e,\mu} \int |U_{H\ell}|^2 \cdot |U_{H\ell'}|^2 \cdot \phi_{M,\nu_\ell}(E_{\nu_H}, m_{\nu_H}) \cdot \bar{\rho}_{M,\ell}(m_{\nu_H}) \cdot \varepsilon(E_{\nu_H}, m_{\nu_H}) \cdot f(m_\mu/m_{\nu_H}) \cdot m_{\nu_H}^6 \cdot L/E_{\nu_H}/\tau_\mu/m_\mu^5 \cdot dE_{\nu_H} \qquad (4\text{-}4)$$

The acceptance ε for the decay $\nu \to \mu e \nu_\ell$, ℓ = e or μ, will be described in the subsection 4.1.3.

4.1.2 Heavy neutrino spectrum

Heavy neutrinos are assumed to be produced in the decays of $K^+ \to e^+\nu_H$ and $K^+ \to \mu^+\nu_H$ through the mixing of ν_H with ν_e or/and ν_μ whose mixing strength is characterized by $|U_{He}|^2$ and $|U_{H\mu}|^2$, respectively. The energy spectrum of heavy neutrinos $\phi_{\nu_H}(E_{\nu_H}, m_{\nu_H})$ is obtained by the following formula [1.19]:

$$\phi_{\nu_H}(E_{\nu_H}, m_{\nu_H}) = \sum_{M=\pi,K} \sum_{\ell=e,\mu} \phi_{M,\nu_\ell}(E_{\nu_H}, m_{\nu_H}) \cdot |U_{H\ell}|^2 \cdot \bar{\rho}_{M,\ell}(m_{\nu_H}) \qquad (4\text{-}5)$$

where $\phi_{M,\nu_\ell}(E_{\nu_H}, m_{\nu_H})$ is known energy spectrum from the decay $M \to \ell + \nu_\ell$ ($M = \pi, K$) except $m_{\nu_H} \neq 0$, $|U_{H\ell}|^2$ is a mixing matrix element and $\bar{\rho}_{M,\ell}(m_{\nu_H})$ is a kinematic factor given in terms of the ratio of masses squared m_ℓ^2/m_M^2 and $m_{\nu_H}^2/m_M^2$ and vanishes for $m_{\nu_H} \geq m_M - m_\ell$, which is described in detail in APPENDIX A.

The behavior of $\bar{\rho}$ as a function of m_{ν_H} is shown for the decays $\pi^+ \to \mu^+\nu_H$, $\pi^+ \to e^+\nu_H$, $K^+ \to \mu^+\nu_H$ and $K^+ \to e^+\nu_H$ in Figures 4.1.(a)-(d), respectively. As shown in those figures, the rates of the π/K decay into the electron and heavy neutrino are enhanced (i.e. $\bar{\rho} >> 1$) except at small mass region where helicity suppression takes effect, while that into massless neutrinos is strongly suppressed.

According to eq.(4-5), energy spectra of heavy neutrinos can be expressed explicitly by the following formula :

$$\phi_{\nu_H}(E_\nu, m_\nu) = \phi_{K^+;\nu_e}(E_\nu, m_\nu) \cdot |U_{He}|^2 \cdot \bar{\rho}_{K^+;e}(m_\nu) \qquad (4\text{-}6\text{-}1)$$

for the decay mode of $K^+ \rightarrow e^+ \nu_H$,

$$\phi_{\nu_H}(E_\nu, m_\nu) = \phi_{K^+;\nu_\mu}(E_\nu, m_\nu) \cdot |U_{H\mu}|^2 \cdot \bar{\rho}_{K^+;\mu}(m_\nu) \qquad (4\text{-}6\text{-}2)$$

for the decay mode of $K^+ \rightarrow \mu^+ \nu_H$.

The heavy neutrino spectra ϕ_{ν_H} given by eqs.(4-6-1) and (4-6-2) are calculated by using the extended version of NUBEAM [4.2], which generates all species of neutrino through the decay of parent particles with appropriate weights. The main modification in the extended version is to ascribe a finite mass to the neutrino.

The heavy neutrino spectra divided by the mixing matrix element $\phi_{\nu_H}/|U_{He}|^2$ for $K^+ \rightarrow e^+ \nu_H$, with several masses from 200 to 470 MeV, are shown in Figures 4.2.(a)-(g). Similarly $\phi_{\nu_H}/|U_{H\mu}|^2$ for $K^+ \rightarrow \mu^+ \nu_H$ with several masses from 200 to 370 MeV are shown in Figures 4.3.(a)-(e).

4.1.3 Acceptance

In order to obtain the number of heavy neutrino decays expected in the detector, the acceptance $\varepsilon(E_\nu, m_{\nu_H})$ of the decay particles (i.e. a muon and an electron in the final state) was estimated by using a Monte Carlo calculation as a function of the heavy neutrino energy and mass. In the Monte Carlo program,

decay products were generated according to the three-body phase space neglecting the effect of polarization of the heavy neutrinos. The kinematic cuts, applied to the generated events, were equivalent to the selection criteria applied to the data.

The acceptance for heavy neutrinos with several masses are shown in Figures 4.4.(a)-(h). In the low energy region the acceptance is limited by the 1 GeV energy cut, while in the high energy region it is limited by the requirement of the 0.05 radian opening angle (mentioned in 3.1.3) between the muon and electron. The opening angle cut reduces the acceptance for lighter mass neutrinos and sets a low mass limit of 180 MeV on this search.

The systematic errors due to the kinematic cuts were evaluated by varying the cuts within reasonable amounts. The energy cut was varied up to 15% of 1 GeV and the opening angle from 0.03 to 0.07 radian. The resultant variation of the acceptance are shown in Figures 4.5.(a)-(h) and in Figures 4.6.(a)-(h), respectively. As shown in Figures 4.6.(a)-(h), the change due to the opening angle cut are significant especially in the high energy region. However, this variation does not contribute directly to the systematic error of the expected number of heavy neutrino decay events, because the higher energy the heavy neutrino has, the smaller the decay probability becomes.

In view of eq.(4-4), a flux averaged acceptance is calculated as :

$$\bar{\varepsilon}(m_{\nu_H}) = \frac{1}{\alpha} \int \phi_{M,\nu_\ell}(E_\nu, m_{\nu_H}) \cdot \varepsilon(E_\nu, m_{\nu_H}) / E_\nu \cdot dE_\nu \qquad (4\text{-}7)$$

$$\alpha = \int \phi_{M,\nu_\ell}(E_\nu, m_{\nu_H}) / E_\nu \cdot dE_\nu$$

where $1/E_\nu$ comes from the relativistic effect of the decay probability and α is a nomalization factor. Figure 4.7.(a) and (b) show $\bar{\varepsilon}$ as a function of the heavy neutrino mass m_{ν_H} with the systematic errors estimated from the energy and opening angle variations.

4.1.4 Upper Limits

The final number of events obtained for the ν_H sample is 6.8 ± 6.6, as described in the previous chapter. The statistical and systematic errors were summed in quadrature. Since no significant excess was obtained, the results of this experiment were expressed as upper limits on $|U_{H\ell}|^2$, ℓ = e or μ. In order to obtain the upper limits on the mixing matrix elements, we decompose the eq.(4-4) explicitly as a function of $|U_{H\mu}|^2 (\equiv X)$ and $|U_{He}|^2 (\equiv Y)$ like

$$AX^2 + (A+B)XY + BY^2 = C, \qquad (4\text{-}8)$$

where

$$A = \int \phi_{K,\nu_\mu}(E_{\nu_H}, m_{\nu_H}) \cdot \bar{\rho}_{K,\mu}(m_{\nu_H}) \cdot \varepsilon(E_{\nu_H}, m_{\nu_H}) \cdot f(m_\mu / m_{\nu_H}) \cdot m_{\nu_H}^6 \cdot L / E_{\nu_H} / \tau_\mu / m_\mu^5 \cdot dE_{\nu_H} \qquad (4\text{-}9)$$

and

$$B = \int \phi_{K,\nu_e}(E_{\nu_H}, m_{\nu_H}) \cdot \bar{\rho}_{K,e}(m_{\nu_H}) \cdot \varepsilon(E_{\nu_H}, m_{\nu_H}) \cdot f(m_\mu/m_{\nu_H}) \cdot m_{\nu_H}^6 \cdot L/E_{\nu_H}/\tau_\mu/m_\mu^5 \cdot dE_{\nu_H} \quad (4\text{-}10)$$

and C is the observed number of events in the ν_H sample.

The contours of upper limits at 90% C.L. on the mixing matrix elements squared in the $|U_{H\mu}|^2$ and $|U_{He}|^2$ space were calculated by χ^2-method. We defined the χ^2 as :

$$\chi^2 = \frac{(F(X,Y) - F(X_o,Y_o))^2}{\sigma^2_{F(X_o,Y_o)}} \quad (4\text{-}11)$$

where

$$F(X,Y) = AX^2 + (A+B)XY + BY^2 - C \quad (4\text{-}12)$$

and A, B and C are constants having the errors ΔA, ΔB and ΔC, and $\sigma_{F(X_o,Y_o)}$ is the error at $(X,Y) = (X_o,Y_o)$ defined by :

$$\sigma^2_{F(X_o,Y_o)} = (X_o^2 + X_oY_o)^2(\Delta A)^2 + (Y_o^2 + X_oY_o)^2(\Delta B)^2 + (\Delta C)^2 \quad (4\text{-}13)$$

where (X_o,Y_o) satisfies $F(X_o,Y_o) = 0$.

As the degree of freedom is two, the value $\chi^2 = 3.22$ corresponds to 90% C.L. upper limit according to the eq.(4-11). The results of 90% C.L. upper limits on the mixing matrix elements for several heavy neutrino masses are drawn in the $|U_{H\mu}|^2$ and

$|U_{He}|^2$ space, which is shown in Figure 4.8.(a). In this figure the region outside the contour of 90% C.L. upper limit in the $|U_{H\mu}|^2$ and $|U_{He}|^2$ space is excluded.

To compare these results with other experiments which only determined the limit for a single mixing matrix element squared, we calculated the upper limits for each mixing matrix element, $|U_{H\mu}|^2$ and $|U_{He}|^2$, assuming that the other one is zero. In this case the degree of freedom is one, then χ^2 = 1.64 corresponds to 90% C.L.. These results are shown in Figures 4.8.(b) and (c), together with previous experimental results. The results are also given in Table 4.1.

§4.2 Anomalous "μe" Search

For a possible anomaly search more general than ν_H hunt, we used both the single-shower sample I with 1 GeV cut and sample II with 2 GeV cut, of which the final number of events are 17.5 ± 11.5 and 6.9 ± 6.8, respectively. The statistical and systematic errors were summed quadratically. Although the result of the single-shower sample I exhibit about 1.5σ effect, it is hardly to be considered as new phenomena rather than the statistical fluctuation. In the absence of any positive signature, upper limits for the existence of an anomaly in "μe" events were set in this search by using the remaining events.

In order to normalize "μe" events, the number of all charged current interactions $N_{\nu_\mu N\to\mu^- X}$ occurred in our detector was evaluated. The method to calculate the number of all charged current interactions is basically the same as that used repeatedly in the previous chapter to estimate the number of background events which occurred in our detector. $N_{\nu_\mu N\to\mu^- X}$ was calculated as a sum of $N_{\nu_\mu n\to\mu^- X}$ and $N_{\nu_\mu p\to\mu^- X}$, then

$$\begin{aligned} N_{\nu_\mu N\to\mu^- X} &= N_{\nu_\mu n\to\mu^- X} + N_{\nu_\mu p\to\mu^- X} \\ &= 2.99 \times 10^5 + 1.61 \times 10^5 \\ &= (4.60 \pm 1.00) \times 10^5 \quad \text{events} \end{aligned} \tag{4-14}$$

The value of the cross sections $\sigma(\nu_\mu n\to\mu^- X)$ and $\sigma(\nu_\mu p\to\mu^- X)$, which were taken from the 7-foot bubble chamber experiment at BNL neutrino beam [4.2], were used to calculate the flux integrated

cross sections as described in Chapter 3. The systematic uncertainties are from the ϕ_{ν_μ}(15%), the cross sections(7%), the number of targets(10%) and P.O.T.(10%).

When the single-shower sample I is normalized to all charged current interactions of $(4.60 \pm 1.00) \times 10^5$, the rate for the production of anomalous "μe" events, $R_{\mu e}$, subject to the particular selection criteria discussed in chapter 3, is calculated to be :

$$R_{\mu e} = (3.8 \pm \begin{matrix} 2.9 \\ 2.5 \end{matrix}) \times 10^{-5} \qquad (4\text{-}15)$$

or

$$R_{\mu e} < 7.6 \times 10^{-5} \qquad (4\text{-}16)$$

for 90% C.L. upper limit [APPENDIX B], where 21.8% systematic uncertainty in the normalization is included.

Similarly if the single-shower sample II is normalized to all charged current interactions, the rate for the production of anomalous "μe" events becomes :

$$R_{\mu e} < 3.6 \times 10^{-5} \qquad (4\text{-}17)$$

for 90% C.L. upper limit.

Chapter 5. DISCUSSIONS AND CONCLUSIONS

Heavy neutrino search

We have observed no signals for the heavy neutrino decay $\nu_H \rightarrow \mu e \nu_\ell$ (ℓ = e, μ) and imposed upper limits at 90% C.L. on the mixing matrix elements squared $|U_{H\mu}|^2$ and $|U_{He}|^2$.

Various experiments have been performed to search for the massive neutrinos as is described in Chapter 1. In the mass region around a few hundred MeV experiments to search for heavy neutrino decays utilizing a neutrino beam have an advantage over spectroscopy experiments because of the large incoming neutrino flux. The sensitivity of our experiment are much better than those of beam dump experiments, where the distance between the production target and the detector is much longer than ours.

Therefore, our heavy neutrino search, in the mass range of 200 $\sim$ 500 MeV, could be able to obtain good upper limits on the mixing matrix elements squared $|U_{H\mu}|^2$ and $|U_{He}|^2$. Especially, the limit on $|U_{H\mu}|^2$ was improved considerably compared to the previous experiments. However, the better limit on $|U_{He}|^2$ was already reported by PS191 experimental group at CERN PS [4.3]. The reason that our experiment could not give better results compared to PS191, is due to existence of the background events caused in the detector material, since PS191 had no materials in the decay region and observed no candidates. Therefore the limits will be improved at least an order of magnitude if we pull out a part of scintillator planes to suppress the conventional neutrino interactions.

In our search for the heavy neutrino decays in the neutrino beam, there is no signature exhibiting the existence of such massive neutrinos. However, it is still natural to look for existence of massive neutrinos for various reasons. Therfore searches for heavy neutrinos should be promoted with much higher sensitivities in future.

Anomalous "μe" search

For a more general anomaly search of "μe" events, the data sample obtained with the loose cut on extra tracks around the vertex were used. We found no evidence.

We also found no evidence for the production of anomalous events in the data sample with higher shower energy greater than 2 GeV which is comparable to the Aachen-Padova experiment. They claimed an excess of "μe" events of :

$$R_{\mu e} = (6.9 \pm 2.5) \times 10^{-5}. \qquad (5\text{-}1)$$

An upper limit at 90 % C.L. was placed on the production rate on such events,

$$R_{\mu e} < 3.6 \times 10^{-5}. \qquad (5\text{-}2)$$

We did not confirm the anomalous "μe" events reported by the Aachen-Padova group.

Table 2.1

SUMMARY OF THE DETECTOR

LOCATION	Brookhaven National Laboratory, USA
INCIDENT BEAM	Neutrino Horn Focussed From 28 GeV Protons 110m from proton target
ASSEMBLY	Modular construction; each module consisting of a plane of calorimeter and two planes (x,y) of tracking proportional drift tubes 112 Modules + γ-Catcher + Spectrometer Weight 172 + 30 tons

MODULE PROPERTIES

CALORIMETER (LIQUID SCINTILLATOR)

Active Area 4.22×4.09 m^2 Thickness 7.9 cm

Weight (Liquid & Acrylic) 1.35 metric tons

16 cells/module 2 Amperex 2212A phototubes/cell

1 Pulse Height Measurement/2 Time Measurements Per Tube Readout

PROPORTIONAL DRIFT TUBES (PDT)

Active Area 4.2×4.2 m^2

Thickness (x and y) 7.6 cm 54 x wires 54 y wires

1 Pulse Height Measurement/2 Time Measurements Per Wire Readout

GAMMA CATCHER 10 standard calorimeter modules with 1 radiation length og lead between each module

30 metric tons target mass.

MUON SPECTROMETER 2m $\times$ 2m Aperture Muon Spectrometer

$$< \int B \cdot d\ell > = 70 \text{ MeV/c}$$

$$(\Delta p/p)^2 = (.10^2 + (.067p)^2) \quad p \text{ in GeV/c}$$

Table 2.2

Properties of the Liquid Scintillator Mixture

hydrogen/carbon ratio	1.93
index of refraction	1.47
optical absorption coefficient	0.58/m
density	0.858 gm/cm^3
absorption length	84 cm
radiation length	53 cm
mean dE/dx	1.79 MeV/cm

Table 3.1

Sample	Total	μe	$\mu\gamma$
Single-shower sample I	123	46	77
Single-shower sample II	49	18	31
ν_H sample	43	17	26

Table 3.2

Sample	Excess	Subtracted γ's
Single-shower sample I	24.5 ± 9.0	21.5 ± 11.3
Single-shower sample II	10.2 ± 5.9	7.8 ± 7.3
ν_H sample	11.0 ± 5.5	6.0 ± 6.9
Two-shower sample	-8.3 ± 12.9	94.3 ± 15.9

Table 3.3

Excess λ [module]	Single-shower sample I	Single-shower sample II	ν_H sample
5.05	17.4 ± 9.5	7.6 ± 6.2	8.7 ± 5.8
5.94	24.5 ± 9.0	10.2 ± 5.9	11.0 ± 5.5
6.83	29.0 ± 8.7	11.9 ± 5.7	12.5 ± 5.3

Table 3.4

Sample	N_{Dalitz}	$N_{\mu\gamma}$
Single-shower sample I	1.0 ± 0.5	98.5 ± 15.5
Single-shower sample II	0.4 ± 0.2	38.8 ± 9.5
ν_H sample	0.3 ± 0.2	32.0 ± 9.1

Table 3.5

Sample	Background $\langle e^- p \pi^+ \rangle$	Events $\langle e^- n \pi^+ \rangle$
Single-shower sample I	4.1 ± 1.7	.98 ± .45
Single-shower sample II	2.4 ± 1.1	.49 ± .28
ν_H sample	2.0 ± 1.0	.85 ± .40

Table 3.6

Mode	Branching Ratio
$\Lambda_c^+ \rightarrow e^+$ anything	4.5 ± 1.7 (%)
$\frac{\Gamma(\Lambda_c^+ \rightarrow e^+ n \nu_e)}{\Gamma(\Lambda_c^+ \rightarrow e^+ \Lambda^o \nu_e)}$	0.25 ± 0.05
$\Lambda^o \rightarrow p\pi^-$	64.2 ± 0.5 (%)
$\Lambda^o \rightarrow n\pi^o$	35.8 ± 0.5 (%)

Table 3.7

The upper, middle and lower numbers of each process are corresponding to the single-shower sample I, II and ν_H sample.

Process	Acceptance	Branching Ratio	B.G. Events
$\Lambda_c^+ \to ne^+\nu_e$	9.6×10^{-2}	0.009	1.1 ± 0.66
	1.0×10^{-1}	0.009	1.2 ± 0.72
	1.8×10^{-2}	0.009	0.21 ± 0.13
$\Lambda_c^+ \to \Lambda^o e^+\nu_e$	$< 10^{-4}$	0.023	0.0
$\to p\pi^-$	1.0×10^{-2}	0.023	0.30 ± 0.18
	2.5×10^{-3}	0.023	0.076 ± 0.045
$\Lambda_c^+ \to \Lambda^o e^+\nu_e$	1.3×10^{-2}	0.013	0.22 ± 0.13
$\to n\pi^o$	1.4×10^{-2}	0.013	0.24 ± 0.14
$\to \gamma\gamma$	1.6×10^{-3}	0.013	0.028 ± 0.017

Table 3.8

Excess 1 means that the excess after subtracting π^o background, Excess 2 means that the excess after subtracting all other background and Excess 3 means that the excess after crrections for the filter and scanning.

Sample	Single-shower sample I	Single-shower sample II	ν_H sample
Excess 1	24.5±9.0±6.1	10.2±5.9±2.6	11.0±5.5±2.8
$e^-p\pi^+$	4.1 ± 1.7	2.4 ± 1.1	2.0 ± 1.0
$e^-n\pi^+$	0.98 ± 0.45	0.49 ± 0.28	0.85 ± 0.40
$\Lambda_c^+ \rightarrow ne^+\nu_e$	1.2 ± 0.72	0.21 ± 0.13	1.1 ± 0.66
$\Lambda_c^+ \rightarrow \Lambda^o e^+ \nu_e$ $\rightarrow p\pi^-$	0.30 ± 0.18	0.076 ± 0.045	0.0
$\Lambda_c^+ \rightarrow \Lambda^o e^+ \nu_e$ $\rightarrow n\pi^o$ $\rightarrow \gamma\gamma$	0.24 ± 0.14	0.028 ± 0.017	0.22 ± 0.13
$\pi^o \rightarrow e^+e^-\gamma$	1.0 ± 0.5	0.4 ± 0.2	0.3 ± 0.2
Excess 2	16.7±9.0±6.4	6.6±5.9±2.8	6.5±5.5±3.1
Excess 3	17.5±9.5±6.4	6.9±6.2±2.8	6.8±5.8±3.1

Table 4.1

Mass [MeV]	$\|U_{H\mu}\|^2$	$\|U_{He}\|^2$
200	2.28×10^{-6}	2.75×10^{-6}
250	3.20×10^{-7}	4.20×10^{-7}
300	1.10×10^{-7}	1.35×10^{-7}
350	4.44×10^{-8}	5.71×10^{-8}
370	3.41×10^{-8}	4.39×10^{-8}
400		3.05×10^{-8}
450		2.56×10^{-8}
470		3.69×10^{-8}

APPENDIX A. Kinematic Factor ($\bar{\rho}$)

The decay rate for the mode $M^+ \to \ell^+ \nu_H$, relative to the one for $M^+ \to \ell^+ \nu_\ell$, ν_ℓ a massless flavor neutrino, is given by :

$$\frac{\Gamma(M^+ \to \ell^+ \nu_H)}{\Gamma(M^+ \to \ell^+ \nu_\ell)} = |U_{H\ell}|^2 \cdot \bar{\rho}_{M,\ell}(m_{\nu_H}) \qquad \text{(A-1)}$$

, where ν_H could be any heavy neutrino and ν_ℓ is a conventional massless neutrino,

and $$\bar{\rho}_{M,\ell}(m_{\nu_H}) = \frac{\rho(X,Y)}{X(1-X)^2} \qquad \text{(A-2)}$$

$$\rho(X,Y) = h(X,Y) \cdot \lambda^{1/2}(1,X,Y) \qquad \text{(A-3)}$$

$$h(X,Y) = X + Y - (X - Y)^2 \qquad \text{(A-4)}$$

$$\lambda(1,X,Y) = 1 + X^2 + Y^2 - 2(X + Y + XY) \qquad \text{(A-5)}$$

where $X = m_\ell^2/m_M^2$ and $Y = m_{\nu_H}^2/m_M^2$. $h(X,Y)$ originates from the decay matrix element and $\lambda^{1/2}(1,X,Y)$ is a phase space factor.

In comparing $h(X,Y)$ and $\lambda^{1/2}(1,X,Y)$ with the massless case, $\bar{h}(X,Y)$ and $\bar{\lambda}^{1/2}(1,X,Y)$ are defined as the followings :

$$\bar{h}(X,Y) = \frac{h(X,Y)}{h(X,0)} = \frac{h(X,Y)}{X(1-X)} \qquad \text{(A-6)}$$

$$\bar{\lambda}^{1/2}(1,X,Y) = \frac{\lambda^{1/2}(1,X,Y)}{\lambda^{1/2}(1,X,0)} = \frac{\lambda^{1/2}(1,X,Y)}{1-X} \qquad \text{(A-7)}$$

and then

$$\bar{\rho}_{M,\ell}(m_{\nu_H}) = \frac{\rho(X,Y)}{\rho(X,0)} = \frac{h(X,Y)\cdot\lambda^{1/2}(1,X,Y)}{x(1-X)^2}$$

$$= \bar{h}(X,Y)\cdot\bar{\lambda}^{1/2}(1,X,Y). \qquad \text{(A-8)}$$

When $Y = 0$, i.e., in the case of massless neutrinos, $\bar{\rho} = 1$. $\bar{\rho}$ vanishes for $m_{\nu_H} \geqq m_M - m_\ell$.

APPENDIX B. Error of The Ratio R = X/Y

X and Y are independent normal variables whose means are μ_x and μ_y, and variances are σ_x and σ_y, respectively. The ratio R = X/Y does not behave as a normal distribution. However, $(\mu_x - \mu_y R)/(\sigma_x^2 + \sigma_y^2 R)^{-1/2}$ is normally distributed about zero with an unit variance assuming that μ_y is so large compared with σ_y that the range of Y is effectively positive.

Therefore the error of R within S times of a standard deviation is :

$$\frac{\mu_x\mu_y \pm \sqrt{\mu_x^2\mu_y^2 - (\mu_x^2 - S^2\sigma_x^2)(\mu_y^2 - S^2\sigma_y^2)}}{\mu_y^2 - S^2\sigma_y^2} \qquad \text{(B-1)}$$

When $\sigma_y = 0$, this form reduces to a well known form such as :

$$R \pm S\delta R \qquad \text{(B-2)}$$

$$\delta R = R\sigma_x/\mu_x \qquad \text{(B-3)}$$

An upper limit at 90% C.L. is given by taking S = 1.282 and an upper sign (+) in the equation (B-1).

REFERENCES

[1.1] W.Pauli, Septieme Conseil Solvay, 1933(Gauthier-Villars, Paris, 1934).

[1.2] C.L.Cowan Jr. and F.Reines et al.,Science 124(1956)103.

[1.3] M.Goldhaber et al., Phys.Rev.109(1958)1015.

[1.4] G.Backenstoss et al., Phys.Rev.Lett.8(1961)415.

[1.5] G.Danby et al., Phys.Rev.Lett.9(1962)36.

[1.6] S.L.Glashow, Nucl.Phys.22(1961)579;
S.Weinberg, Phys.Rev.Lett.19(1967)1264;
A.Salam, Proc. 8Th Nobel Symp., ed. N.Svarthlm (Almquist and Wiksell, Stockholm,1968)367.

[1.7] F.J.Hasert et al., Phys.Lett.46B(1973)121;
F.J.Hasert et al., Phys.Lett.46B(1973)138.

[1.8] UA1 G.Arnison et al.,Phys.Lett.122B(1983)103 (W);
UA1 G.Arnison et al.,Phys.Lett.129B(1983)273 (W);
UA1 G.Arnison et al.,Phys.Lett.134B(1984)469 (W);
UA1 G.Arnison et al.,Phys.Lett.126B(1983)398 (Z);
UA2 B.Banner et al.,Phys.Lett.122B(1983)476 (W);
UA2 B.Banner et al.,Phys.Lett.129B(1983)130 (Z).

[1.9] H.Georgi and S.L.Glashow, Phys.Rev.Lett.32(1974)438;
C.Pati and A.Salam, Phys.Rev.Lett.31(1973)661.

[1.10] C.Pati and A.Salam, Phys.Rev.D10(1974)275;
R.N.Mohapatra et al., Phys.Rev.D11(1975)566.

[1.11] R.Davis et al., Proc. of the Conf. on the Intersection between Particle and Nulear Phys., Steamboat Spring, 1984;
K.S.Hirata et al., Phys.Rev.Lett.63(1989)16,
ICR Report,95-89-12.

[1.12] For a review, see for example, "THE PHYSICS OF MASSIVE NEUTRINOS", World Scientific, 1989.

[1.13] Review of Particle Properties, Particle Data Group.

[1.14] V.A.Lubimov, Proc. of Brighton Int. Conf.,1983.

[1.15] M.Fritschi et al., Phys.Lett.173B(1986)485;
J.F.Wilkerson et al., Phys.Rev.Lett.58(1987)2023;
H.Kawakami et al., Proc. 6th Moriond Workshop '86, Massive Neutrinos in Astrophysics and in Particle Physics, Tignes, Jan.25-Feb.1, 1986, ed. O Fackler and J.Tran Thank Van.

[1.16] T.Tomoda et al., Nucl.Phys.A452(1986)591.

[1.17] L.A.Ahrens et al., Phys.Rev.D31(1985)2732.

[1.18] G.Zacek et al., Phys.Rev.D34(1986)2621;
E531-Coll., N.Ushida et al., Phys.Rev.Lett.57(1986) 2897;
F.Dydak et al., Phys.Lett.134B(1984)34.

[1.19] R.E.Shrock, Phys.Lett.96B(1980)159;
R.E.Shrock, Phys.Rev.D24(1981)1232;
M.Gronau, Phys.Rev.D28(1983)2762.

[1.20] Y.Asano et al., Phys.Lett.B104(1981)84.

[1.21] R.S.Hayano et al., Phys.Rev.Lett.49(1982)1305;
T.Yamazaki, Proc. 22nd Intern. Conf. on HEP (Leipzig) p.262.

[1.22] R.Abela et al., Phys.Lett.105B(1981)263;
R.Minehart et al., Phys.Rev.Lett.52(1984)804.

[1.23] D.A.Bryman et al., Phys.Rev.Lett.50(1982)1546.

[1.24] CHARM-Coll.,J.Dorenbosch et al., Phys.Lett.166B(1986) 473.

[1.25] WA66-Coll., A.Cooper-Sarkar, Phys.Lett.160B(1985)207.

[1.26] H.Faissner et al., Z.Phys.C10(1981)95.

[2.1] L.A.Ahrens et al., Phys.Rev.Lett.51(1983)1514;
L.A.Ahrens et al., Phys.Rev.Lett.54(1985)18.

[3.1] D.Rein and L.M.Sehgal, Ann. of Phys.133(1981)79.

[3.2] G.Knopp et al., Nucl.Phys.B123(1977)61.

[4.1] L.A.Ahrens et al., Phys.Rev.D34(1986)75.

[4.2] N.J.Baker et al., Phys.Rev.D25(1982)617.

[4.3] G.Bernardi et al., Phys.Lett.B166(1986)497.

[4.4] F.Bergsma et al., Phys.Lett.B128(1983)361.

[4.5] D.Toussaint and F.Wilczek, Nature 289(1981)777;

[4.6] C.N.Pang et al., Phys.Rev.D8(1973)1989.

[4.7] K.Herard et al., Phys.Lett.B55(1975)327.
J.Heintze et al., Phys.Lett.B60(1976)302.

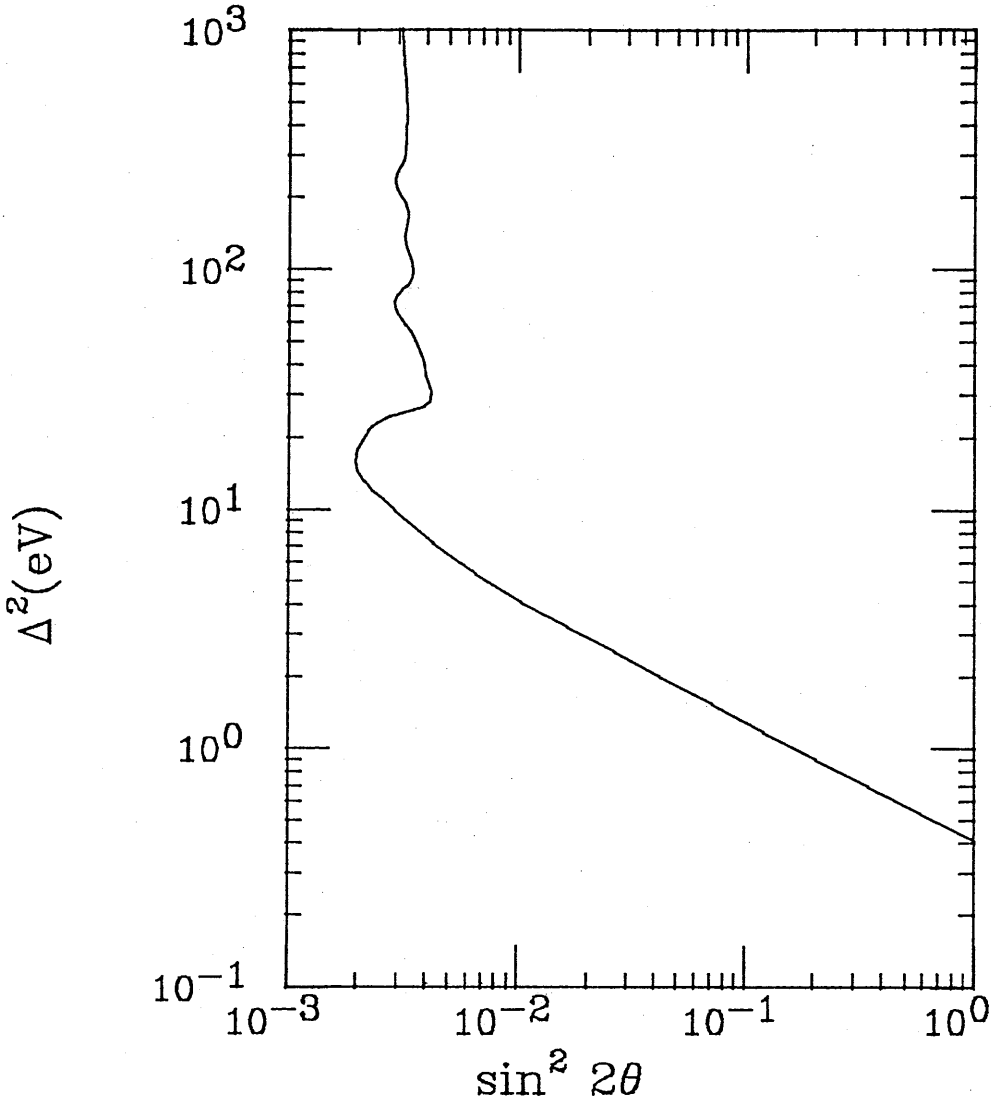

Figure 1.1

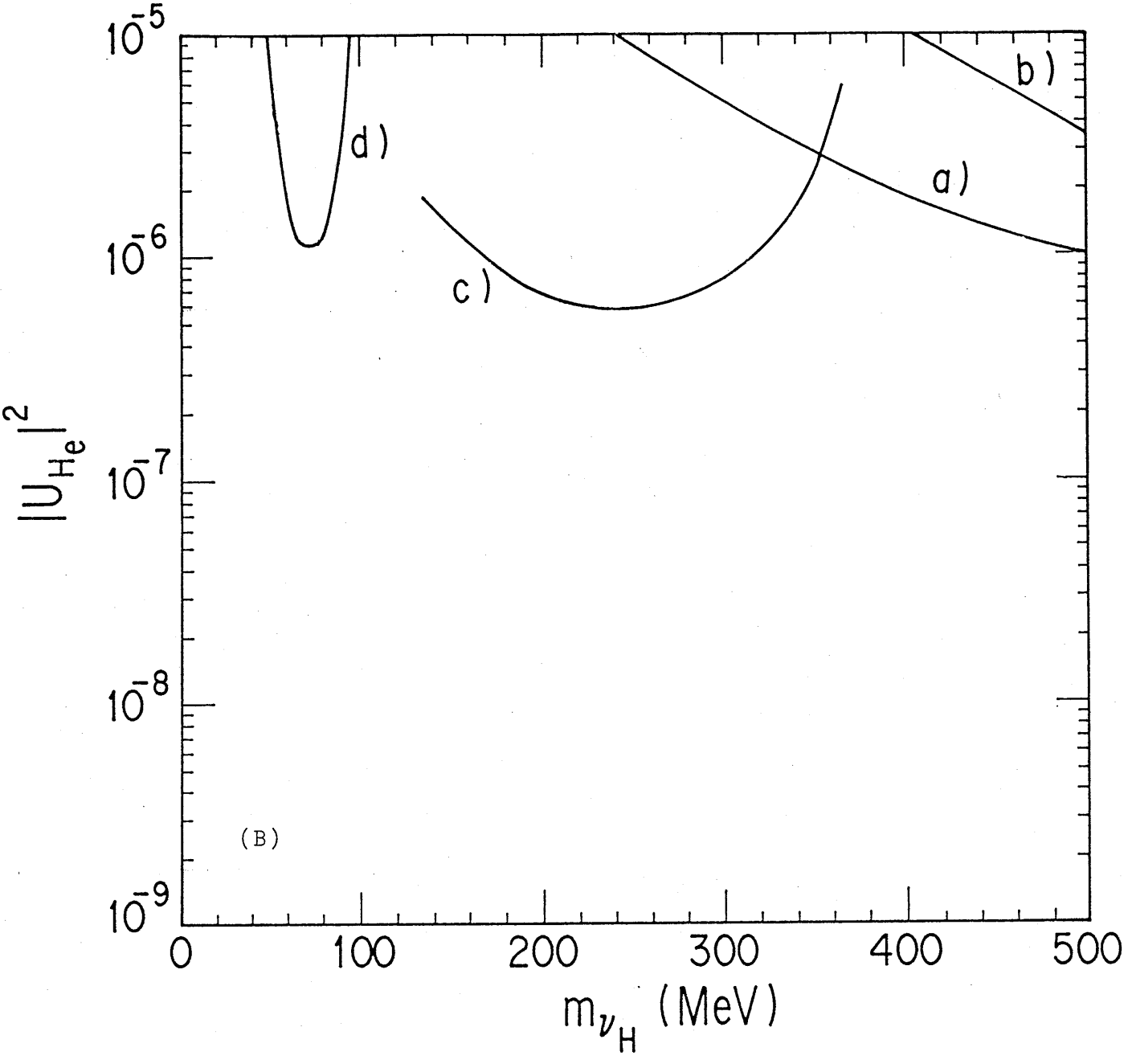

Figure 1.2

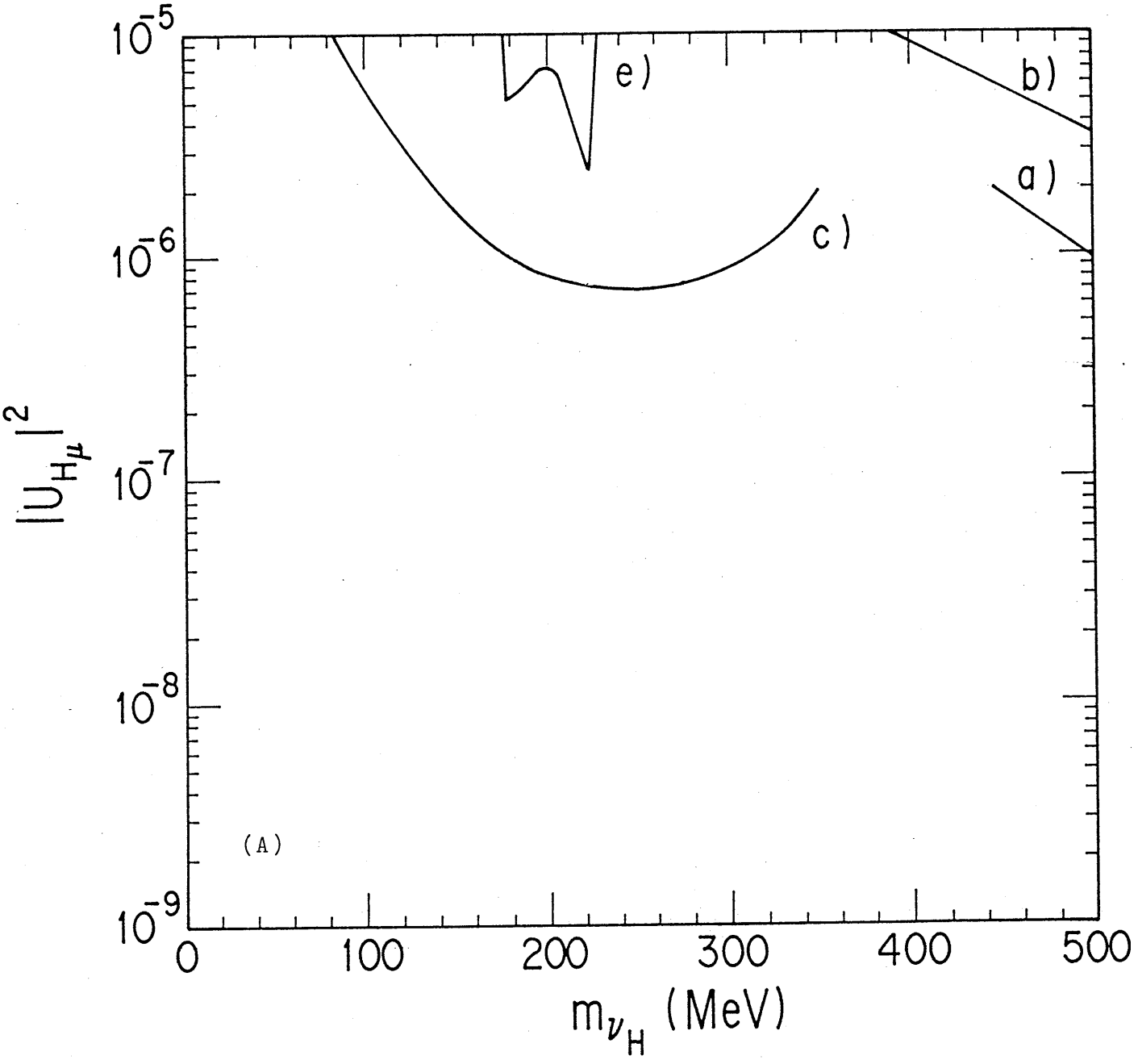

Figure 1.2

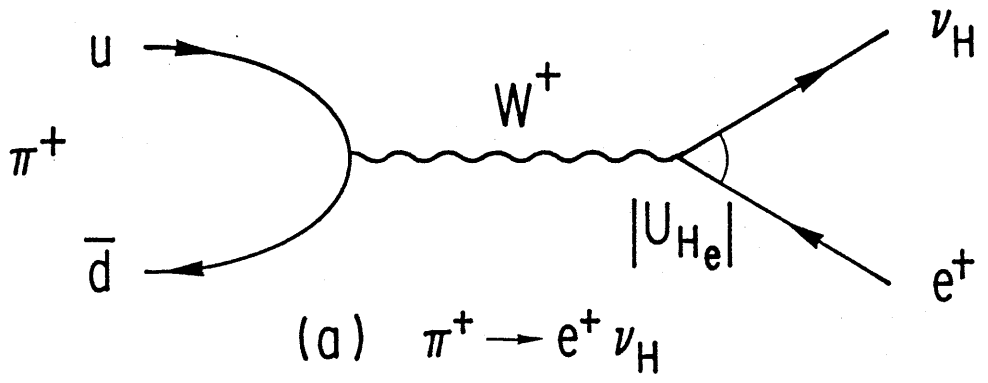

(a) $\pi^+ \rightarrow e^+ \nu_H$

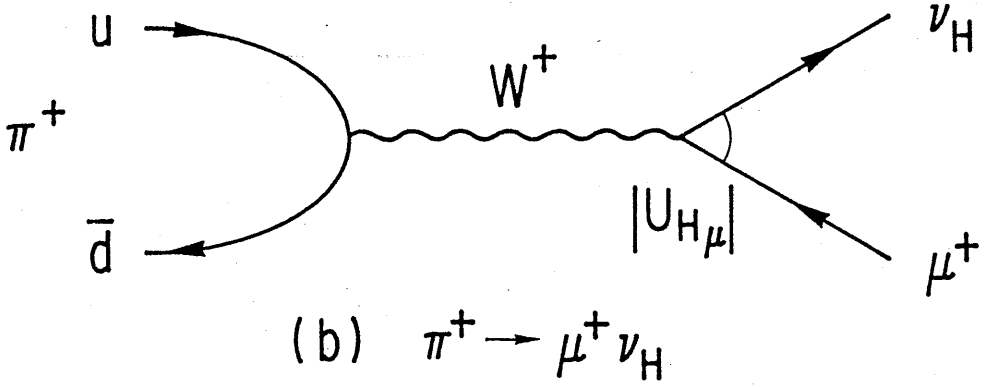

(b) $\pi^+ \rightarrow \mu^+ \nu_H$

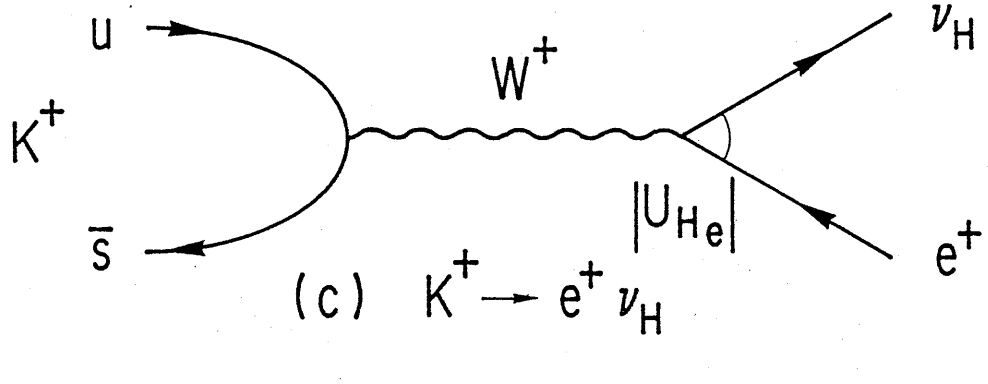

(c) $K^+ \rightarrow e^+ \nu_H$

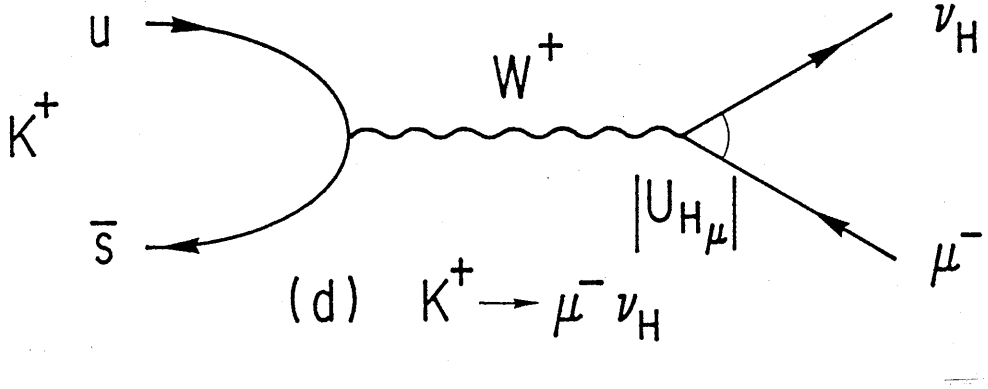

(d) $K^+ \rightarrow \mu^- \nu_H$

Figure 1.3

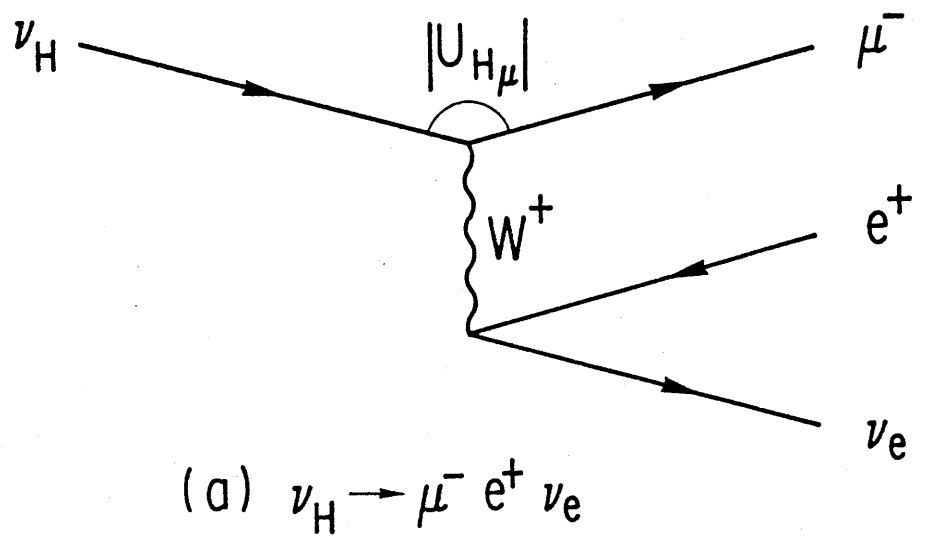

(a) $\nu_H \rightarrow \mu^- e^+ \nu_e$

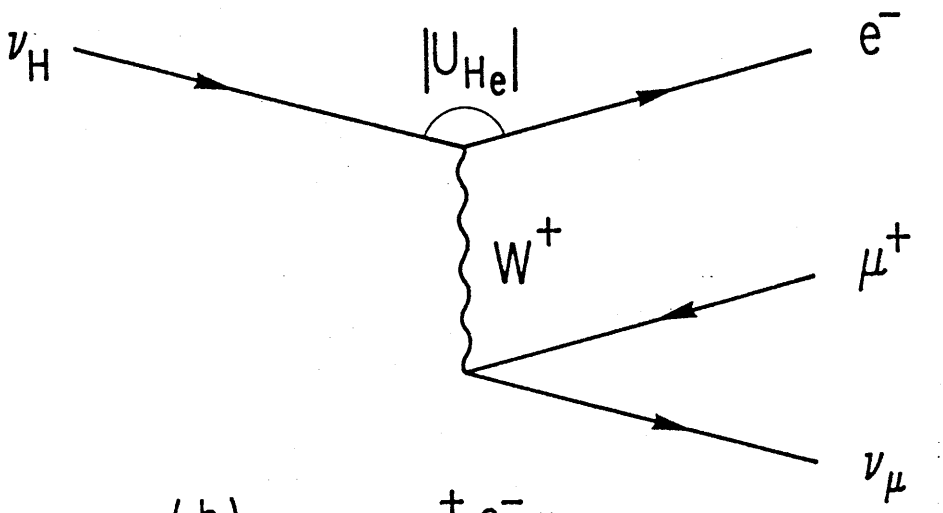

(b) $\nu_H \rightarrow \mu^+ e^- \nu_\mu$

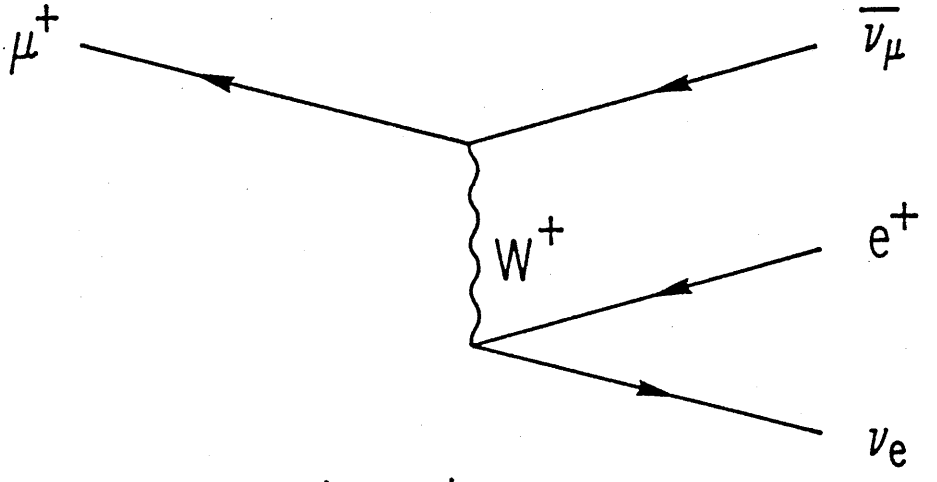

(c) $\mu^+ \rightarrow e^+ \nu_e \overline{\nu_\mu}$

Figure 1.4

The AGS at Brookhaven National Laboratory

Figure 2.1

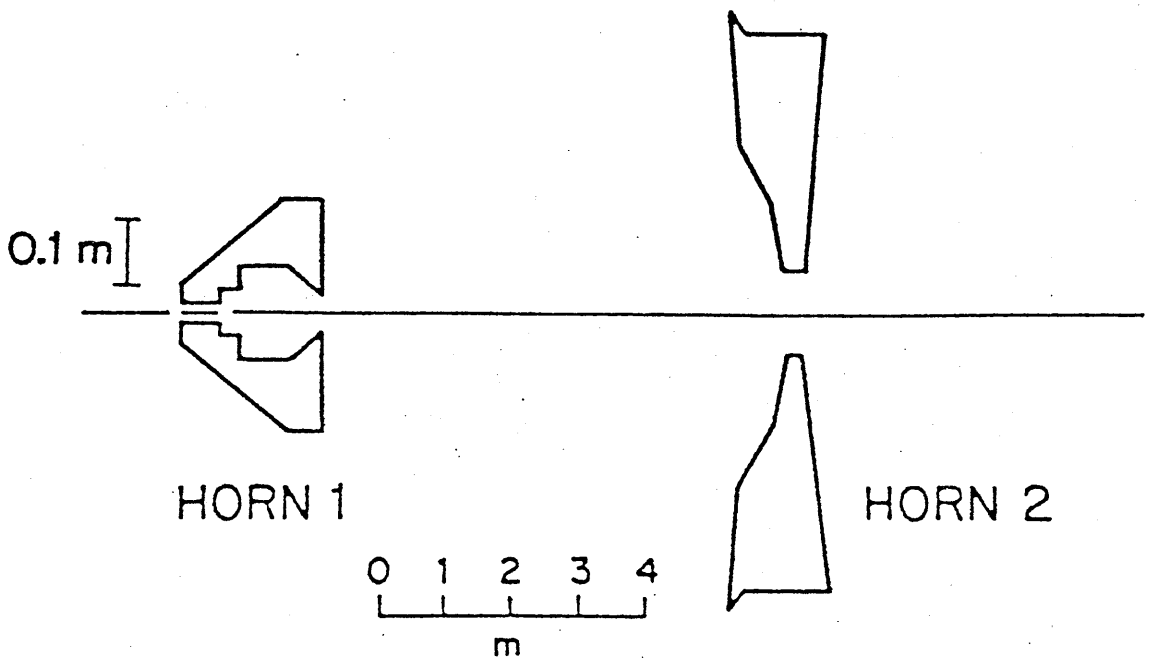

Figure 2.2

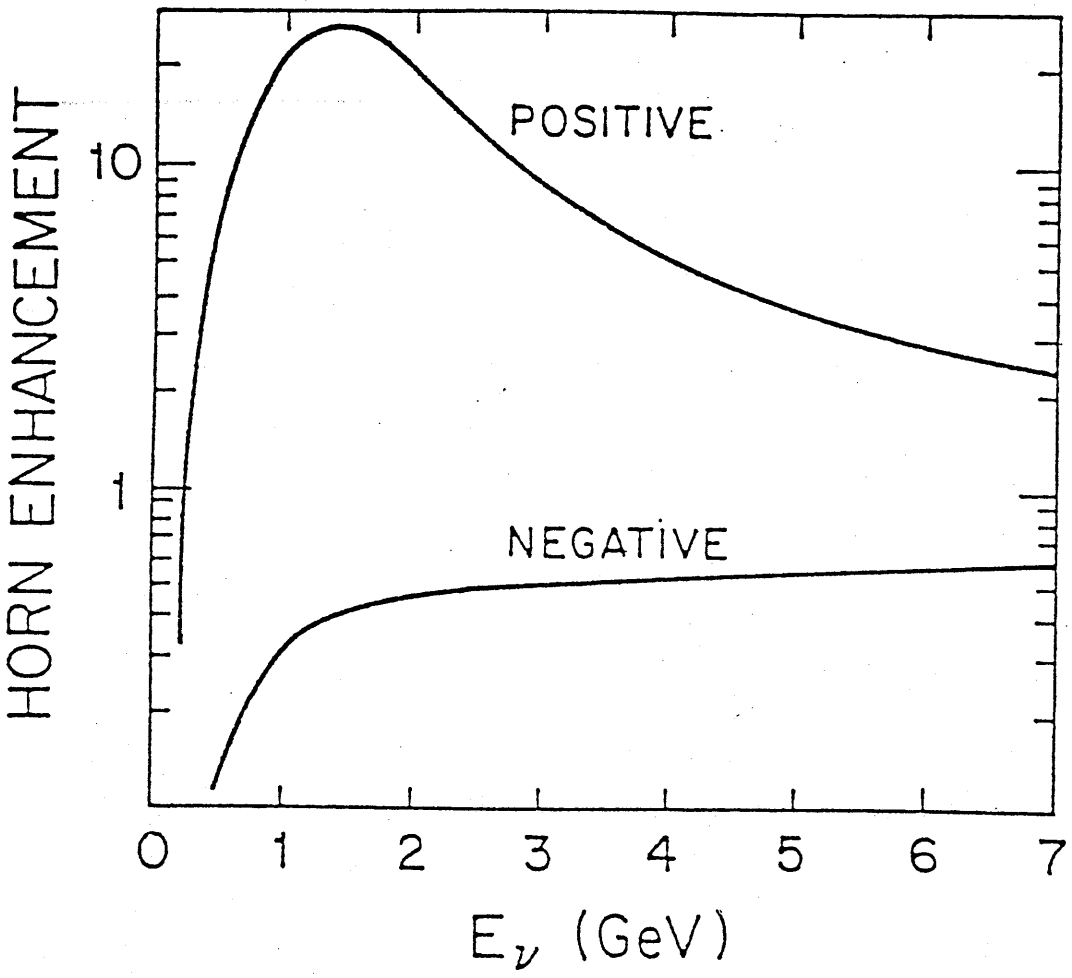

Figure 2.3

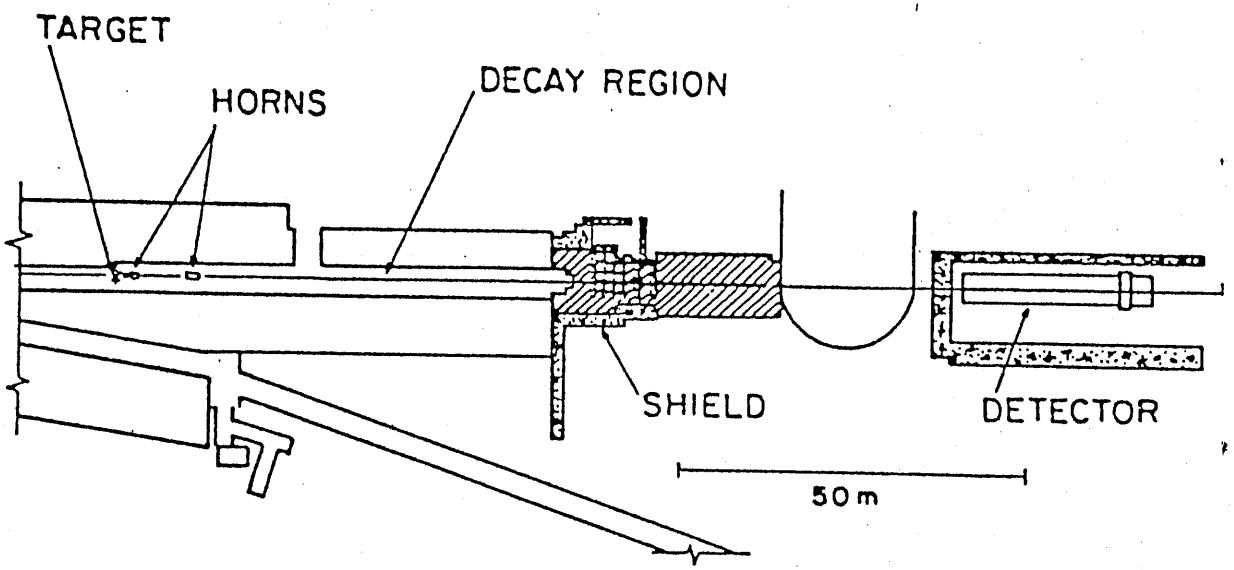

Figure 2.4

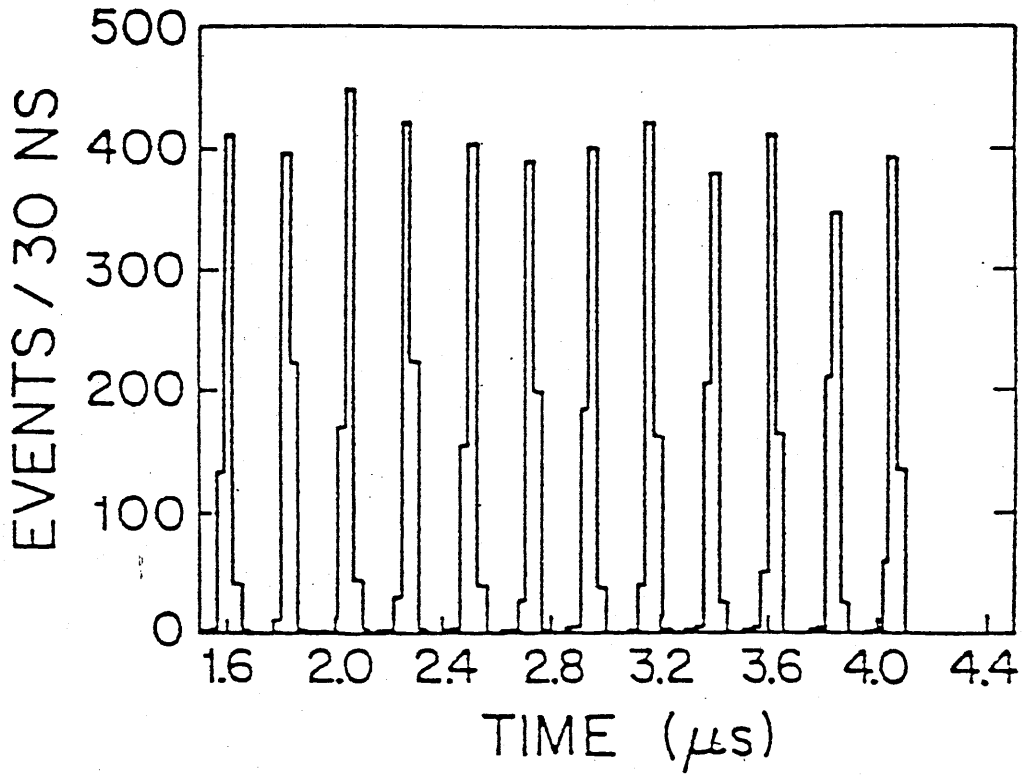

Figure 2.5

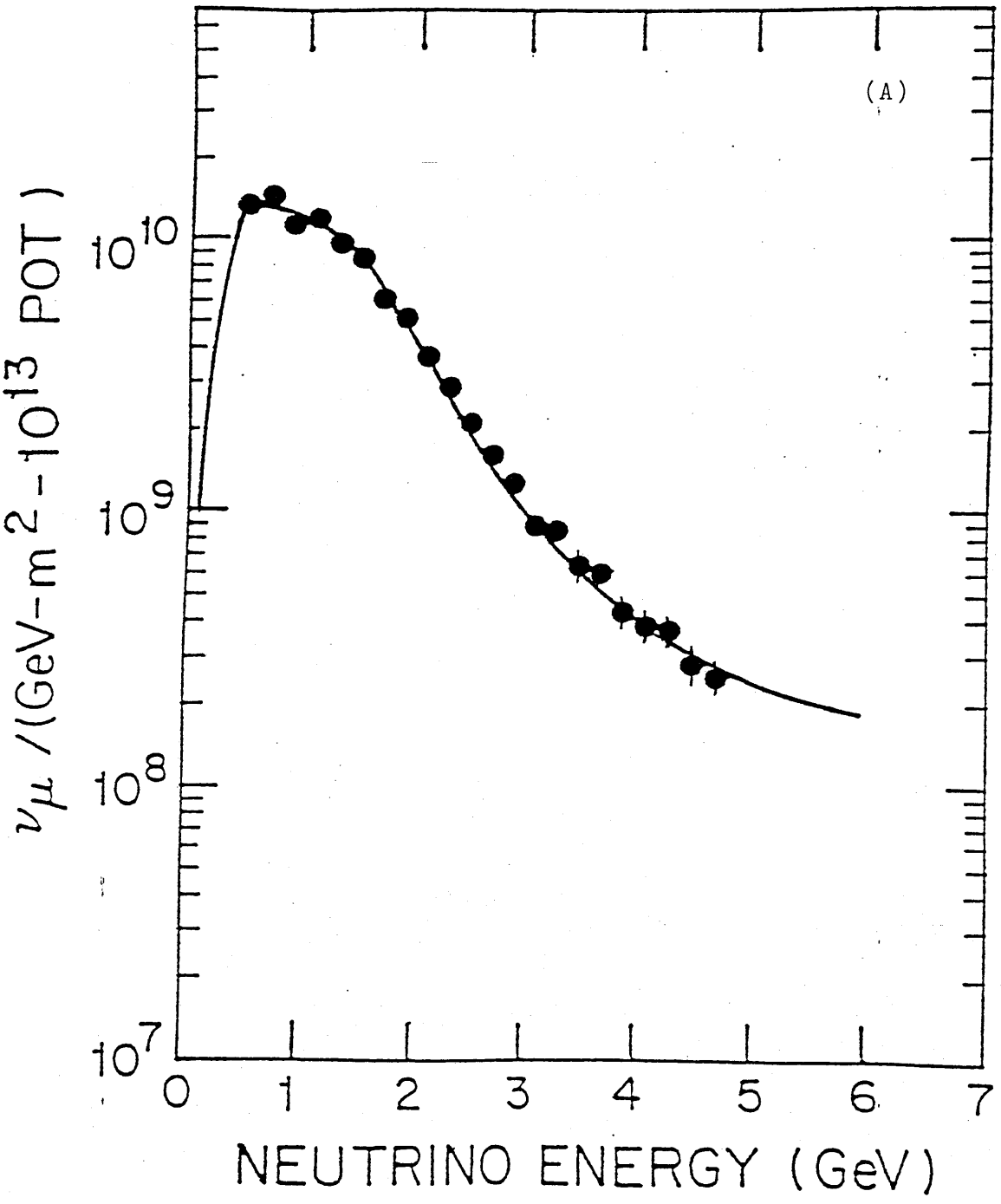
(A)
ν_μ /(GeV-m^2-10^{13} POT)
10^{10}
10^9
10^8
10^7
0
1
2
3
4
5
6
7
NEUTRINO ENERGY (GeV)

Figure 2.6

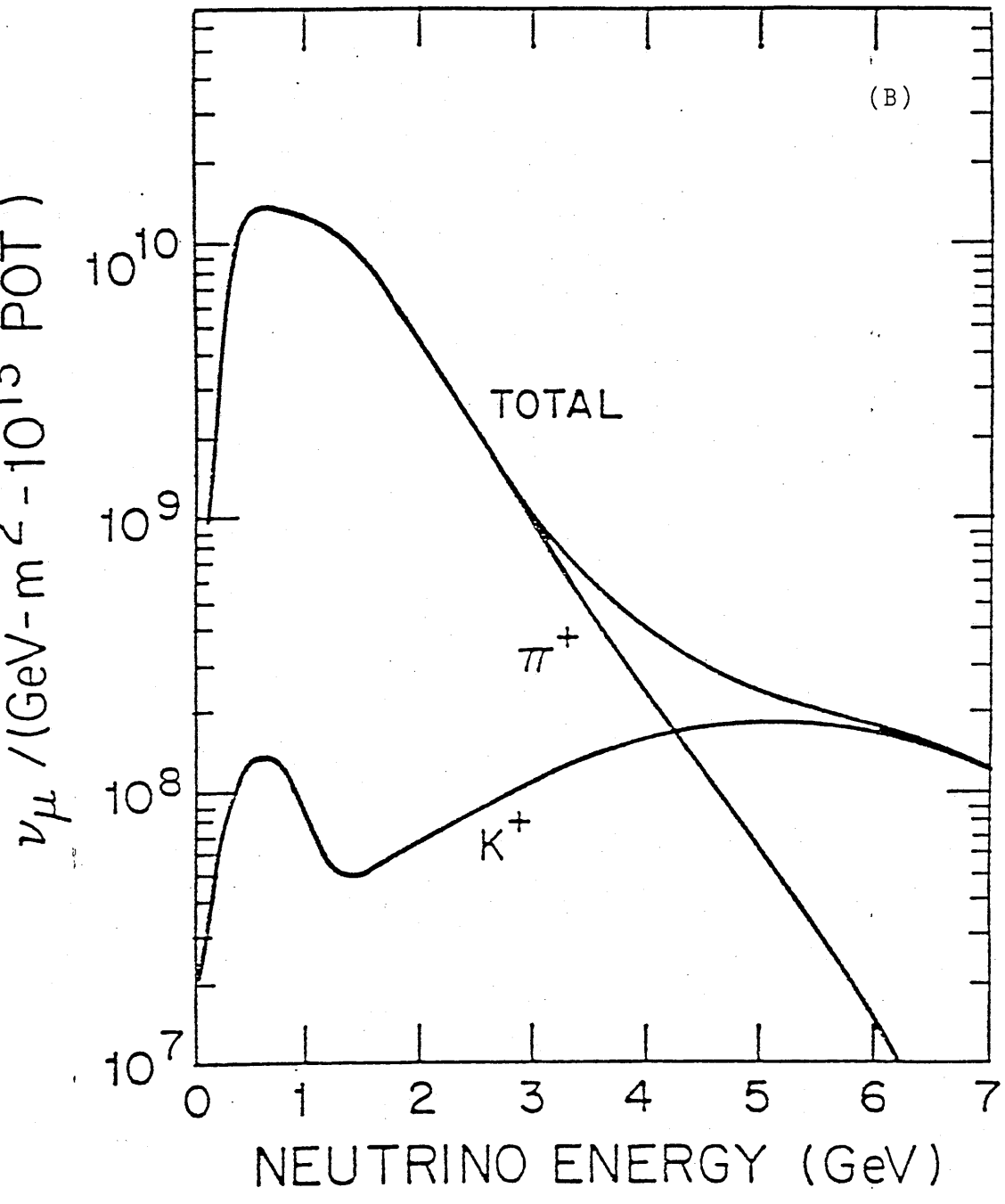
(B)
ν_μ /(GeV-m^2-10^{13} POT)
10^{10}
10^9
10^8
10^7
TOTAL
π^+
K^+
0
1
2
3
4
5
6
7
NEUTRINO ENERGY (GeV)

Figure 2.6

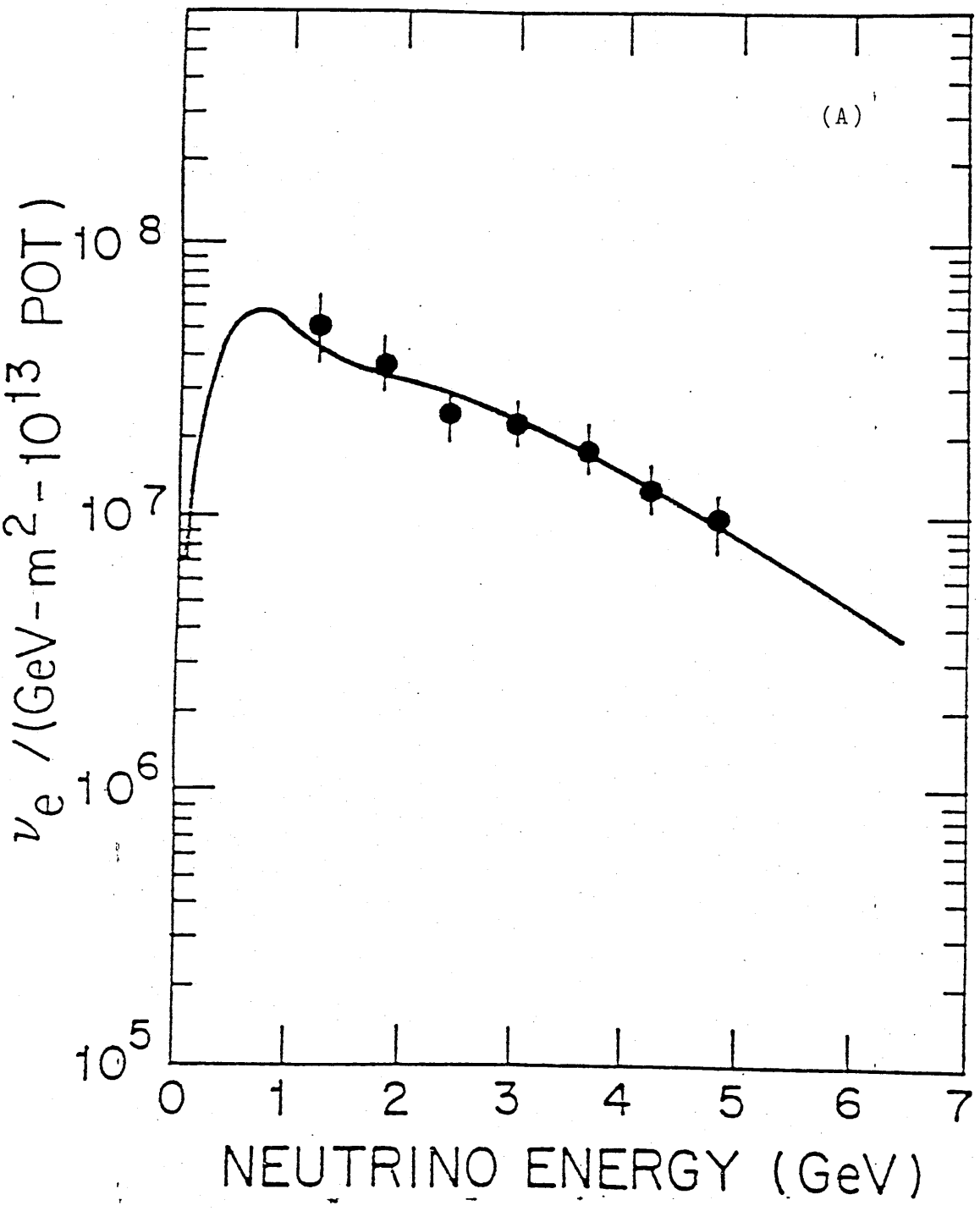
(A)
ν_e /(GeV-m^2-10^{13} POT)
10^8
10^7
10^6
10^5
0
1
2
3
4
5
6
7
NEUTRINO ENERGY (GeV)

Figure 2.7

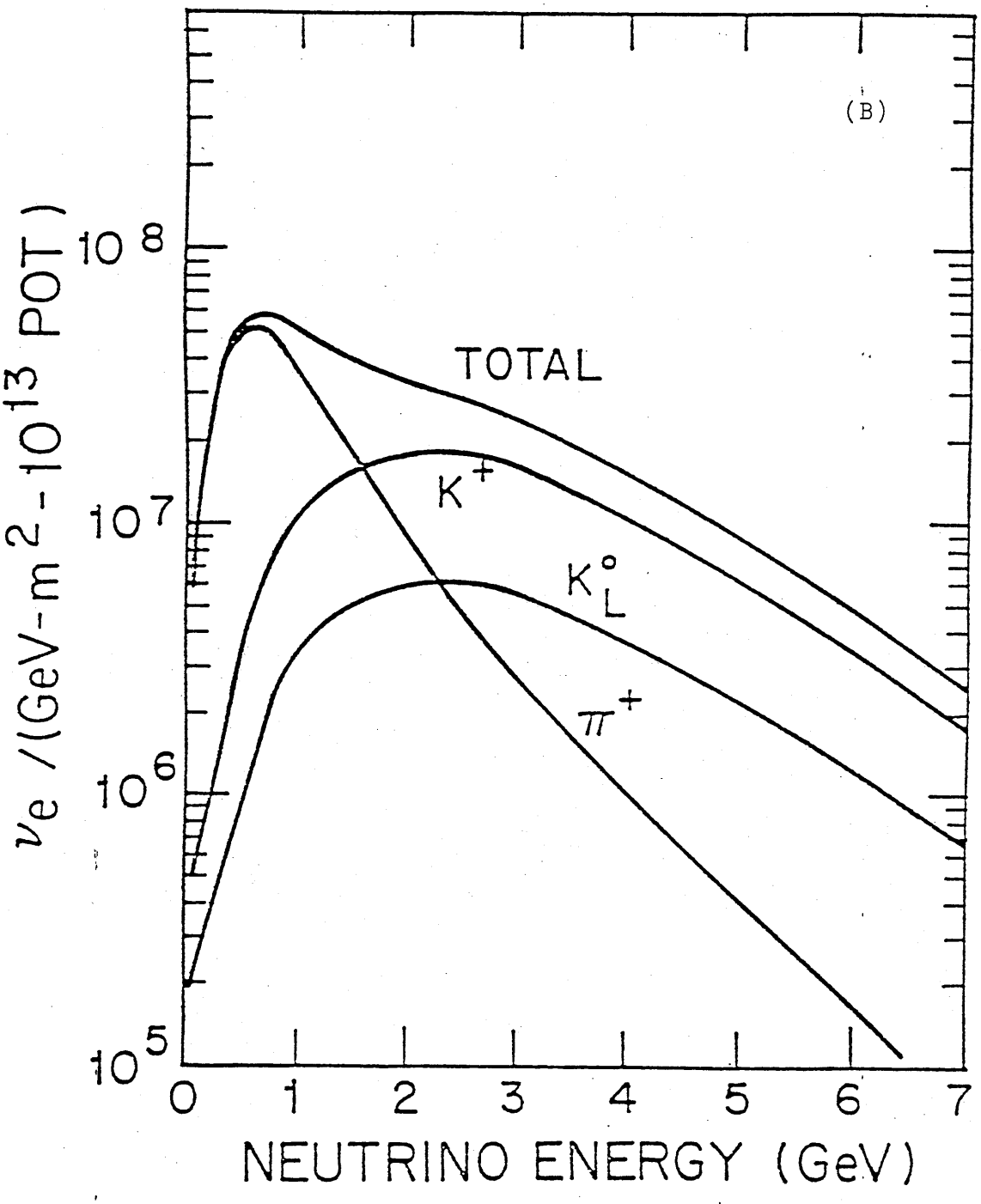
(B)
ν_e /(GeV-m^2-10^{13} POT)
10^8
10^7
10^6
10^5
TOTAL
K^+
K°_L
π^+
0
1
2
3
4
5
6
7
NEUTRINO ENERGY (GeV)

Figure 2.7

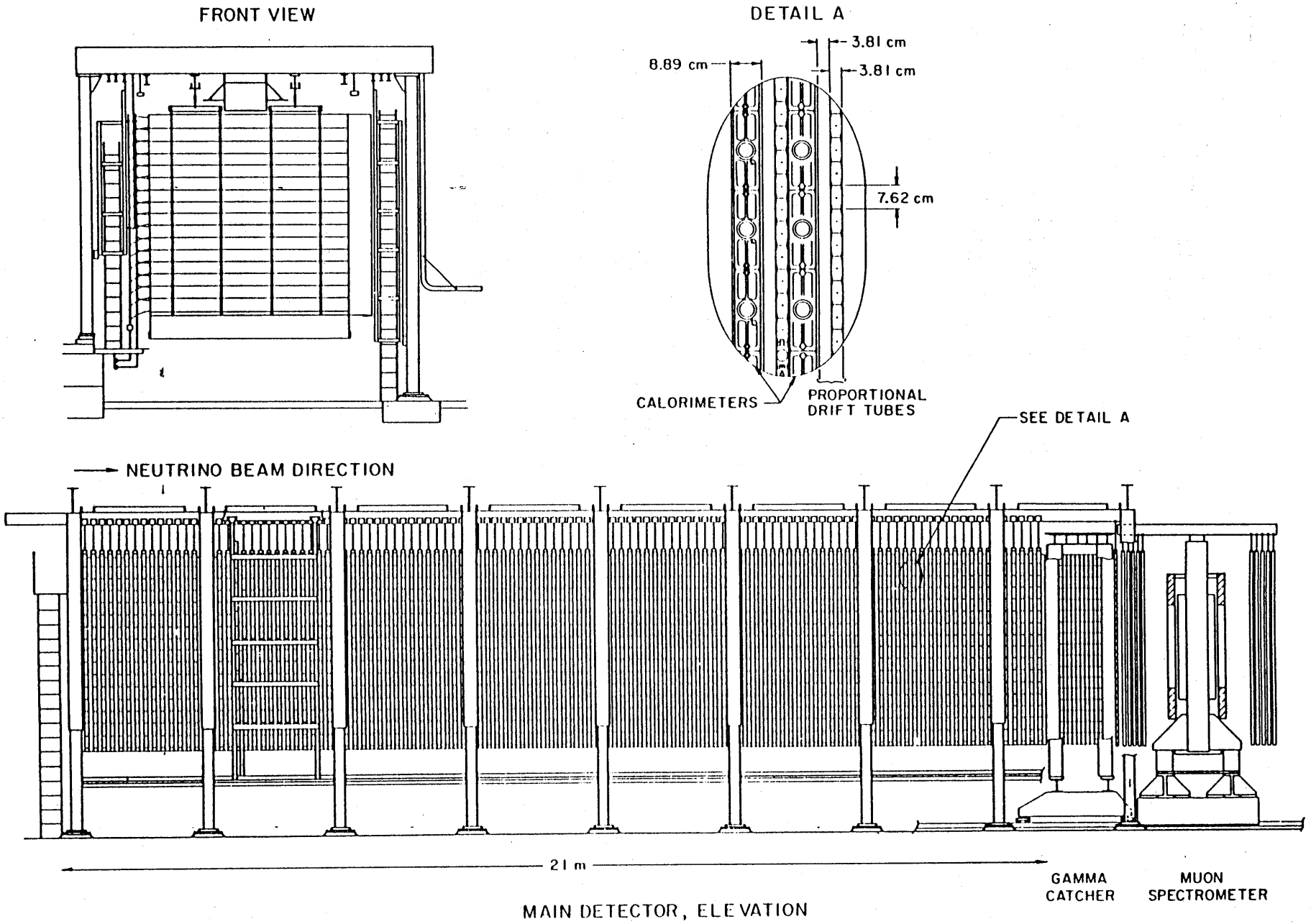
FRONT VIEW
DETAIL A
3.81 cm
3.81 cm
8.89 cm
7.62 cm
CALORIMETERS
PROPORTIONAL
DRIFT TUBES
SEE DETAIL A
NEUTRINO BEAM DIRECTION
21 m
GAMMA
CATCHER
MUON
SPECTROMETER
MAIN DETECTOR, ELEVATION

Figure 2.8

FRONT VIEW

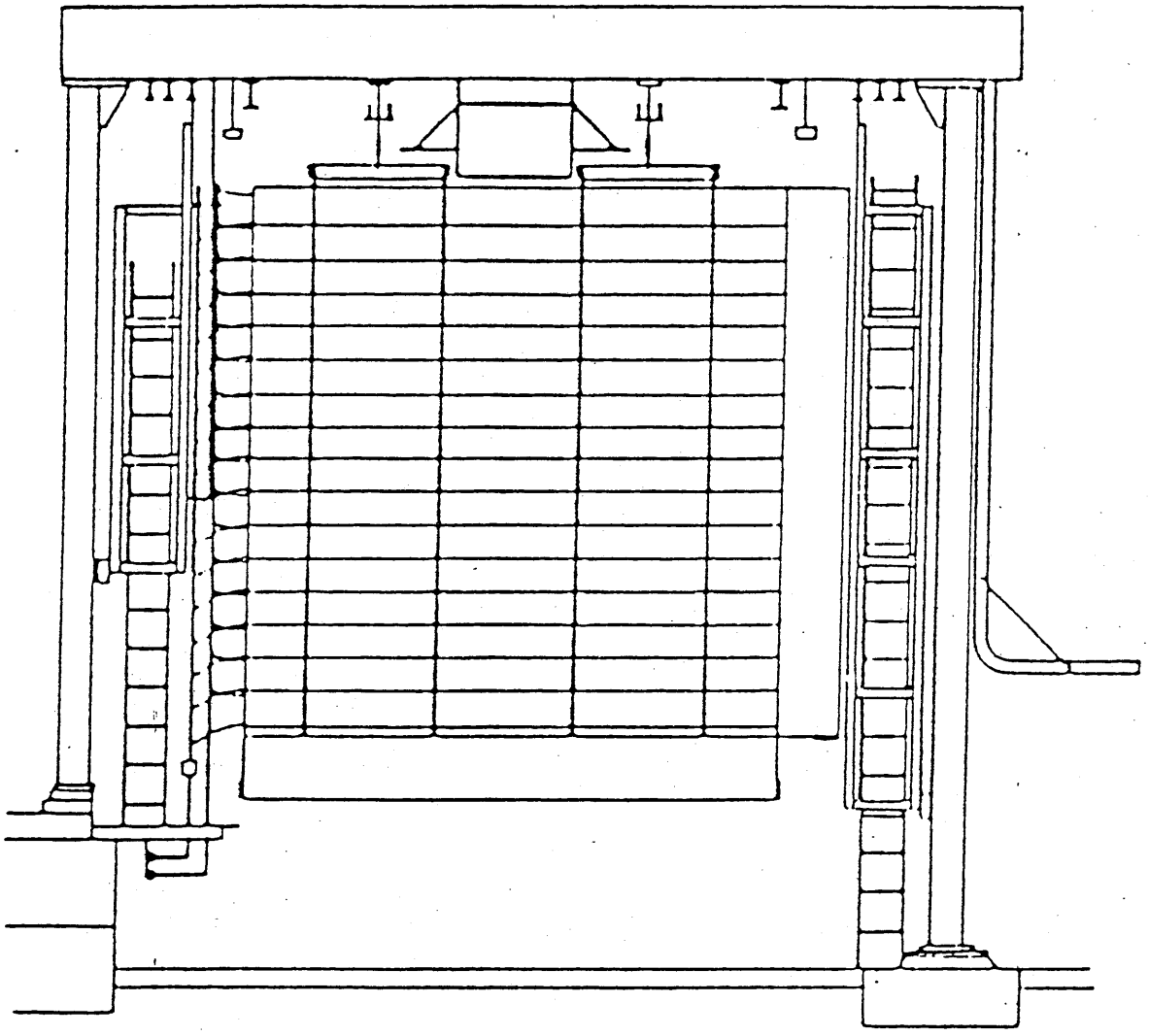

Figure 2.9

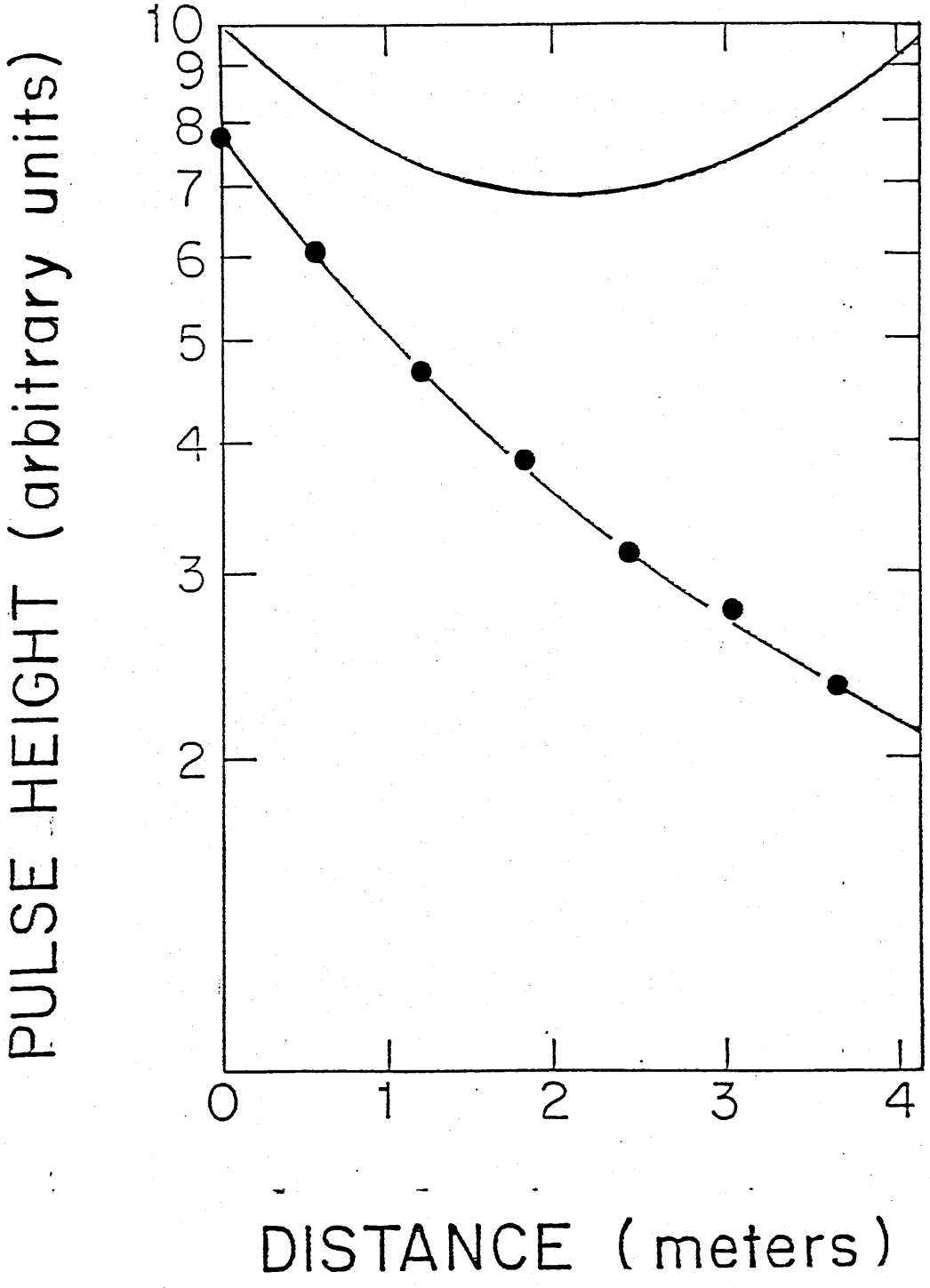
PULSE HEIGHT (arbitrary units)
10
9
8
7
6
5
4
3
2
0
1
2
3
4
DISTANCE (meters)

Figure 2.10

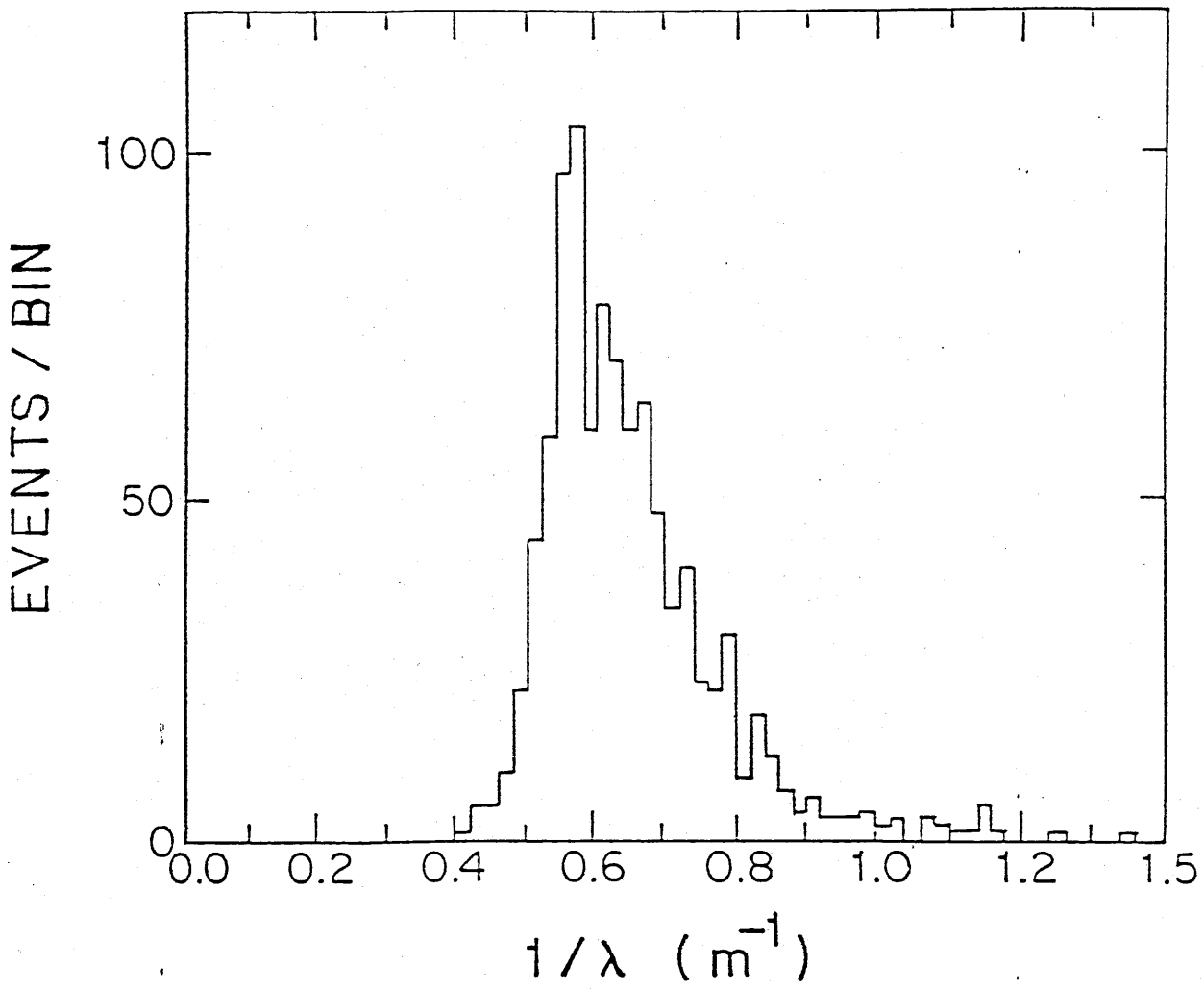

Figure 2.11

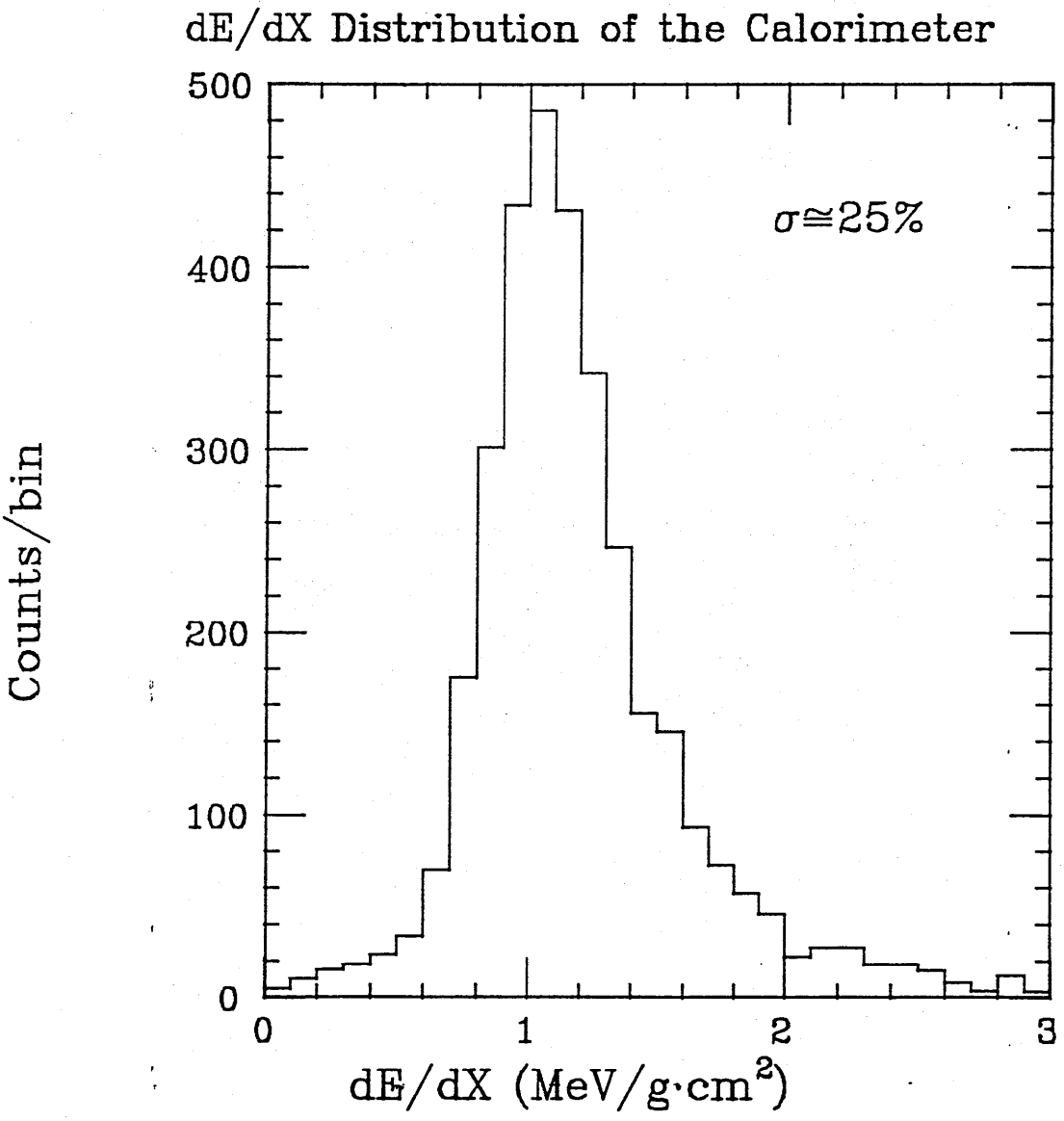
dE/dX Distribution of the Calorimeter
σ≅25%
Counts/bin
500
400
300
200
100
0
0
1
2
3
dE/dX (MeV/g·cm²)

Figure 2.12

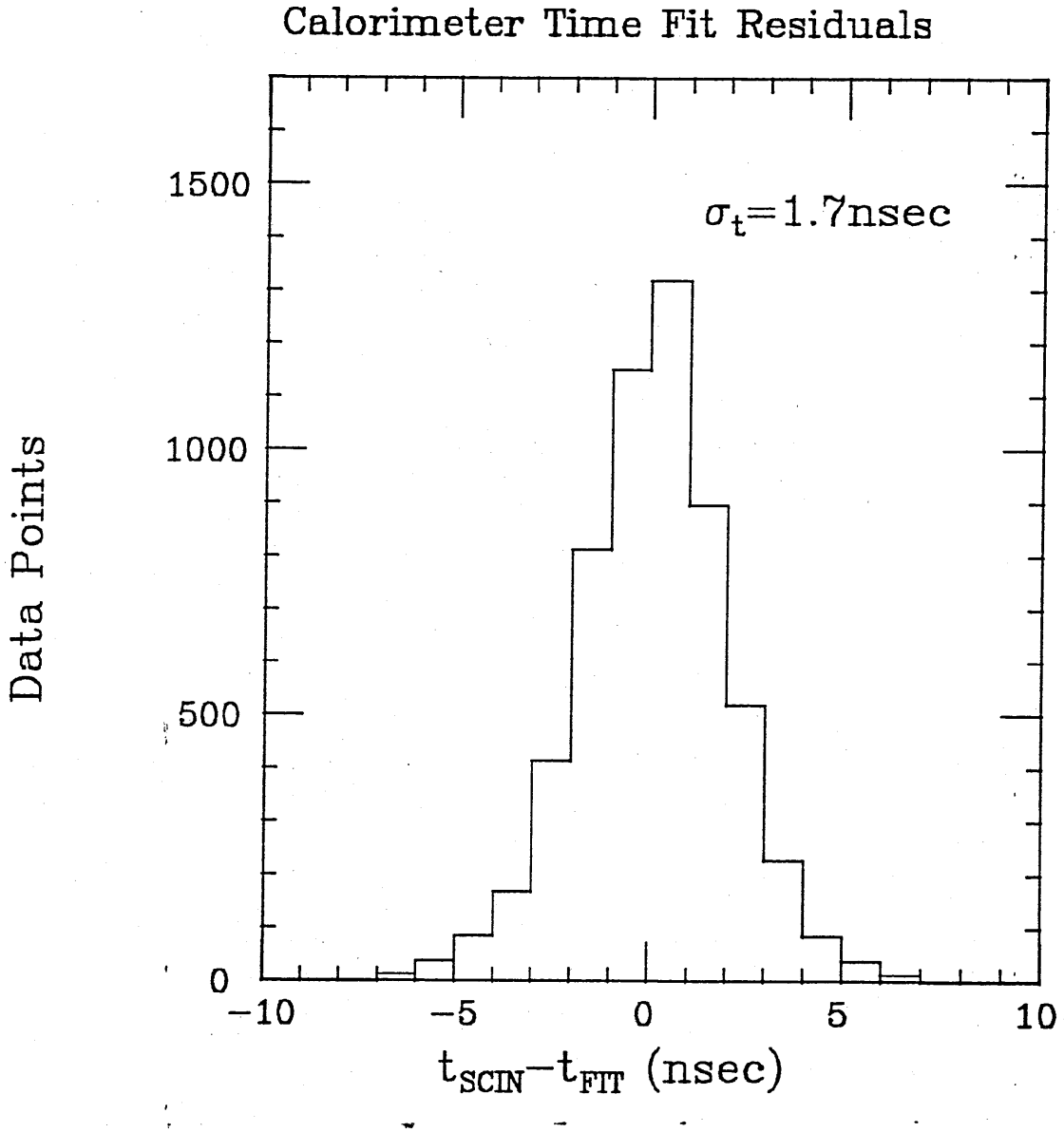
Calorimeter Time Fit Residuals
σ_t=1.7nsec
Data Points
1500
1000
500
0
−10
−5
0
5
10
$t_{SCIN}-t_{FIT}$ (nsec)

Figure 2.13

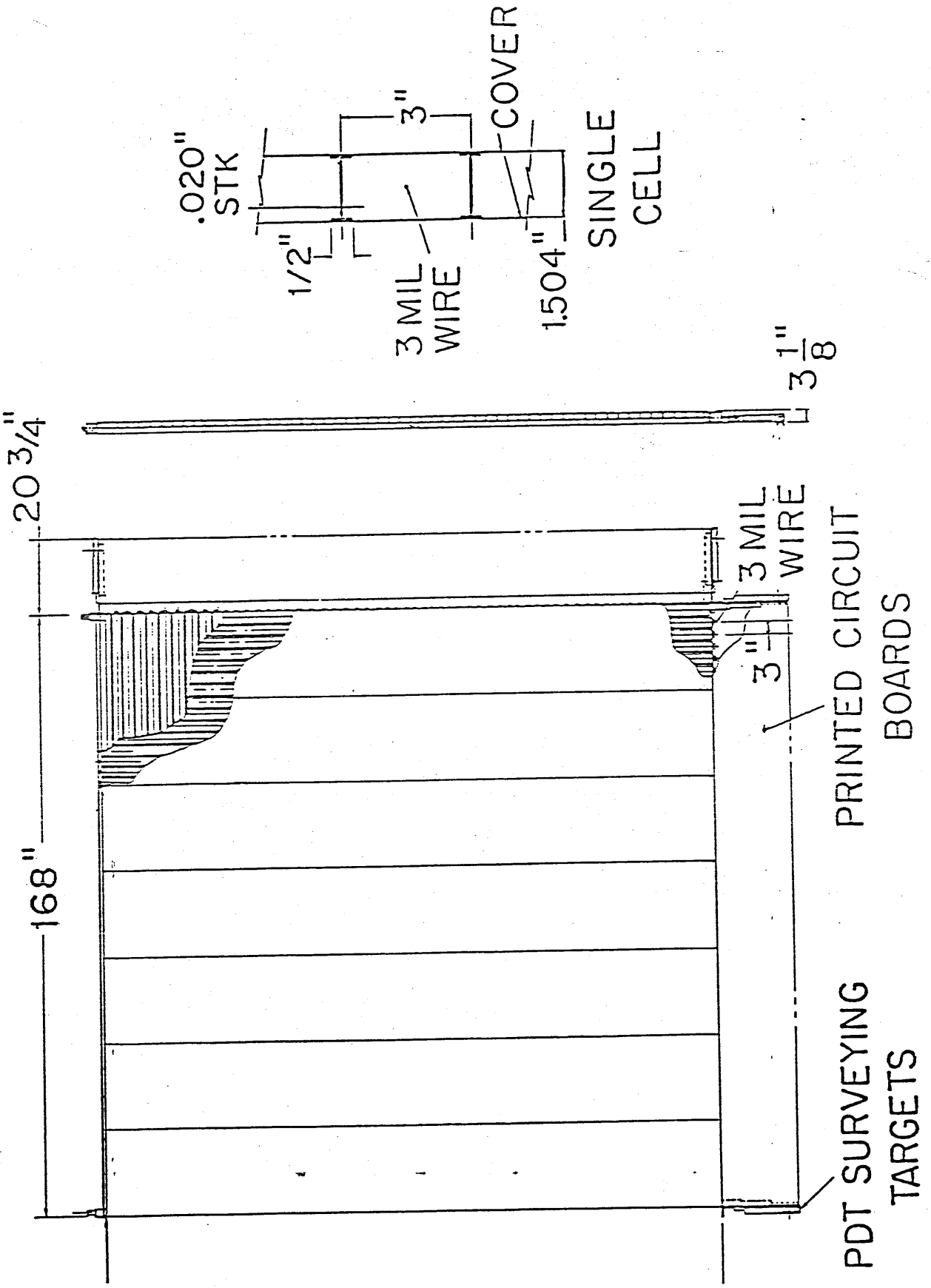
.020"
STK
3"
COVER
SINGLE
CELL
1/2"
3 MIL
WIRE
1.504"
3 1/8"
20 3/4"
3 MIL
WIRE
3"
PRINTED CIRCUIT
BOARDS
168"
PDT SURVEYING
TARGETS

Figure 2.14

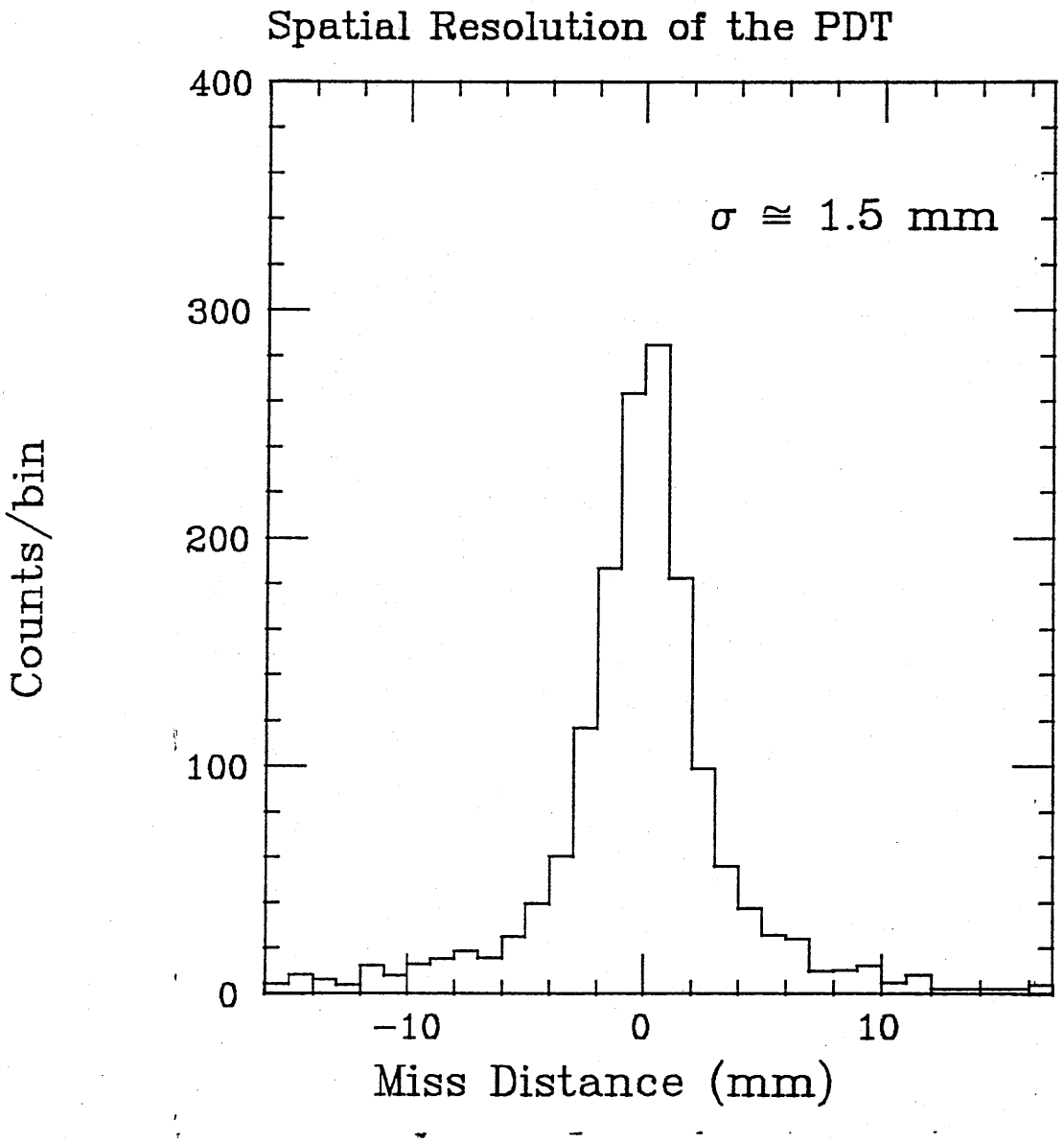
Spatial Resolution of the PDT
σ ≅ 1.5 mm
Counts/bin
400
300
200
100
0
−10
0
10
Miss Distance (mm)

Figure 2.15

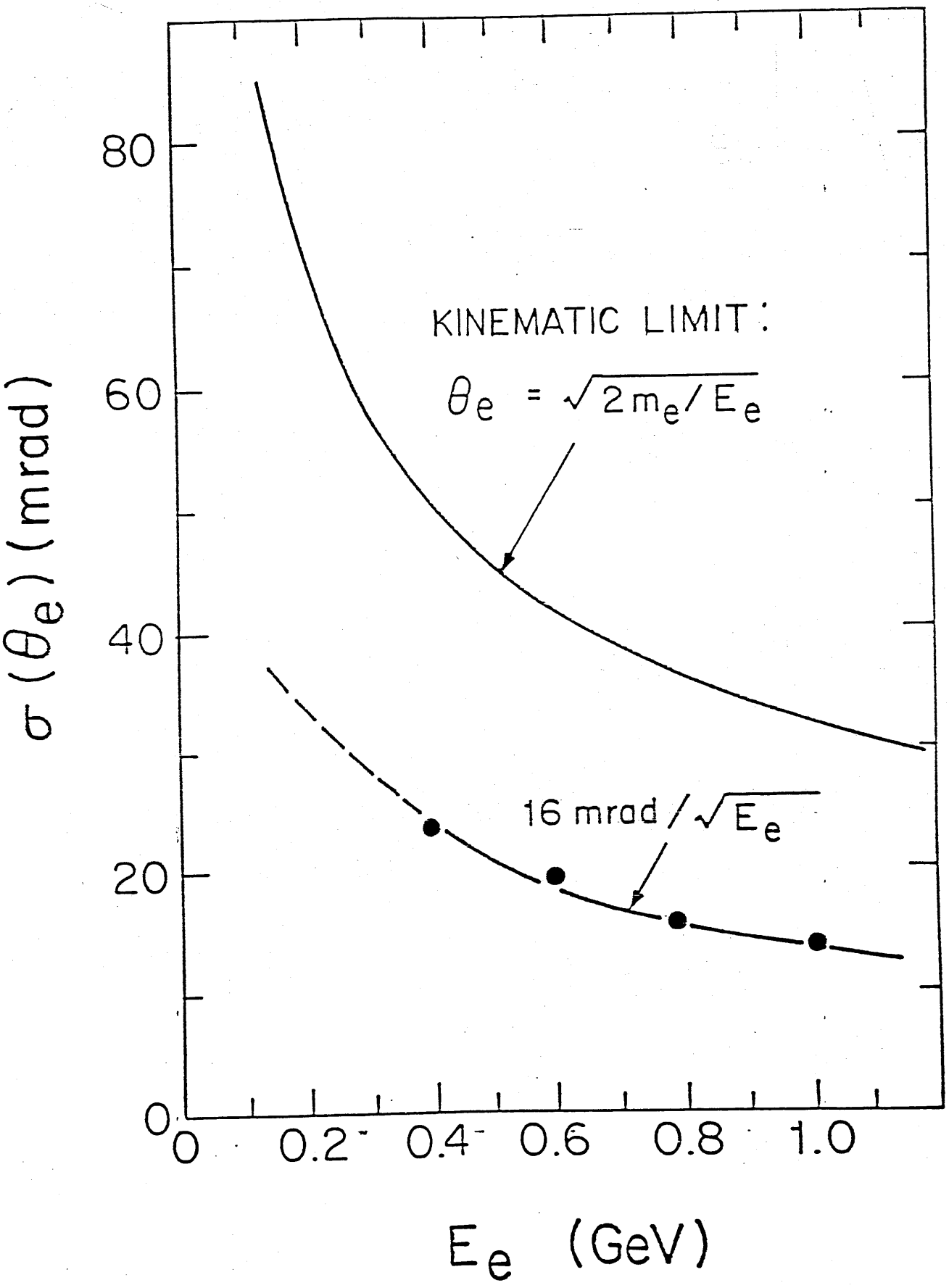
80
60
40
20
0
0
0.2
0.4
0.6
0.8
1.0
σ (θe) (mrad)
Ee (GeV)
KINEMATIC LIMIT:
θe = √2me/Ee
16 mrad / √Ee

Figure 2.16

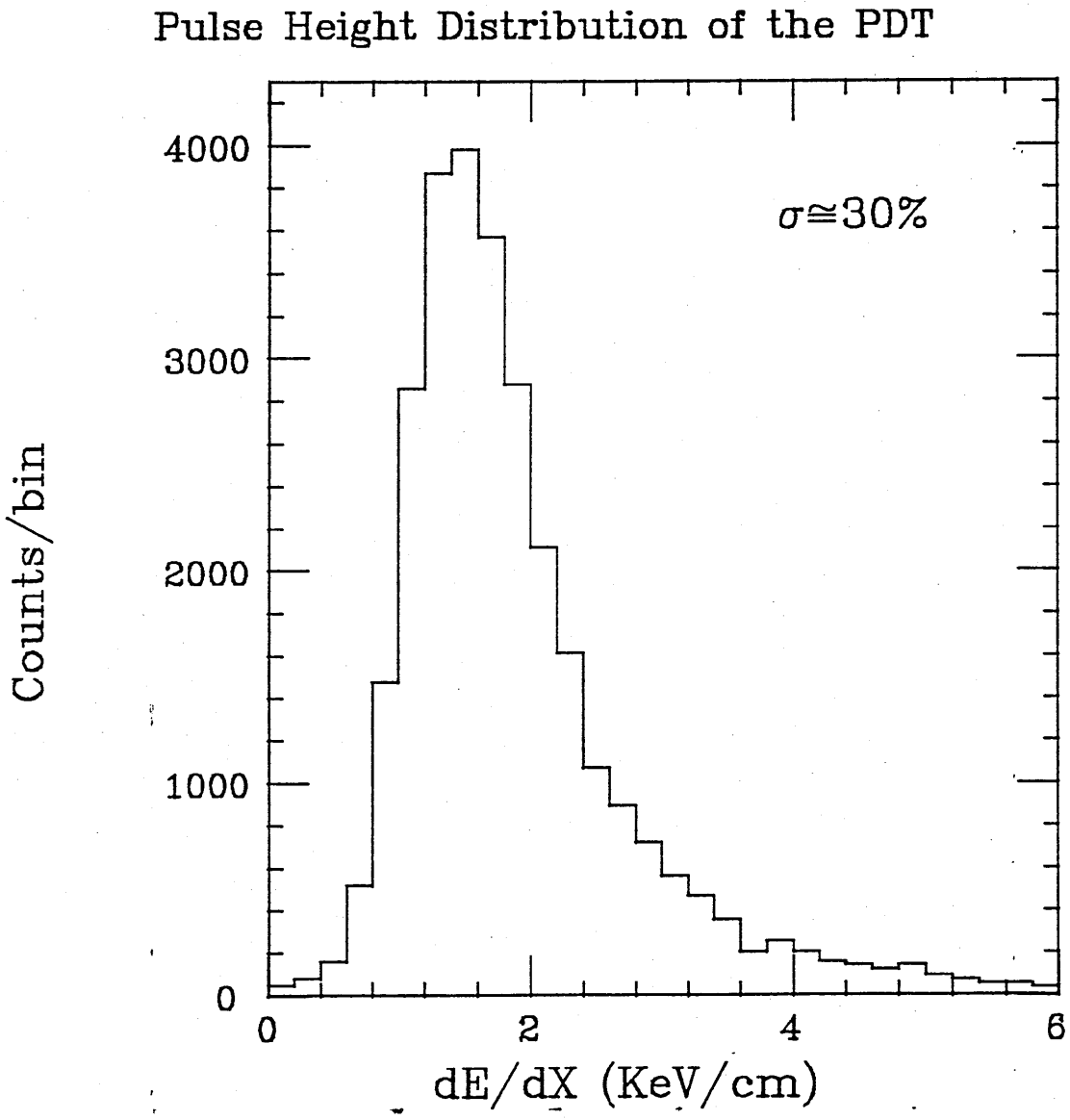
Pulse Height Distribution of the PDT
σ≅30%
Counts/bin
4000
3000
2000
1000
0
0
2
4
6
dE/dX (KeV/cm)

Figure 2.17

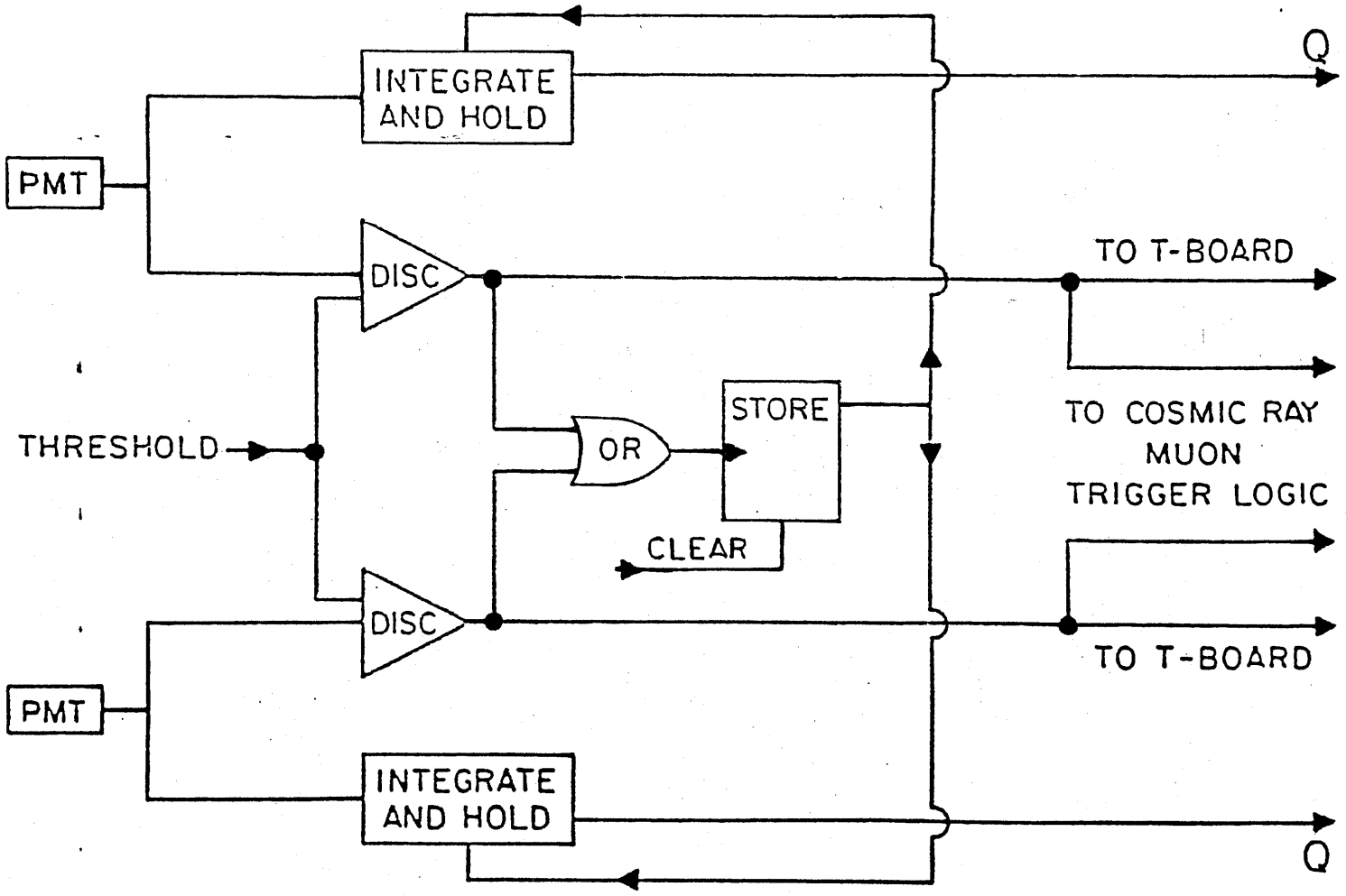
INTEGRATE AND HOLD
Q
PMT
DISC
TO T-BOARD
THRESHOLD
OR
STORE
TO COSMIC RAY MUON TRIGGER LOGIC
CLEAR
DISC
PMT
TO T-BOARD
INTEGRATE AND HOLD
Q

Figure 2.18

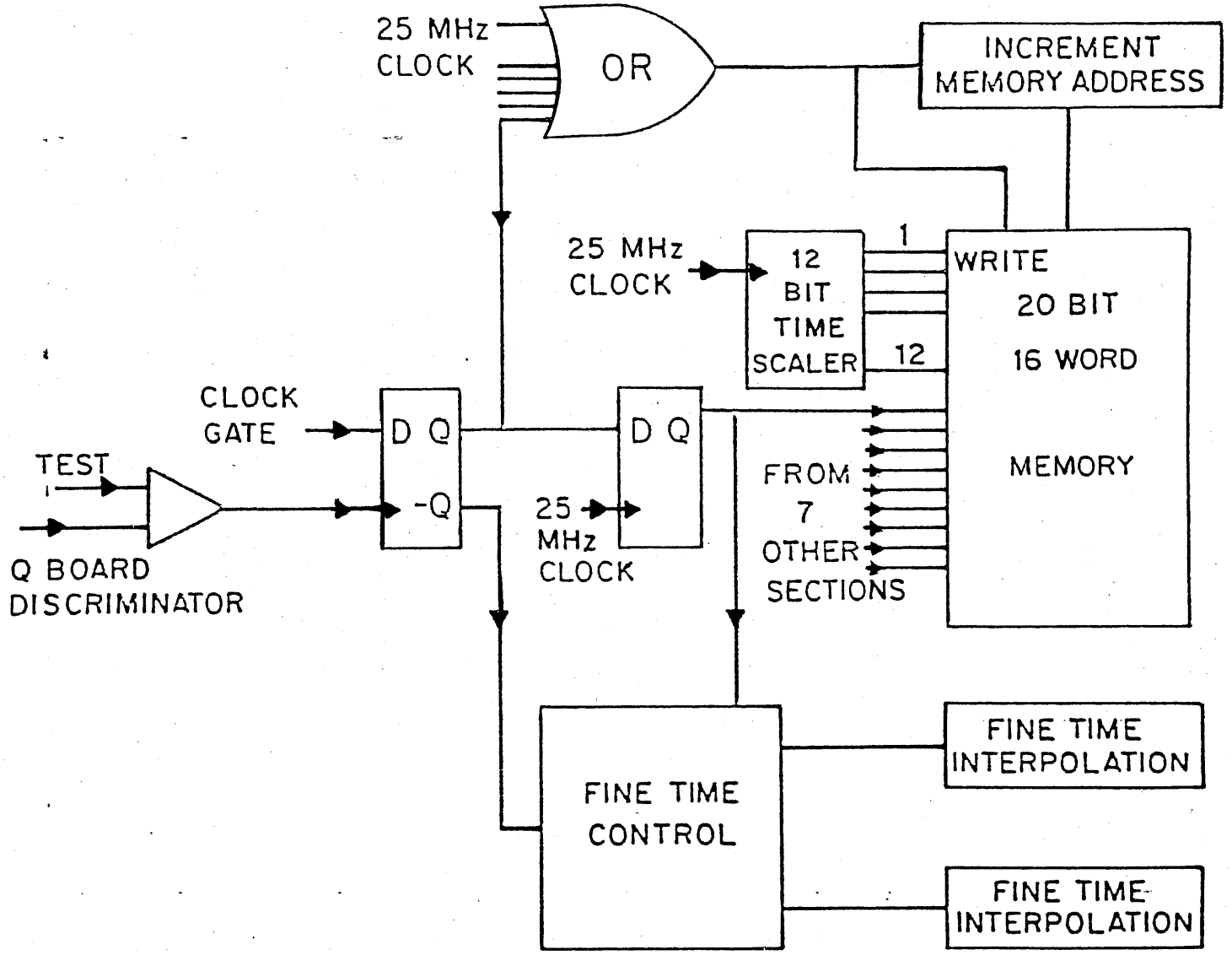
25 MHz
CLOCK
OR
INCREMENT
MEMORY ADDRESS
25 MHz
CLOCK
12
BIT
TIME
SCALER
1
12
WRITE
20 BIT
16 WORD
MEMORY
CLOCK
GATE
D Q
-Q
D Q
25
MHz
CLOCK
TEST
Q BOARD
DISCRIMINATOR
FROM
7
OTHER
SECTIONS
FINE TIME
CONTROL
FINE TIME
INTERPOLATION
FINE TIME
INTERPOLATION

Figure 2.19

ANALOG CARD

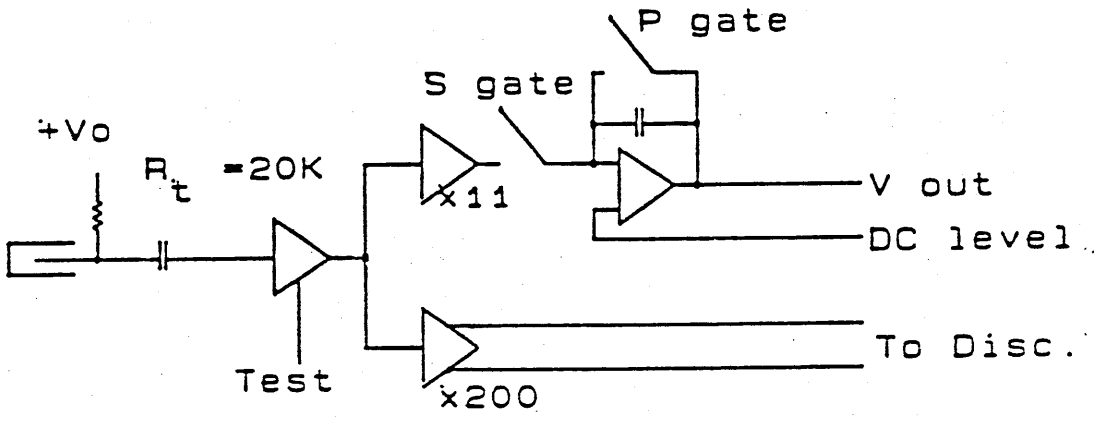

DIGITAL CARD

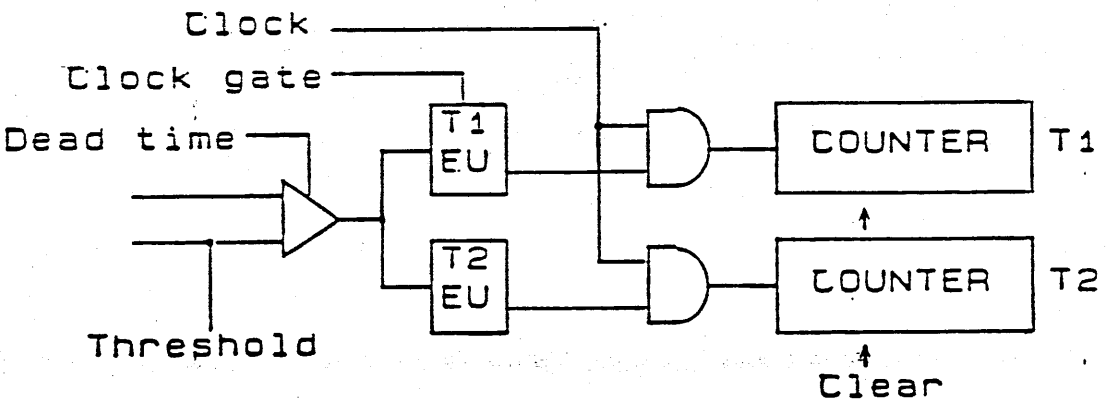

Time is measured with common stop

Least count is 10ns

The PDT electronics

Figure 2.20

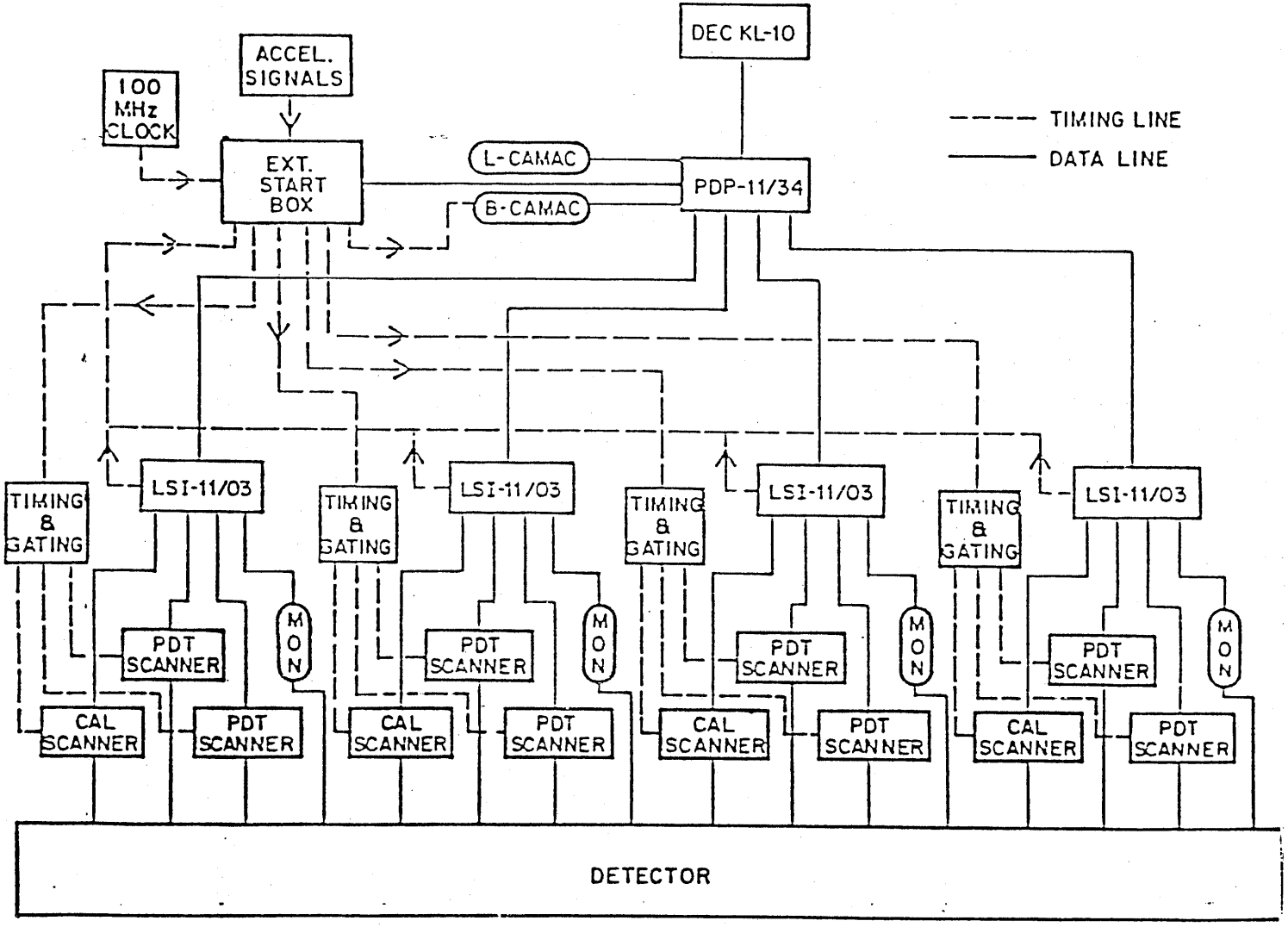
DEC KL-10
ACCEL. SIGNALS
100 MHz CLOCK
EXT. START BOX
L-CAMAC
B-CAMAC
PDP-11/34
TIMING LINE
DATA LINE
TIMING & GATING
LSI-11/03
PDT SCANNER
MON
CAL SCANNER
DETECTOR

Figure 2.21

Data Reduction Flow

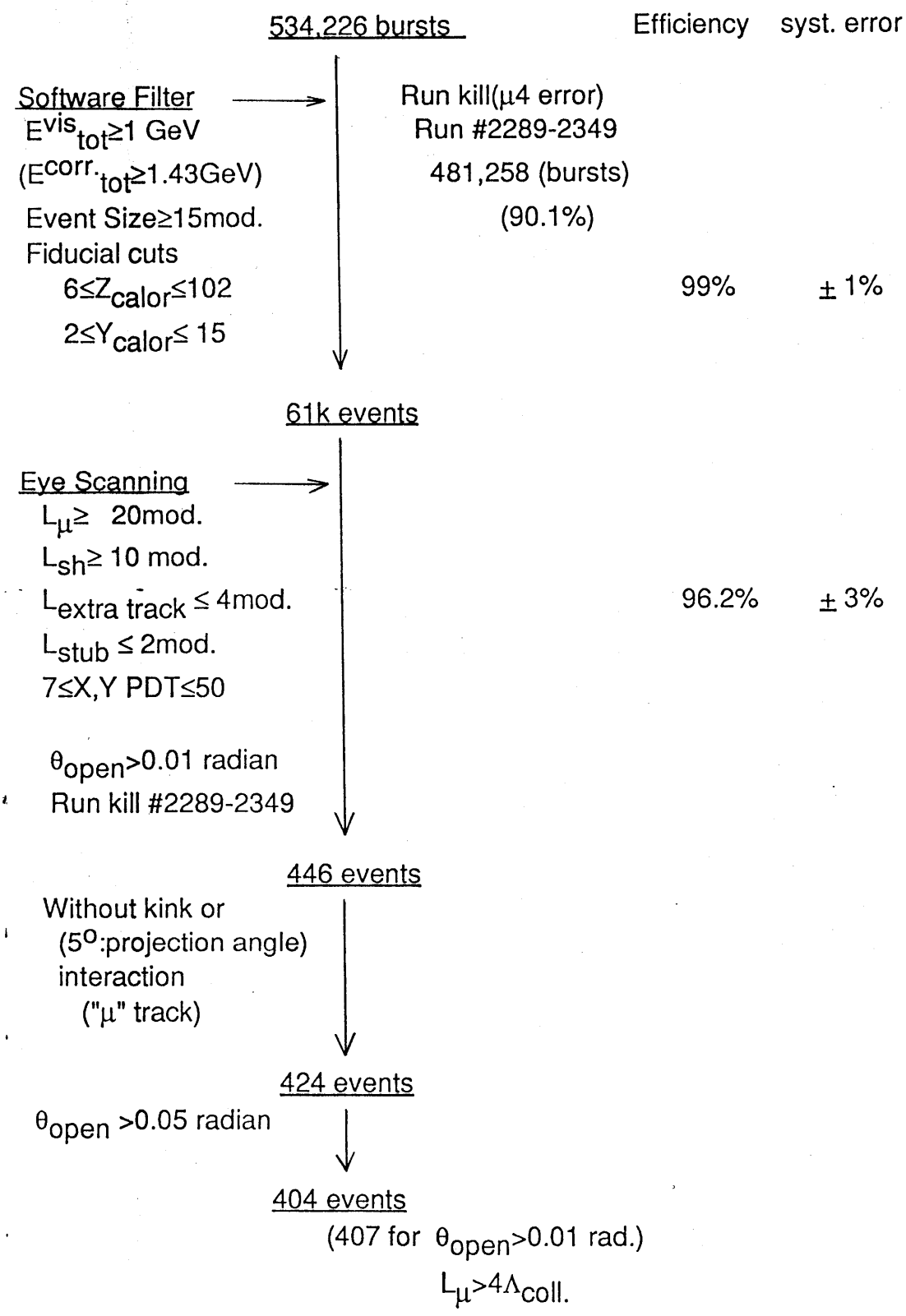

Figure 3.2

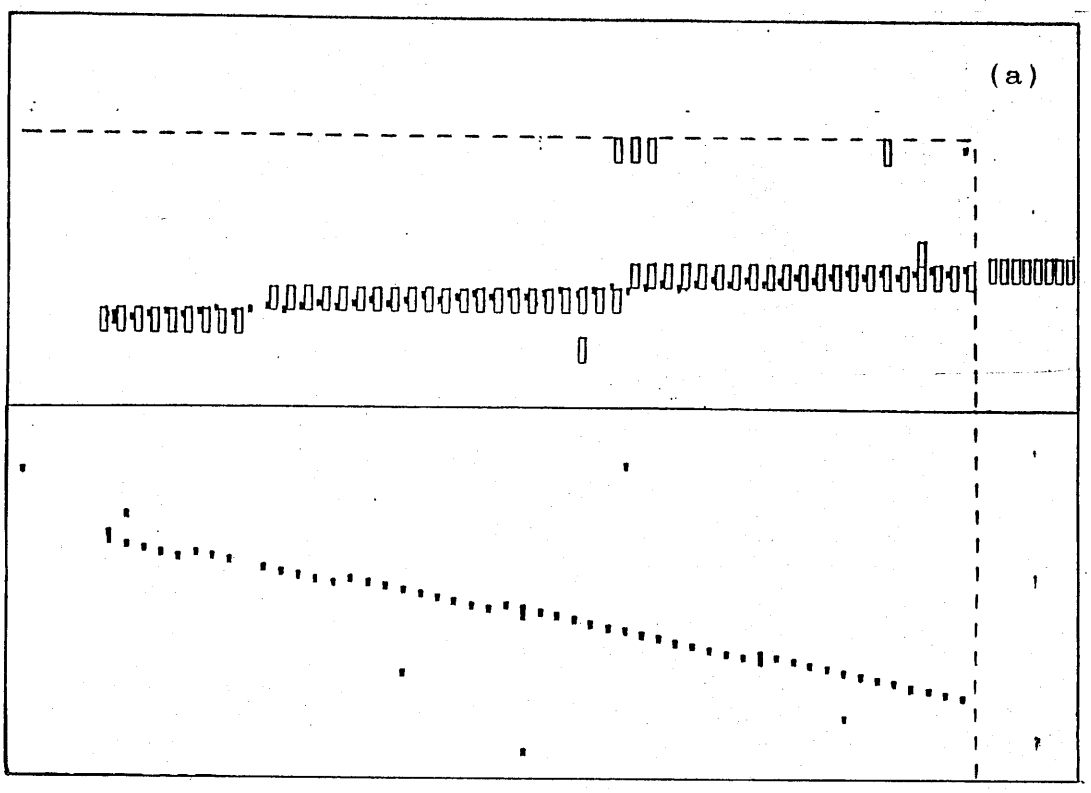

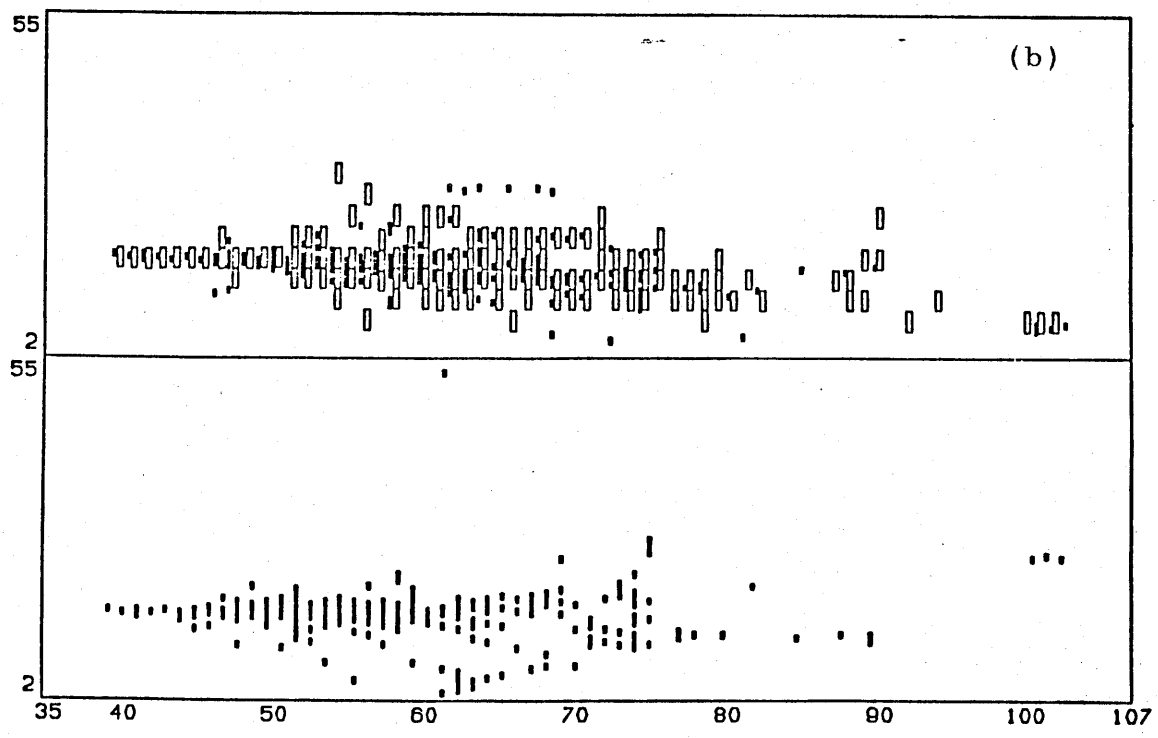

Figure 3.1

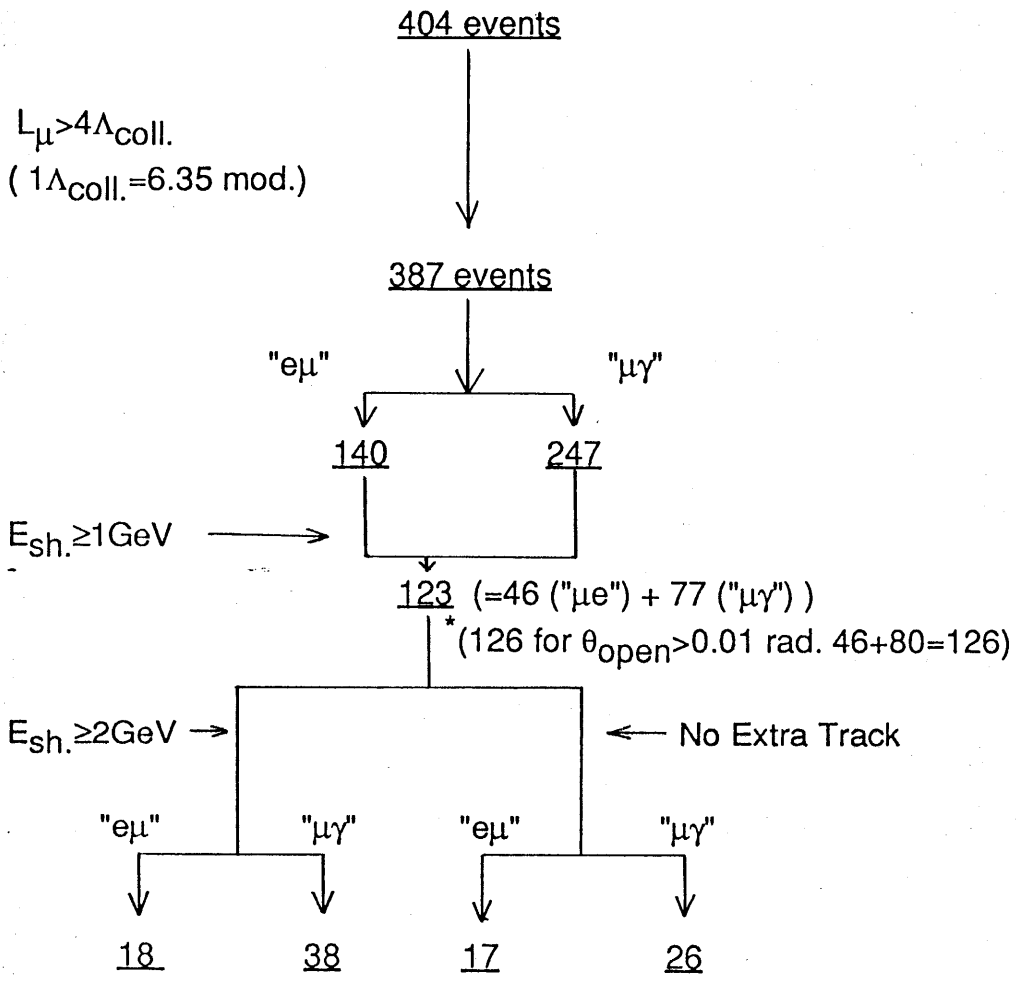
404 events
$L_\mu > 4\Lambda_{coll.}$
($1\Lambda_{coll.}$=6.35 mod.)
387 events
"eμ"
"μγ"
140
247
$E_{sh.} \geq 1$GeV
123 (=46 ("μe") + 77 ("μγ"))
*(126 for $\theta_{open} > 0.01$ rad. 46+80=126)
$E_{sh.} \geq 2$GeV
No Extra Track
"eμ"
"μγ"
"eμ"
"μγ"
18
38
17
26

Figure 3.2

A Time Clustering Example

All Time Clusters

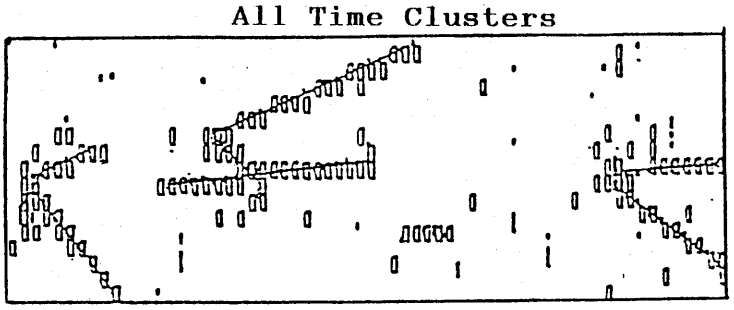

Time Cluster A

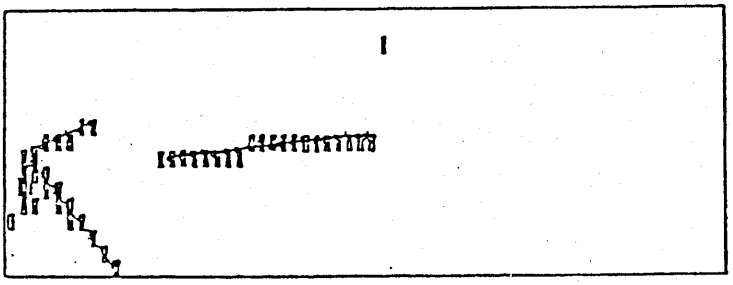

Time Cluster B

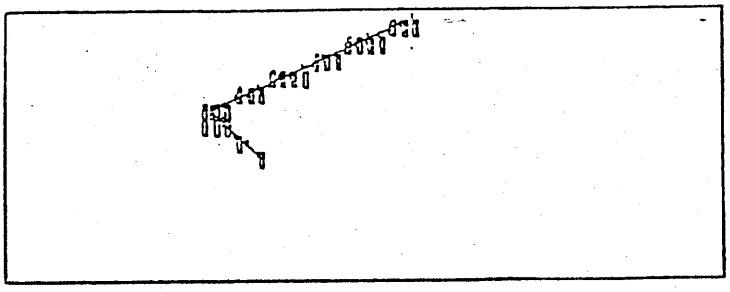

Time Cluster C

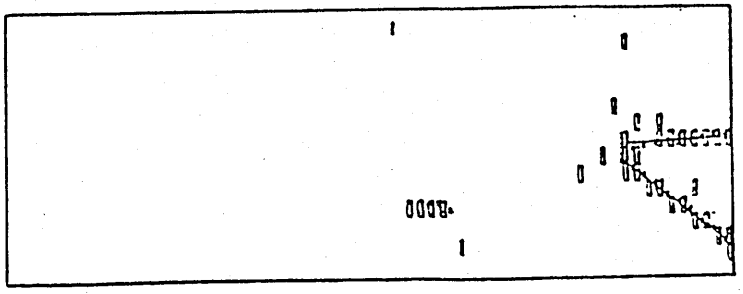

Figure 3.3

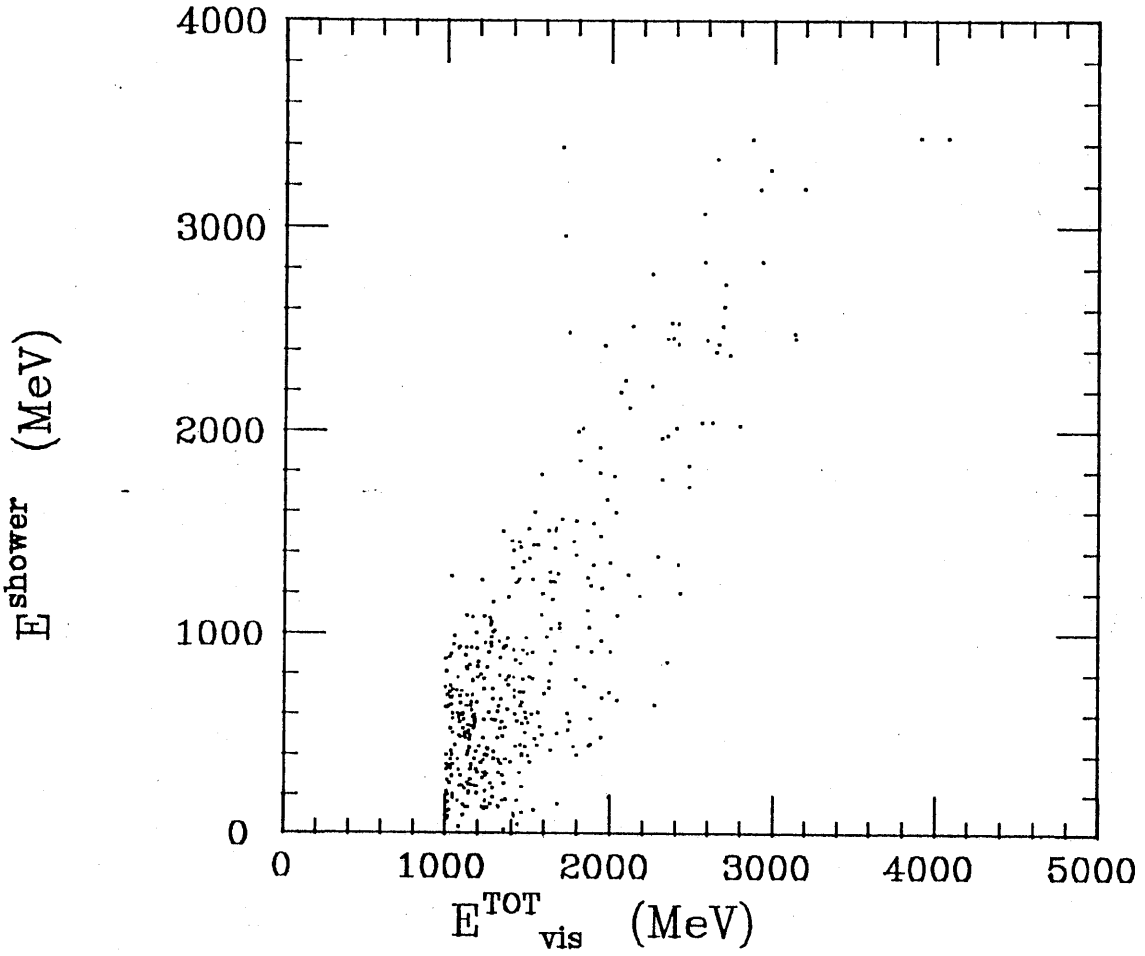
4000
3000
2000
1000
0
0
1000
2000
3000
4000
5000
E^{shower} (MeV)
E^{TOT}_{vis} (MeV)

Figure 3.4

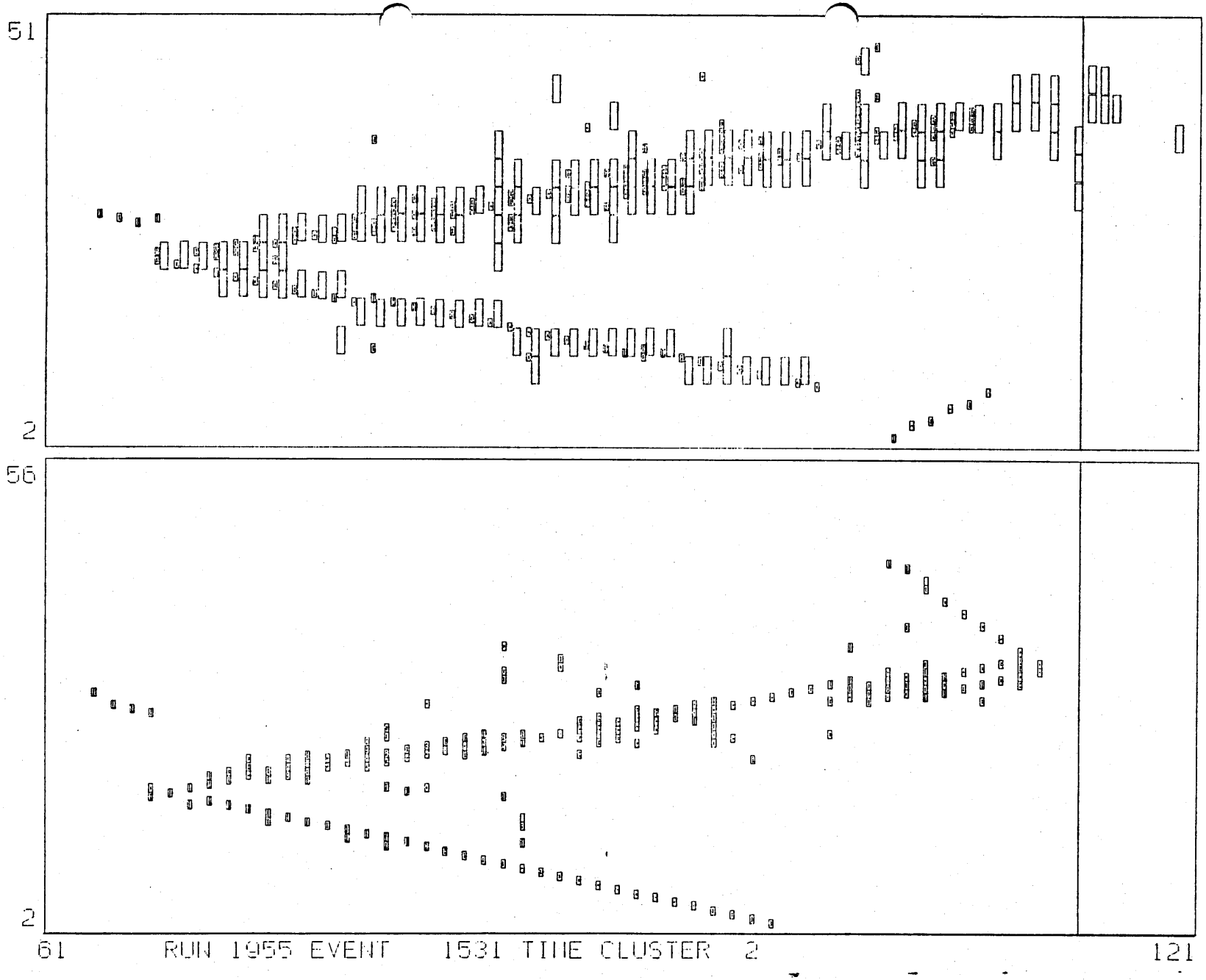

Figure 3.5

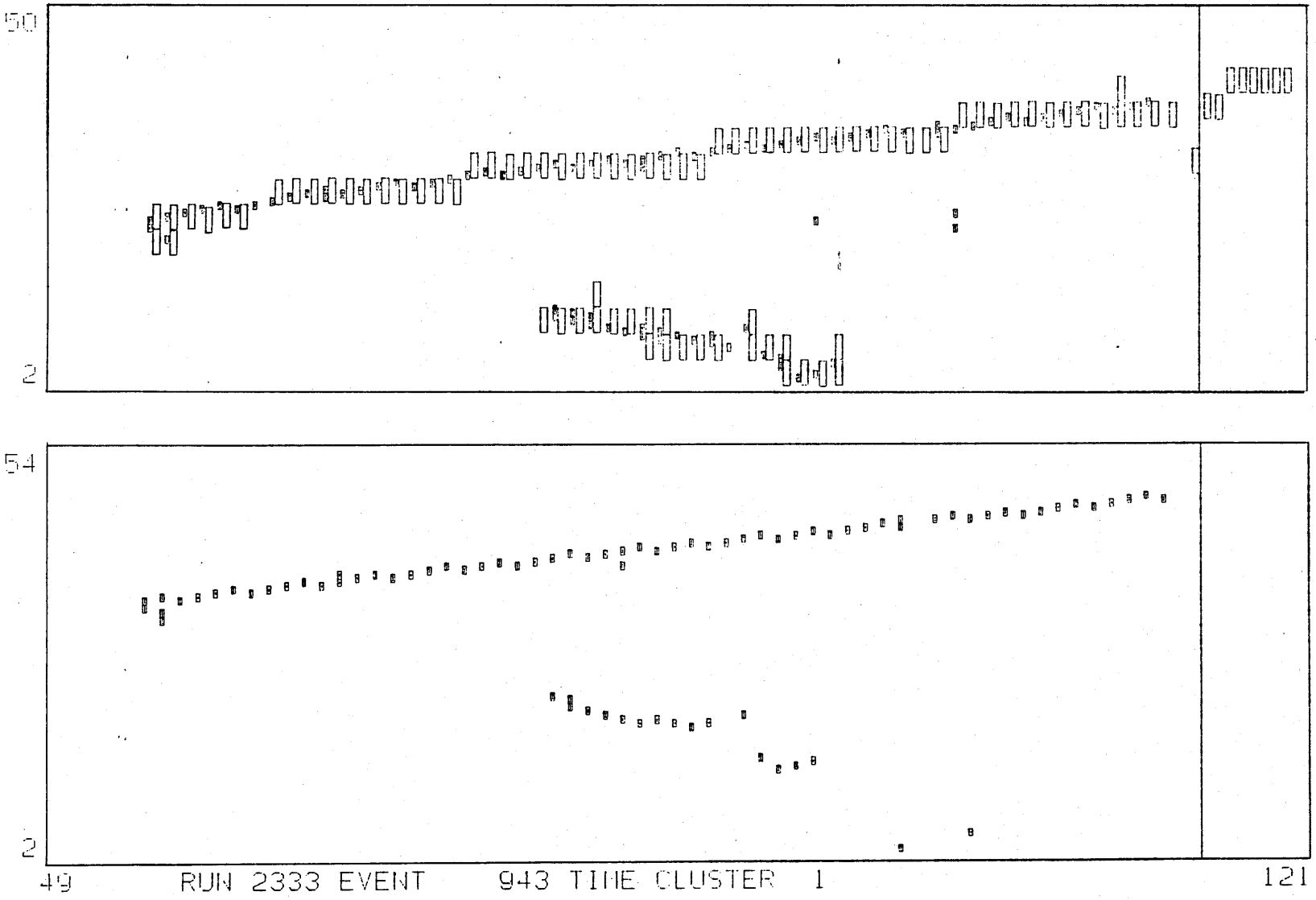

Figure 3.6

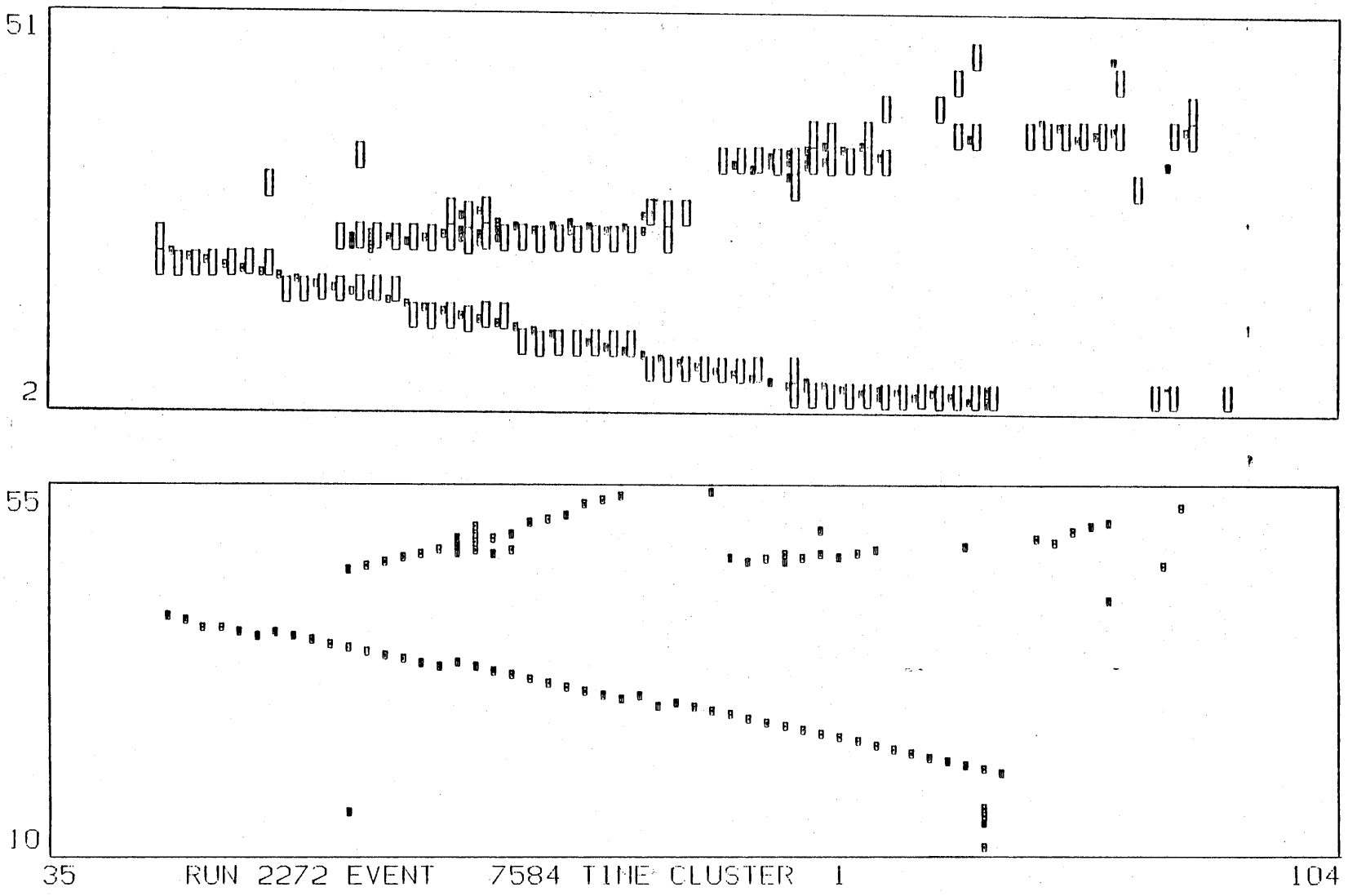

Figure 3.7

Data Reduction Flow

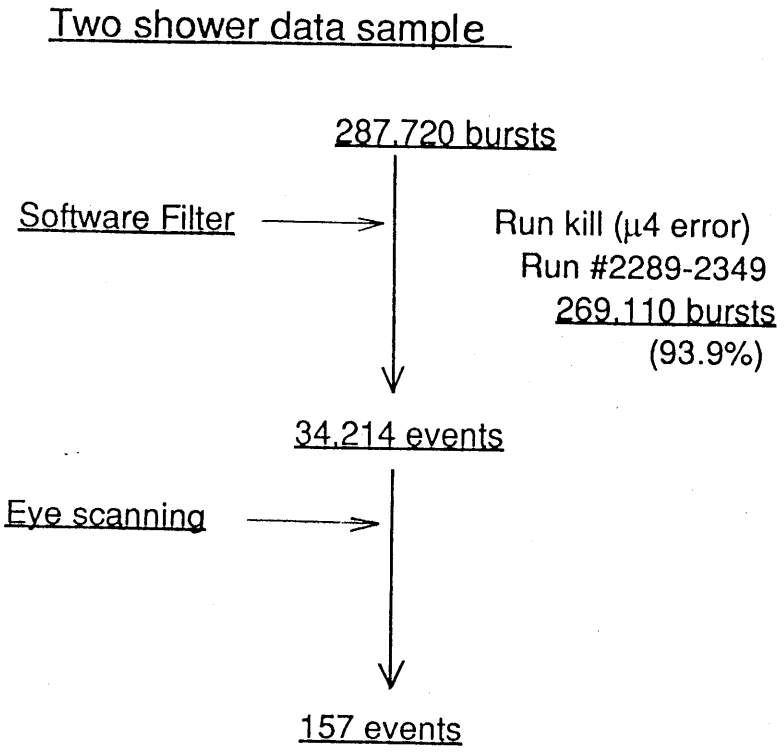

Figure 3.8

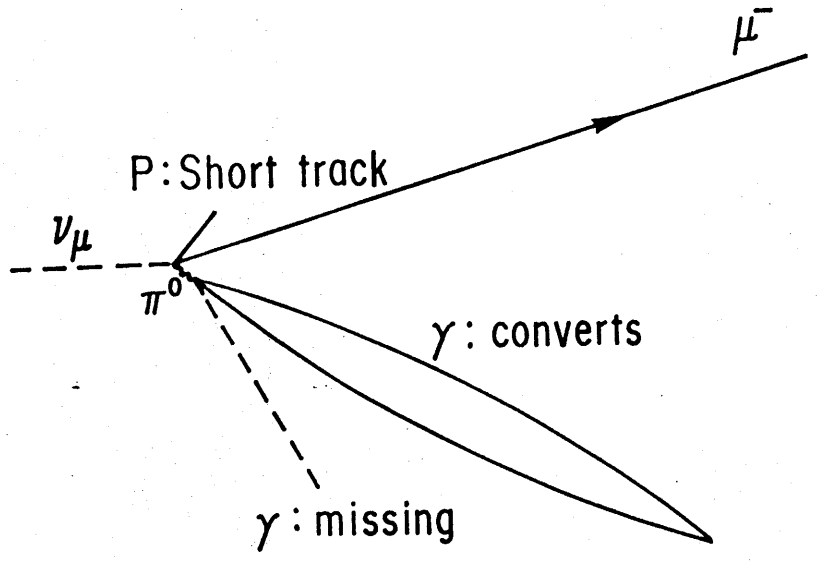

$$\nu_\mu n \rightarrow \mu^- P \pi^0$$

Figure 3.9

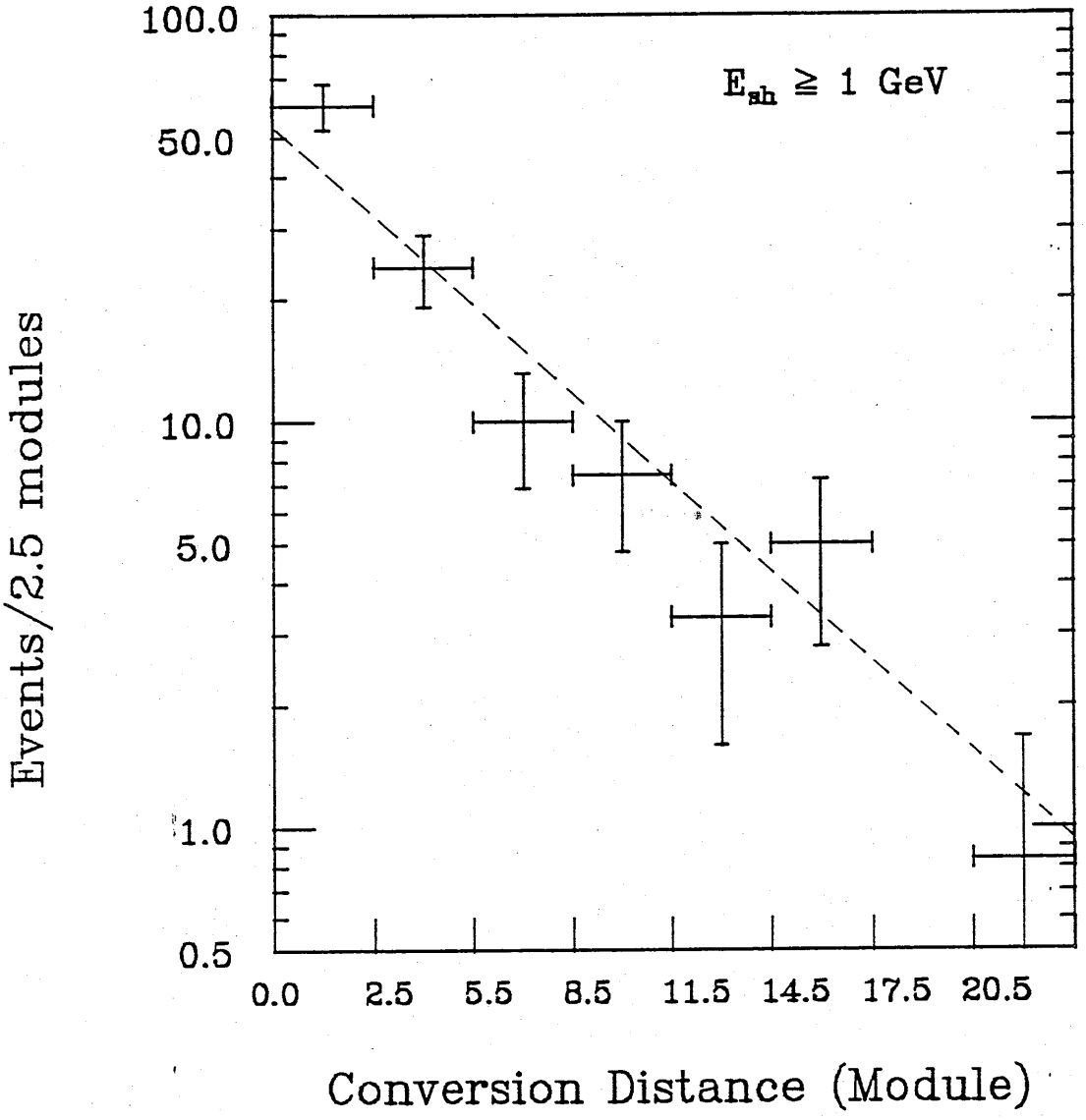
100.0
50.0
10.0
5.0
1.0
0.5
$E_{sh} \geqq 1$ GeV
Events/2.5 modules
0.0
2.5
5.5
8.5
11.5
14.5
17.5
20.5
Conversion Distance (Module)

Figure 3.10

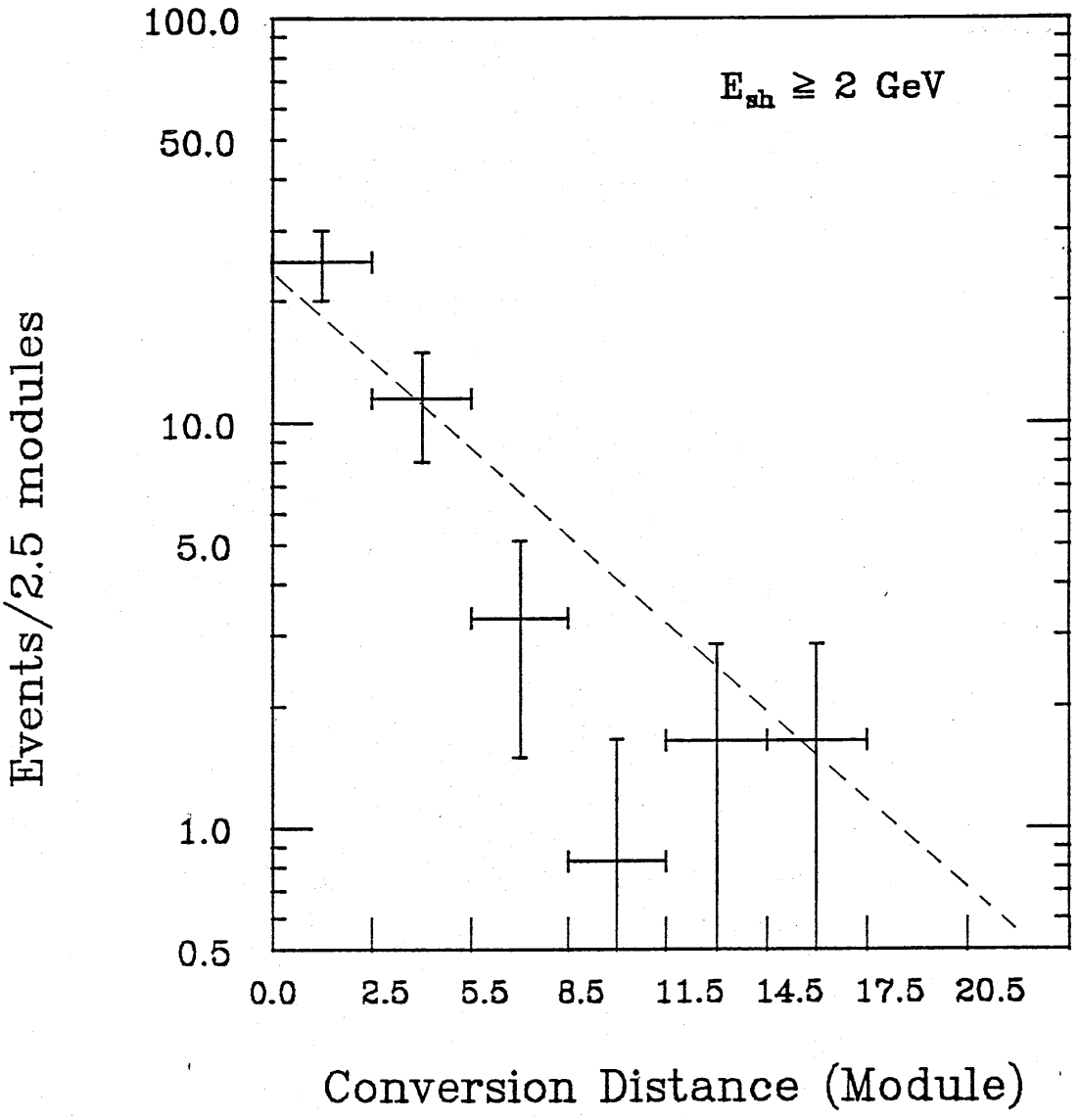
100.0
50.0
10.0
5.0
1.0
0.5
$E_{sh} \geqq 2$ GeV
Events/2.5 modules
0.0
2.5
5.5
8.5
11.5
14.5
17.5
20.5
Conversion Distance (Module)

Figure 3.11

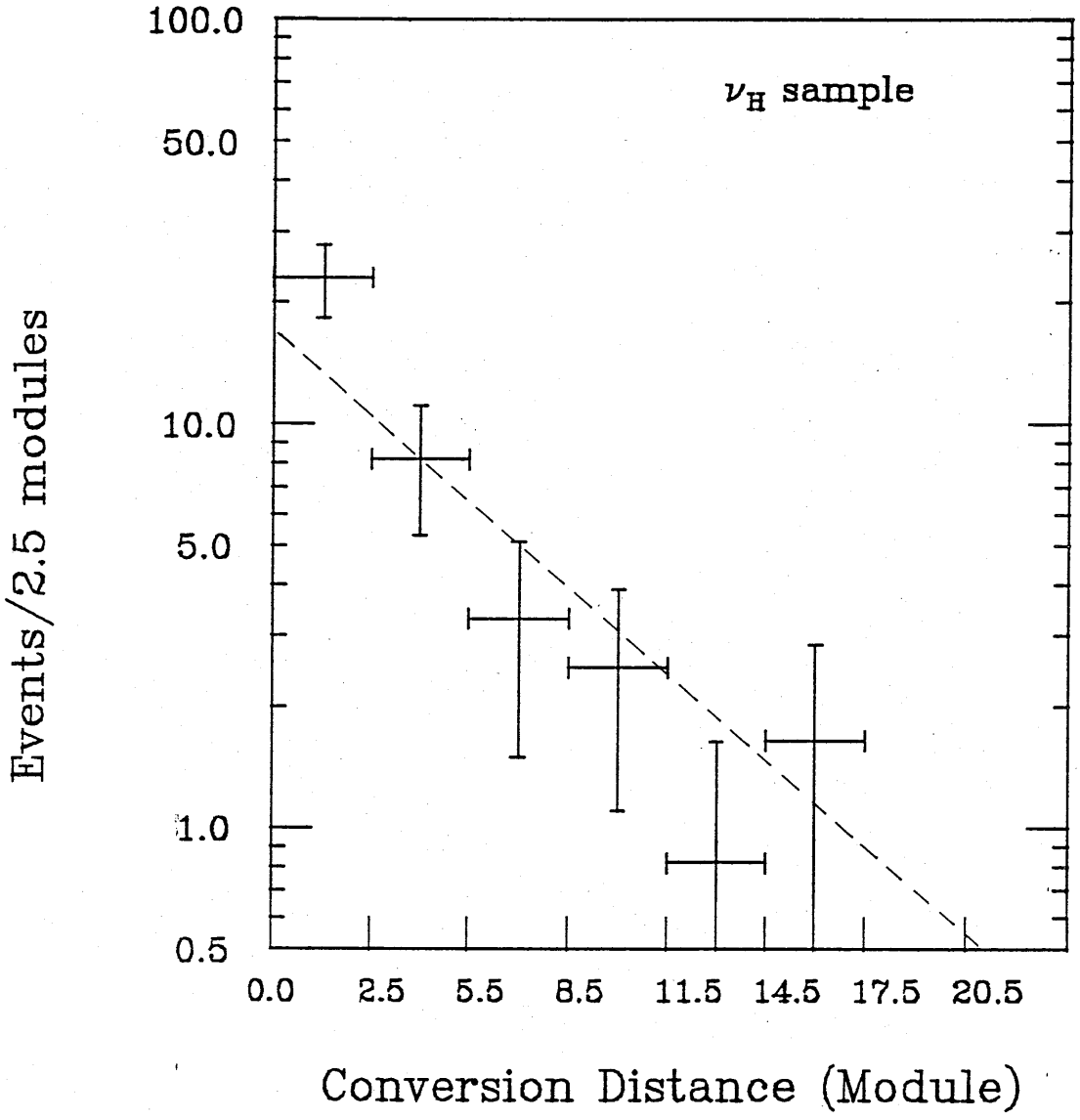
100.0
50.0
10.0
5.0
1.0
0.5
ν_H sample
Events/2.5 modules
0.0
2.5
5.5
8.5
11.5
14.5
17.5
20.5
Conversion Distance (Module)

Figure 3.12

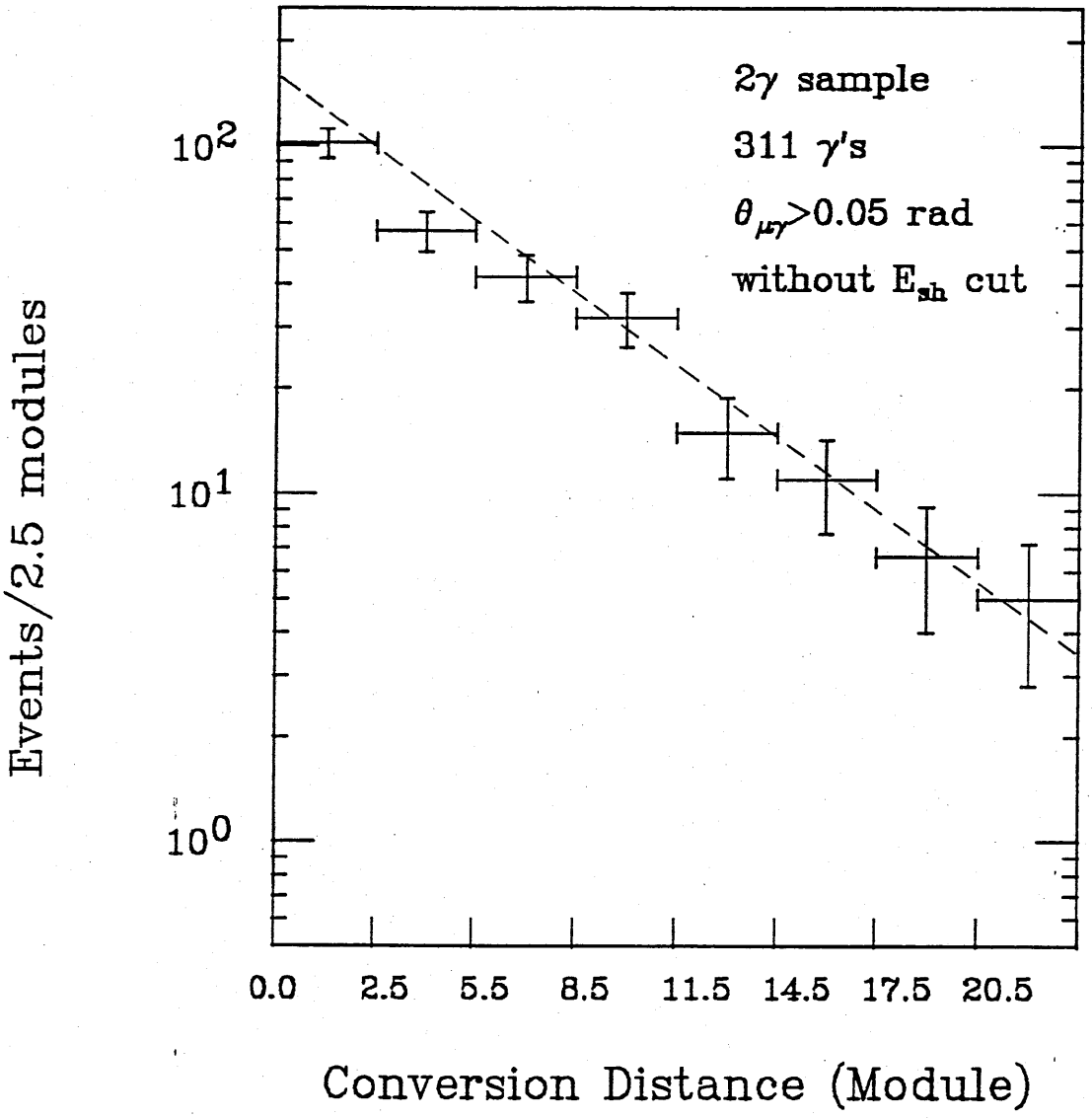
2γ sample
311 γ's
θμγ>0.05 rad
without Esh cut
10^2
10^1
10^0
Events/2.5 modules
0.0
2.5
5.5
8.5
11.5
14.5
17.5
20.5
Conversion Distance (Module)

Figure 3.13

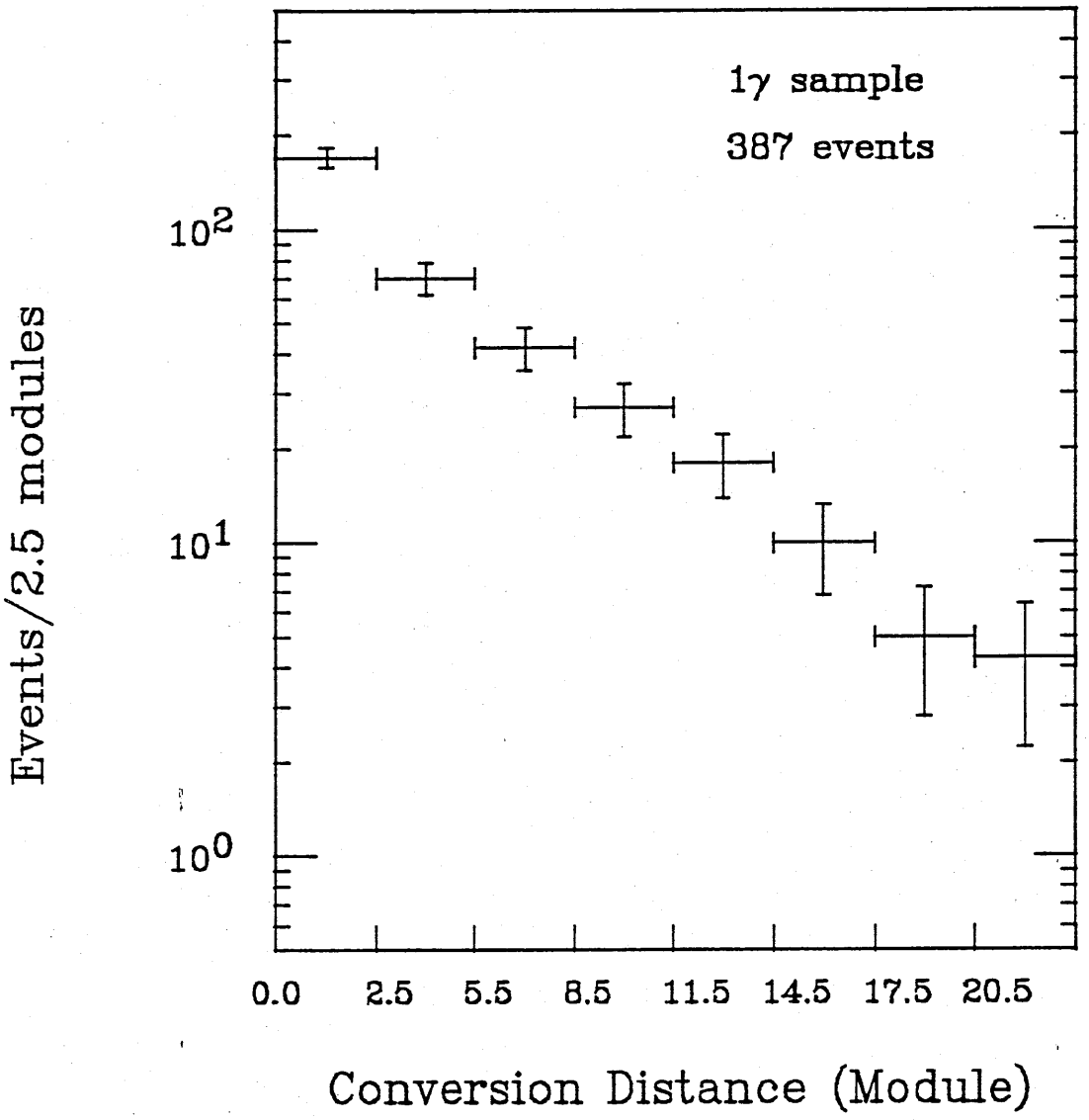
1γ sample
387 events
Events/2.5 modules
10^2
10^1
10^0
0.0
2.5
5.5
8.5
11.5
14.5
17.5
20.5
Conversion Distance (Module)

Figure 3.14

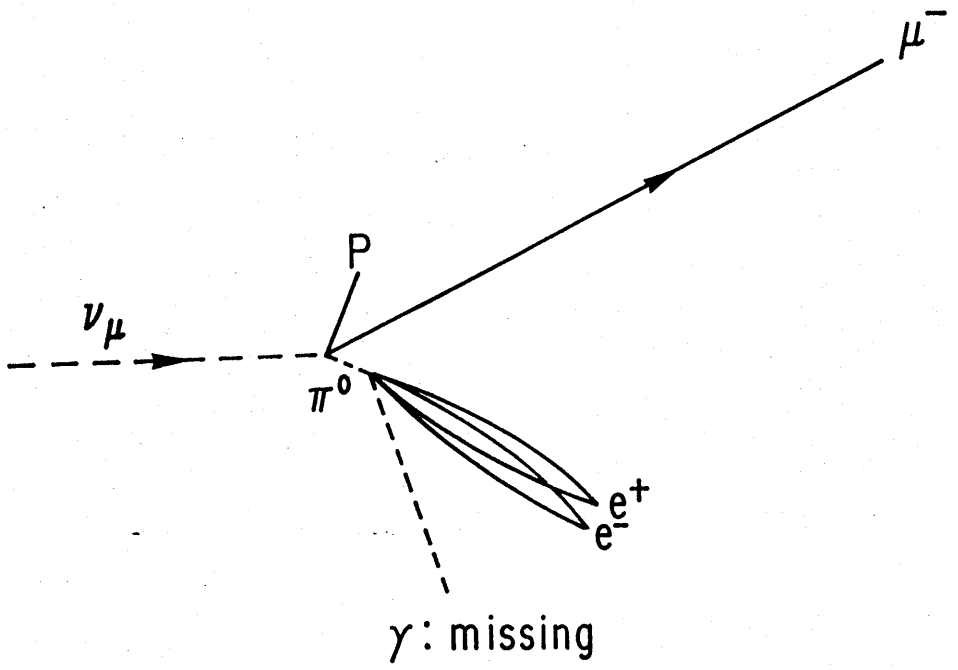

$$\nu_\mu n \rightarrow \mu^- P \pi^0$$
$$\hookrightarrow e^+ e^- \gamma$$

Figure 3.15

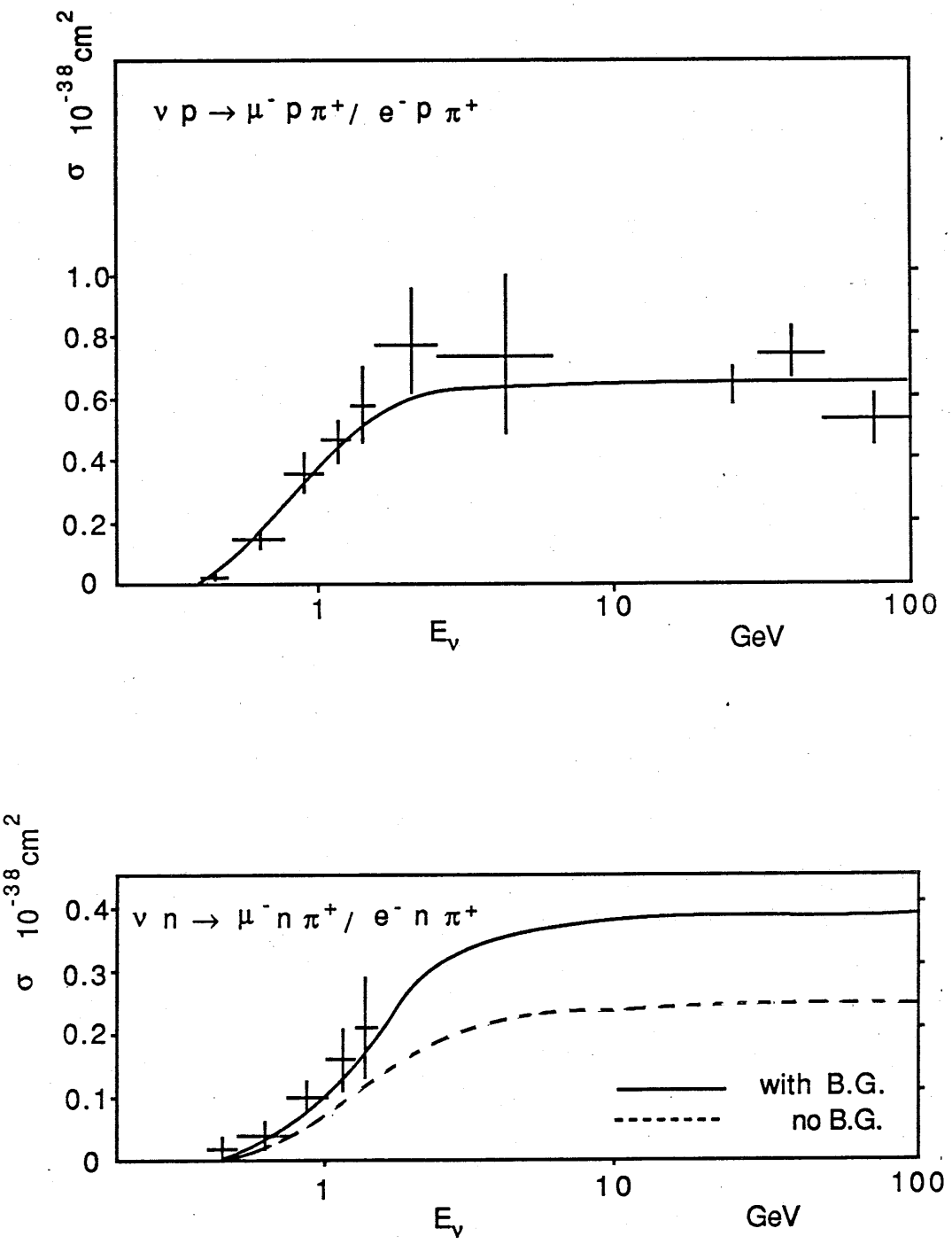
σ 10^-38 cm^2
ν p → μ⁻ p π⁺/ e⁻ p π⁺
1.0
0.8
0.6
0.4
0.2
0
1
10
100
E_ν
GeV
σ 10^-38 cm^2
ν n → μ⁻ n π⁺/ e⁻ n π⁺
0.4
0.3
0.2
0.1
0
with B.G.
no B.G.
1
10
100
E_ν
GeV

Figure 3.16

Data Reduction Flow

$e^-p\pi^+$, $e^-n\pi^+$ M.C. (Δ only based on Rein-Sehgal Model)

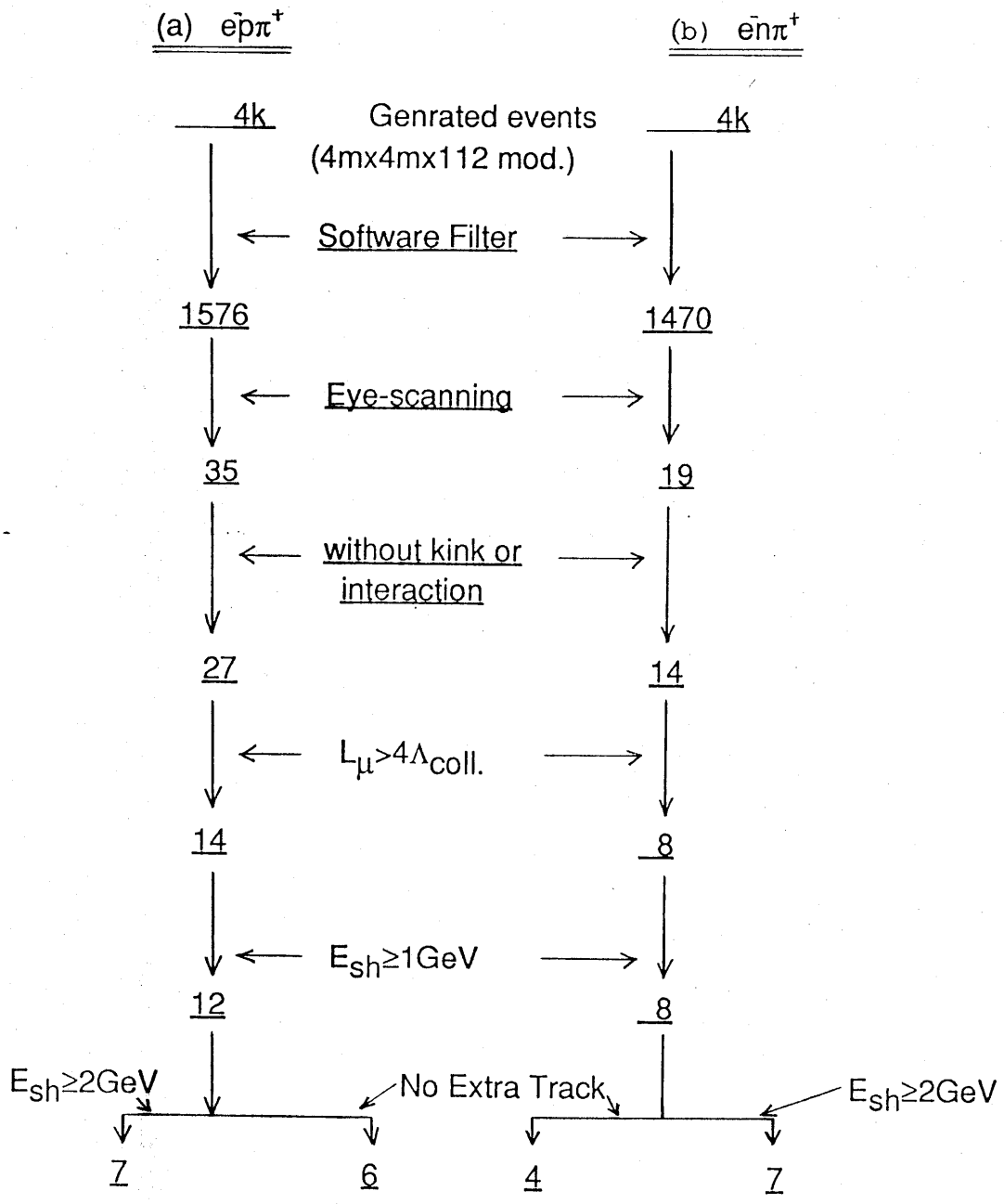

Figure 3.17

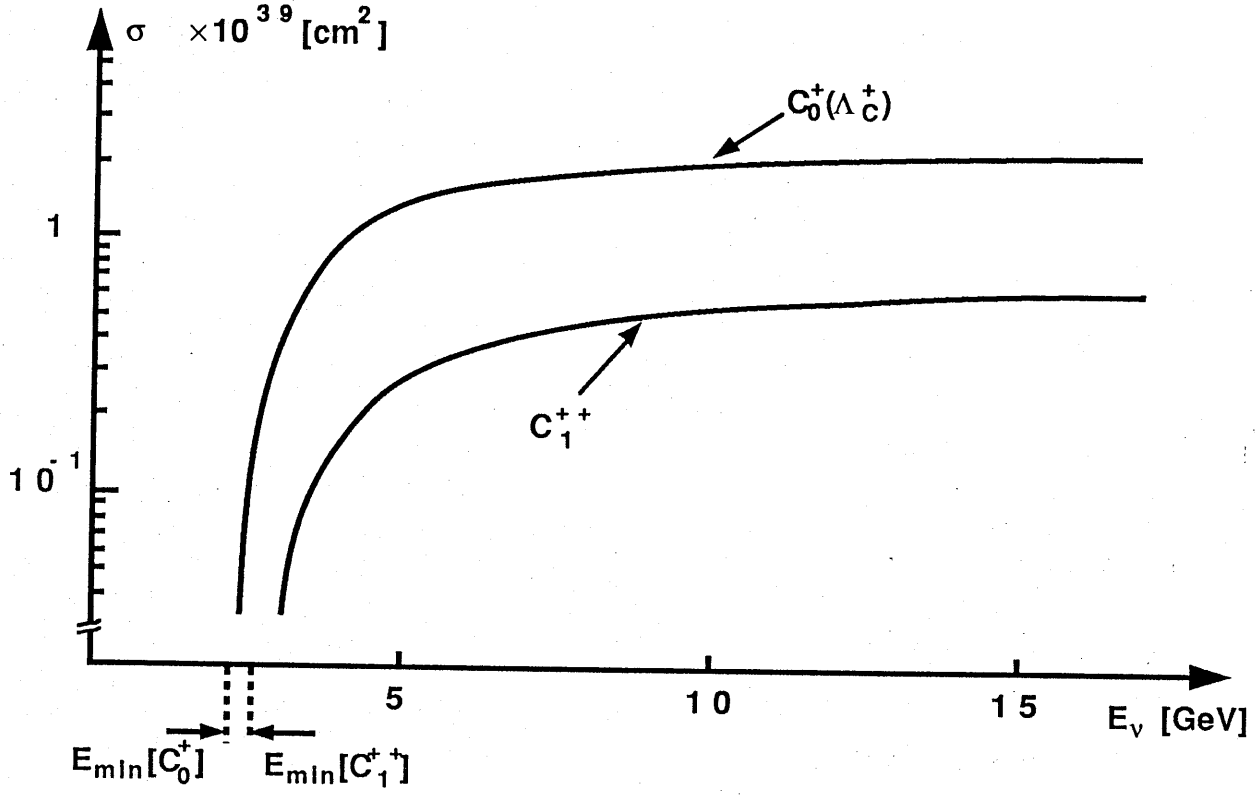

Figure 3.18

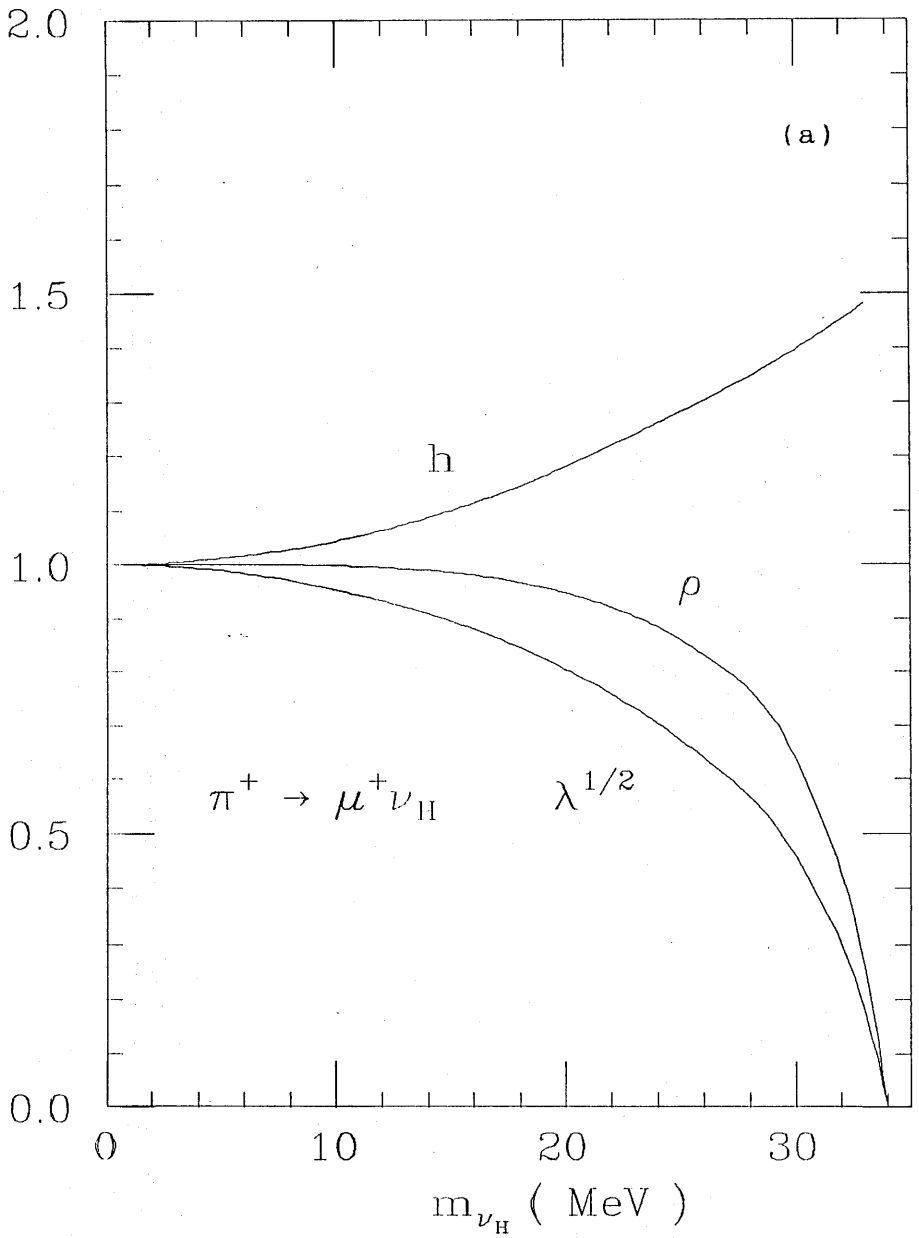
2.0
1.5
1.0
0.5
0.0
(a)
h
ρ
$\pi^+ \rightarrow \mu^+ \nu_H$
$\lambda^{1/2}$
0
10
20
30
m_{ν_H} (MeV)

Figure 4.1

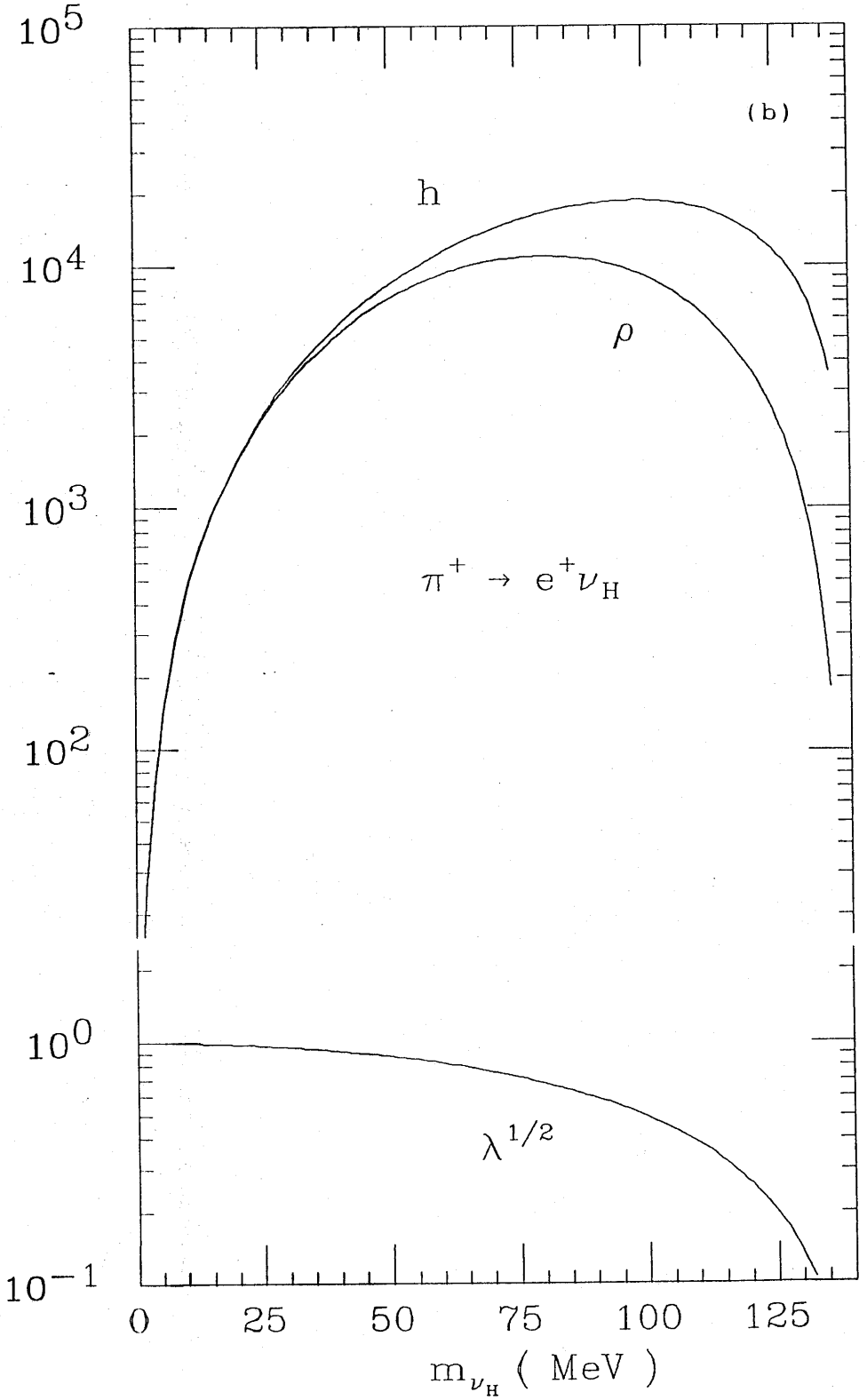
(b)
h
ρ
$\pi^+ \rightarrow e^+ \nu_H$
$\lambda^{1/2}$
10^5
10^4
10^3
10^2
10^0
10^{-1}
0
25
50
75
100
125
m_{ν_H} (MeV)

Figure 4.1

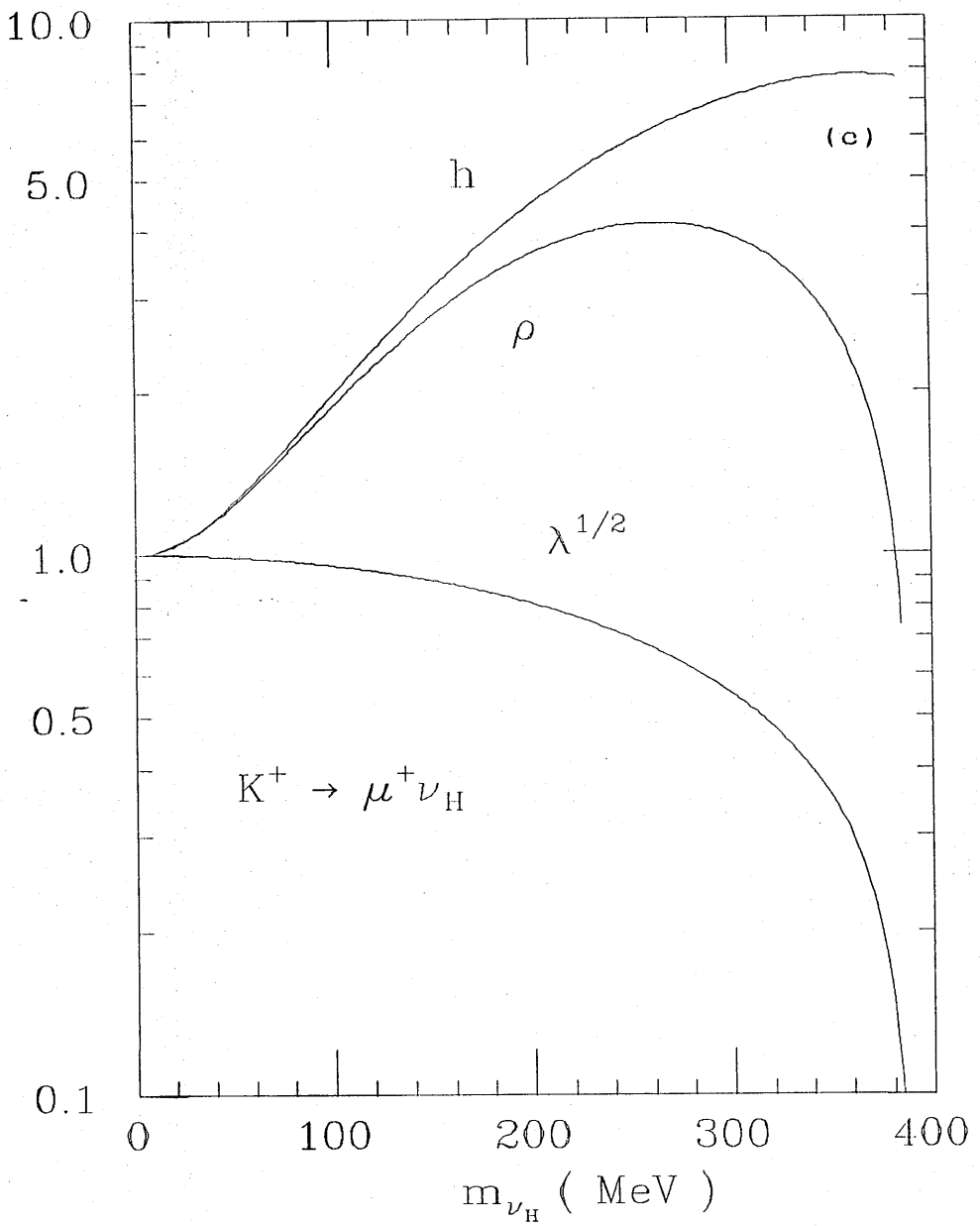

Figure 4.1

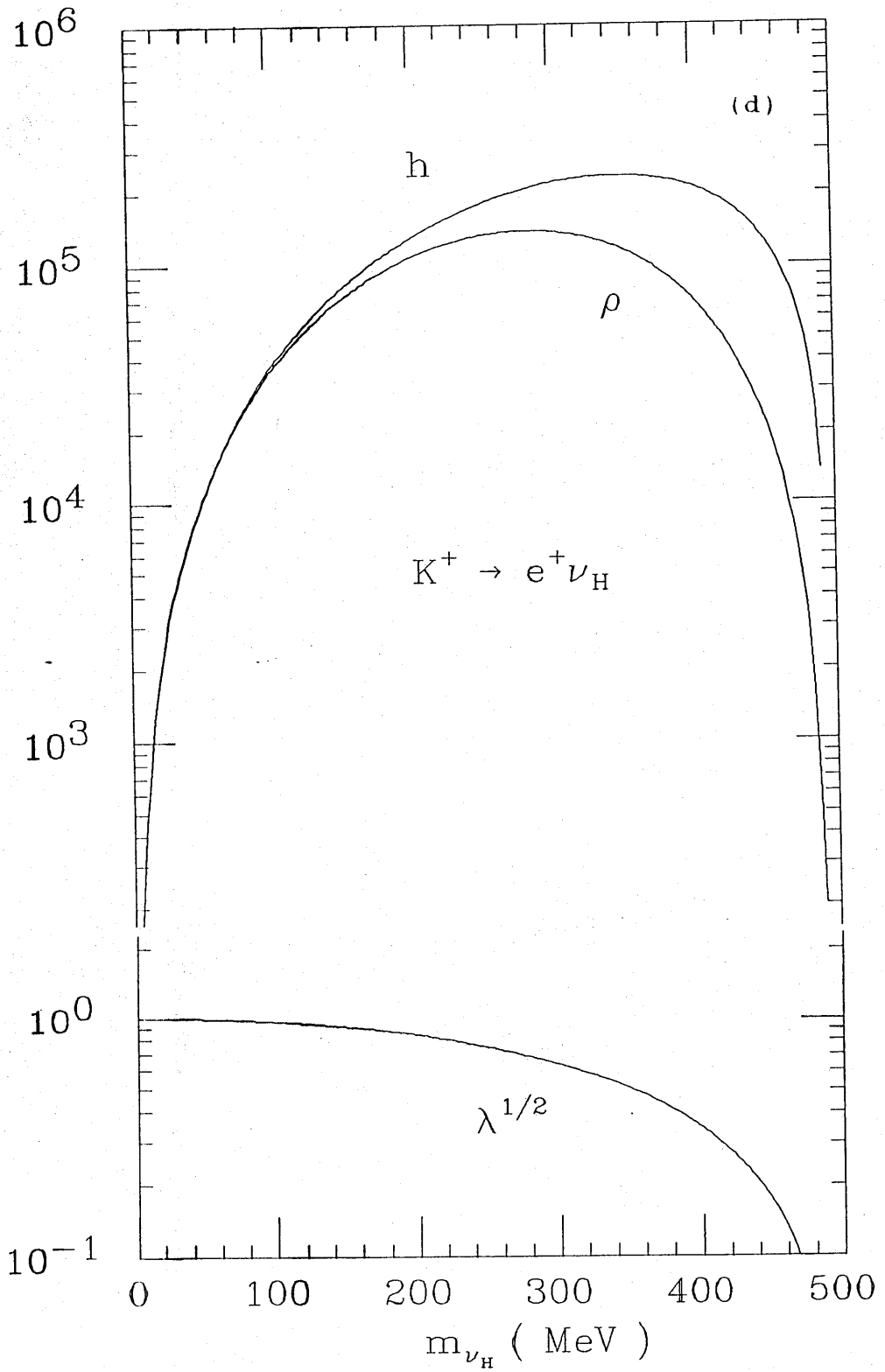
(d)
h
ρ
$K^+ \rightarrow e^+ \nu_H$
$\lambda^{1/2}$
10^6
10^5
10^4
10^3
10^0
10^{-1}
0
100
200
300
400
500
m_{ν_H} (MeV)

Figure 4.1

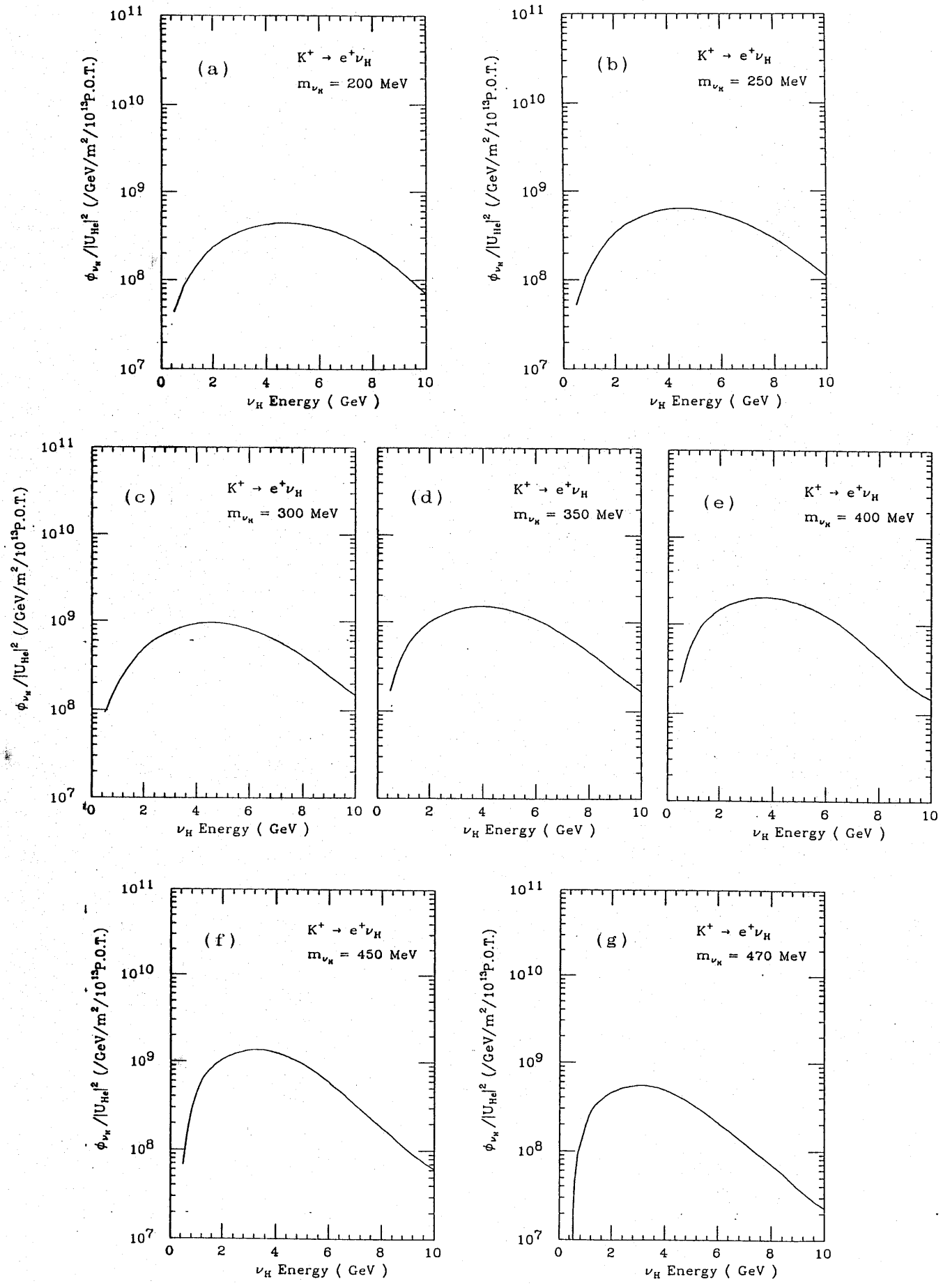
(a)
$K^+ \to e^+\nu_H$
m_{ν_H} = 200 MeV
(b)
$K^+ \to e^+\nu_H$
m_{ν_H} = 250 MeV
(c)
$K^+ \to e^+\nu_H$
m_{ν_H} = 300 MeV
(d)
$K^+ \to e^+\nu_H$
m_{ν_H} = 350 MeV
(e)
$K^+ \to e^+\nu_H$
m_{ν_H} = 400 MeV
(f)
$K^+ \to e^+\nu_H$
m_{ν_H} = 450 MeV
(g)
$K^+ \to e^+\nu_H$
m_{ν_H} = 470 MeV
$\phi_{\nu_H}/|U_{He}|^2$ (/GeV/m^2/10^{13}P.O.T.)
ν_H Energy (GeV)

Figure 4.2

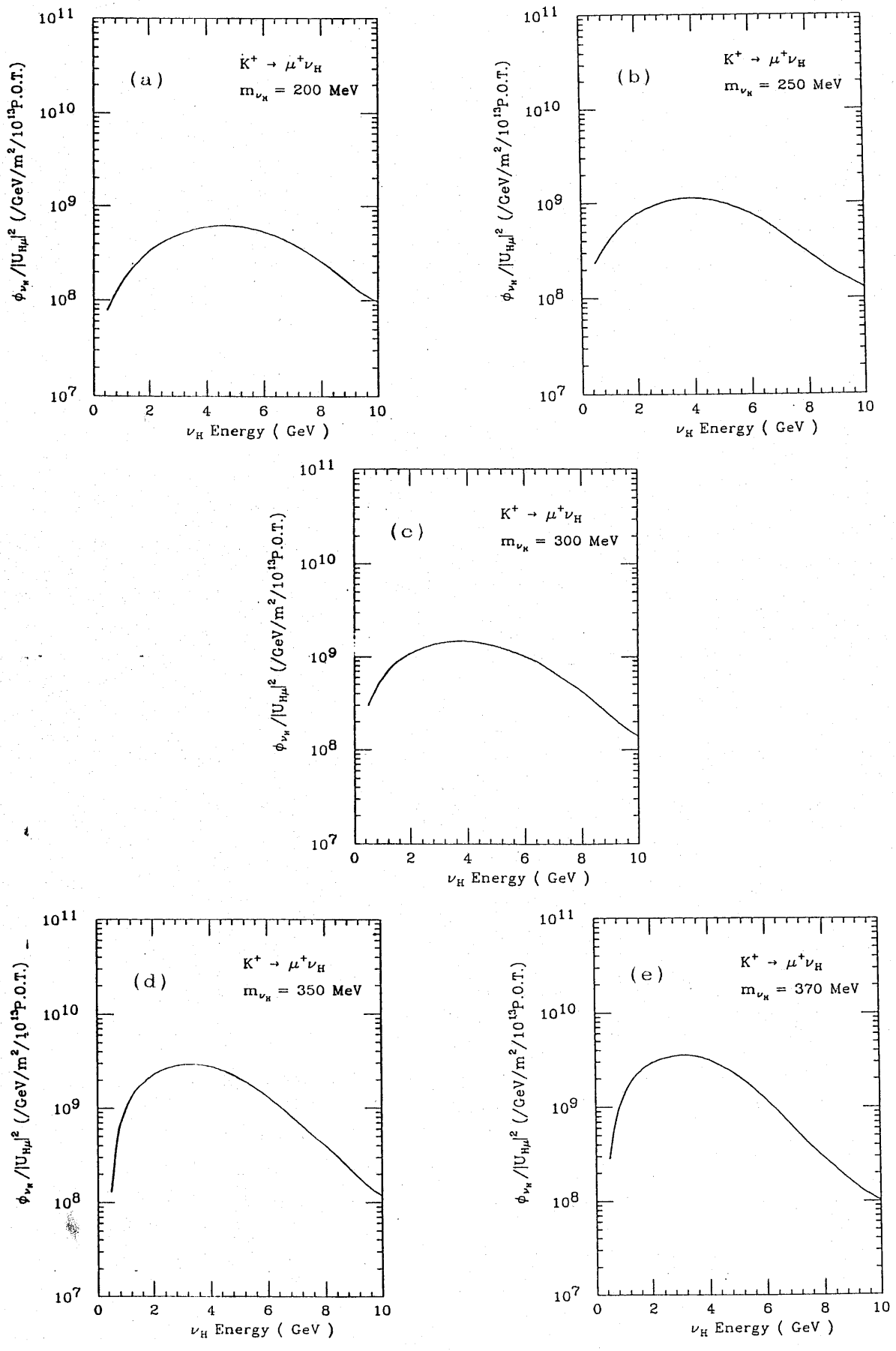
(a)
$K^+ \rightarrow \mu^+ \nu_H$
m_{ν_H} = 200 MeV
(b)
$K^+ \rightarrow \mu^+ \nu_H$
m_{ν_H} = 250 MeV
(c)
$K^+ \rightarrow \mu^+ \nu_H$
m_{ν_H} = 300 MeV
(d)
$K^+ \rightarrow \mu^+ \nu_H$
m_{ν_H} = 350 MeV
(e)
$K^+ \rightarrow \mu^+ \nu_H$
m_{ν_H} = 370 MeV
$\phi_{\nu_H}/|U_{H\mu}|^2$ (/GeV/m^2/10^{13}P.O.T.)
ν_H Energy (GeV)

Figure 4.3

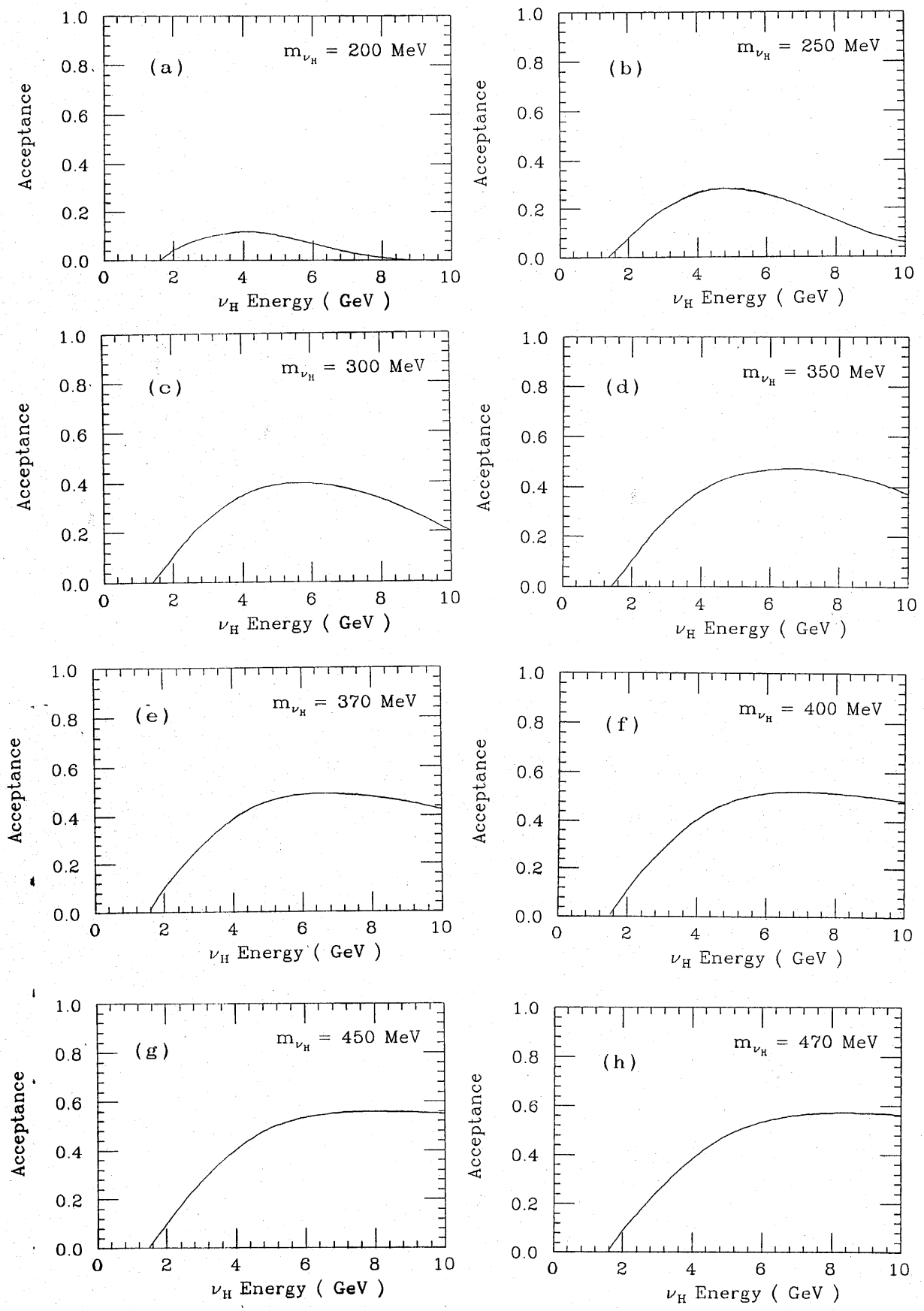
(a)
m_{ν_H} = 200 MeV
(b)
m_{ν_H} = 250 MeV
(c)
m_{ν_H} = 300 MeV
(d)
m_{ν_H} = 350 MeV
(e)
m_{ν_H} = 370 MeV
(f)
m_{ν_H} = 400 MeV
(g)
m_{ν_H} = 450 MeV
(h)
m_{ν_H} = 470 MeV
Acceptance
ν_H Energy (GeV)

Figure 4.4

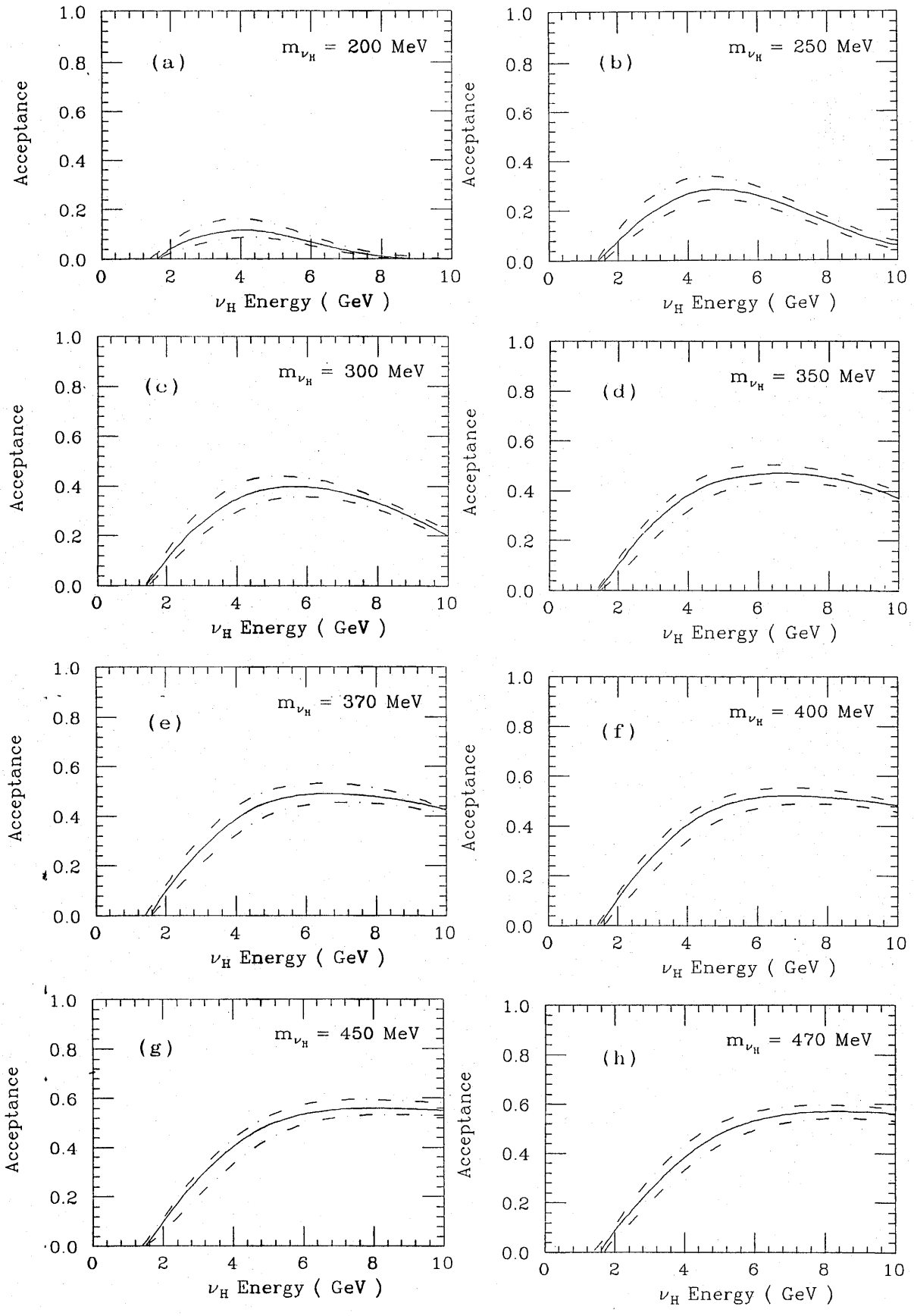
(a)
m_{ν_H} = 200 MeV
(b)
m_{ν_H} = 250 MeV
(c)
m_{ν_H} = 300 MeV
(d)
m_{ν_H} = 350 MeV
(e)
m_{ν_H} = 370 MeV
(f)
m_{ν_H} = 400 MeV
(g)
m_{ν_H} = 450 MeV
(h)
m_{ν_H} = 470 MeV
Acceptance
ν_H Energy (GeV)

Figure 4.5

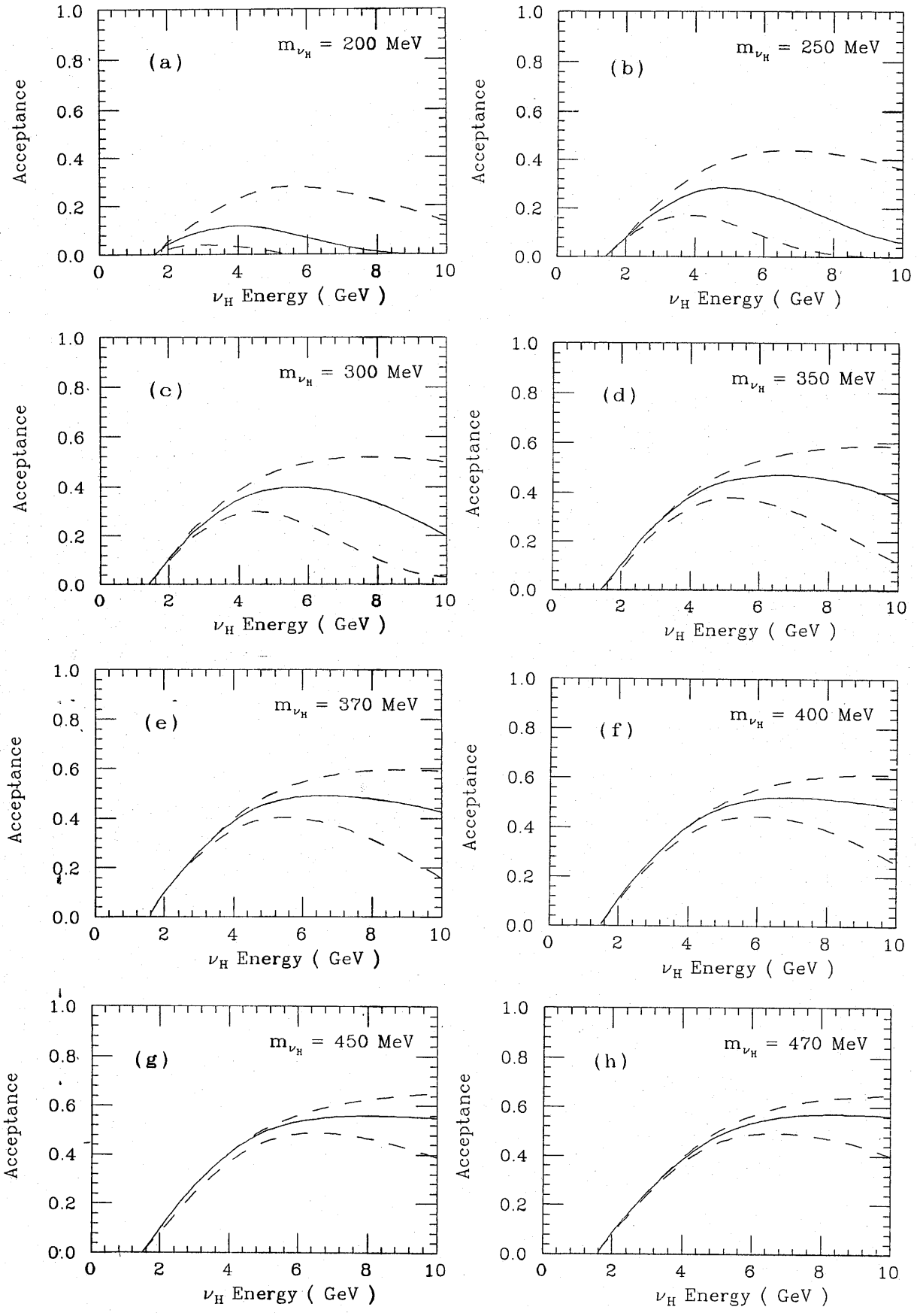
(a)
m_{ν_H} = 200 MeV
(b)
m_{ν_H} = 250 MeV
(c)
m_{ν_H} = 300 MeV
(d)
m_{ν_H} = 350 MeV
(e)
m_{ν_H} = 370 MeV
(f)
m_{ν_H} = 400 MeV
(g)
m_{ν_H} = 450 MeV
(h)
m_{ν_H} = 470 MeV
Acceptance
ν_H Energy (GeV)

Figure 4.6

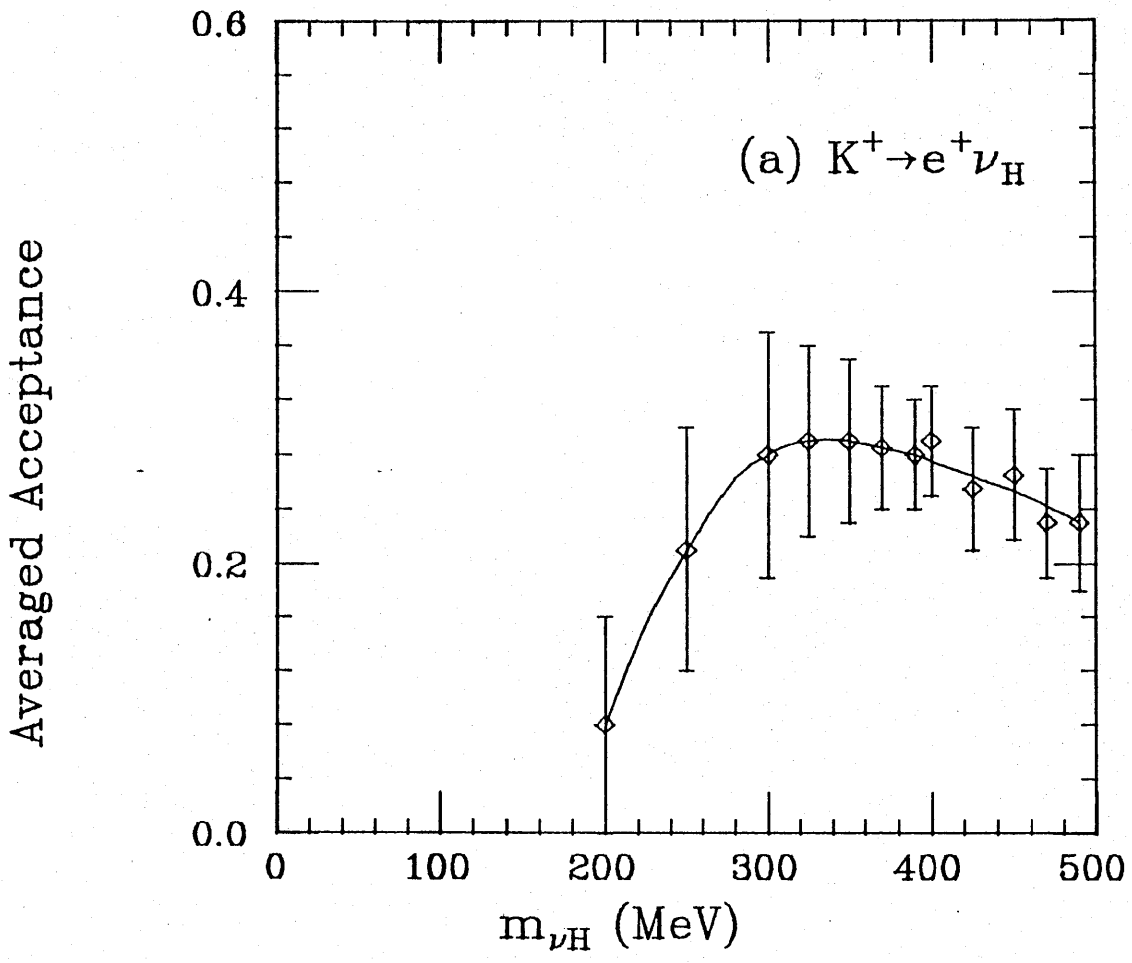
0.6
0.4
0.2
0.0
(a) $K^+ \to e^+ \nu_H$
Averaged Acceptance
0
100
200
300
400
500
$m_{\nu H}$ (MeV)

Figure 4.7

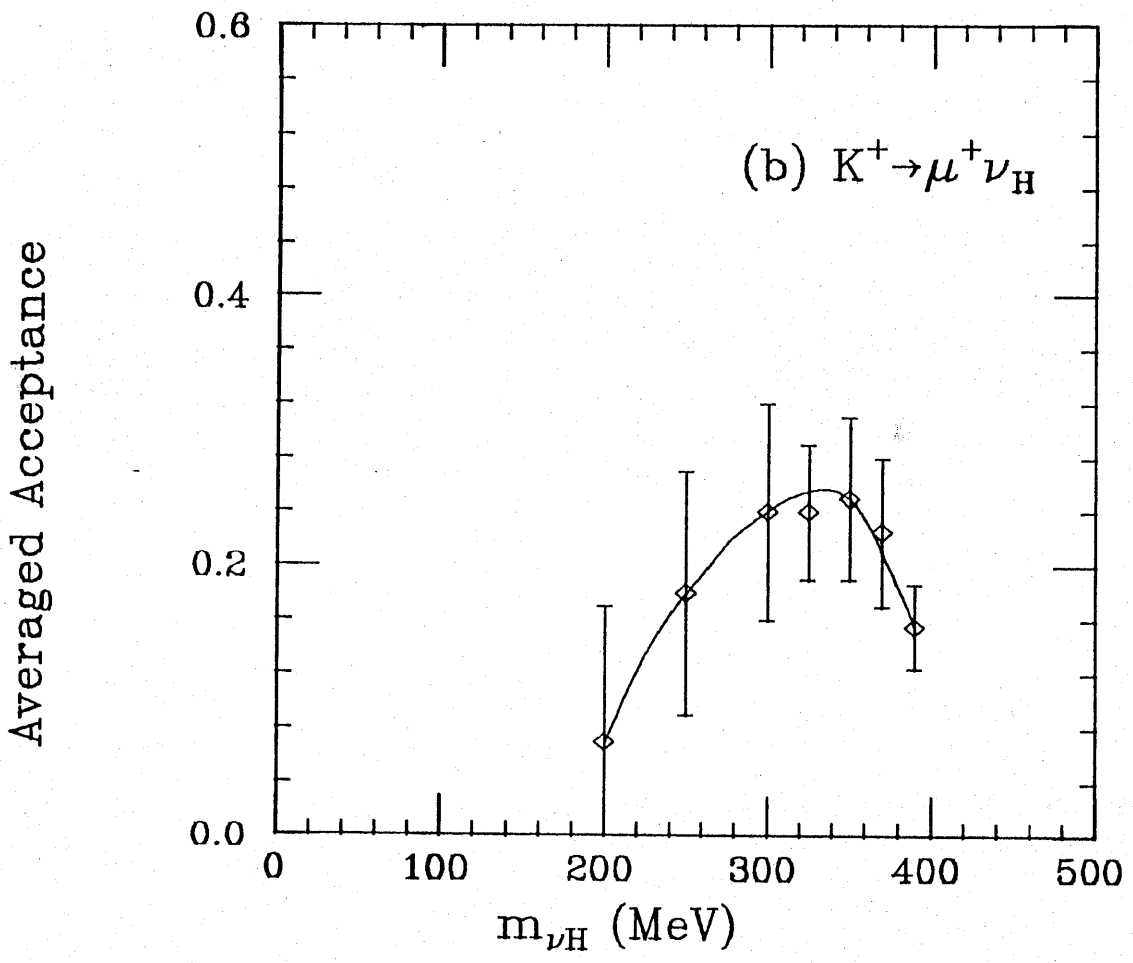
0.6
0.4
0.2
0.0
(b) $K^+ \to \mu^+ \nu_H$
Averaged Acceptance
0
100
200
300
400
500
$m_{\nu H}$ (MeV)

Figure 4.7

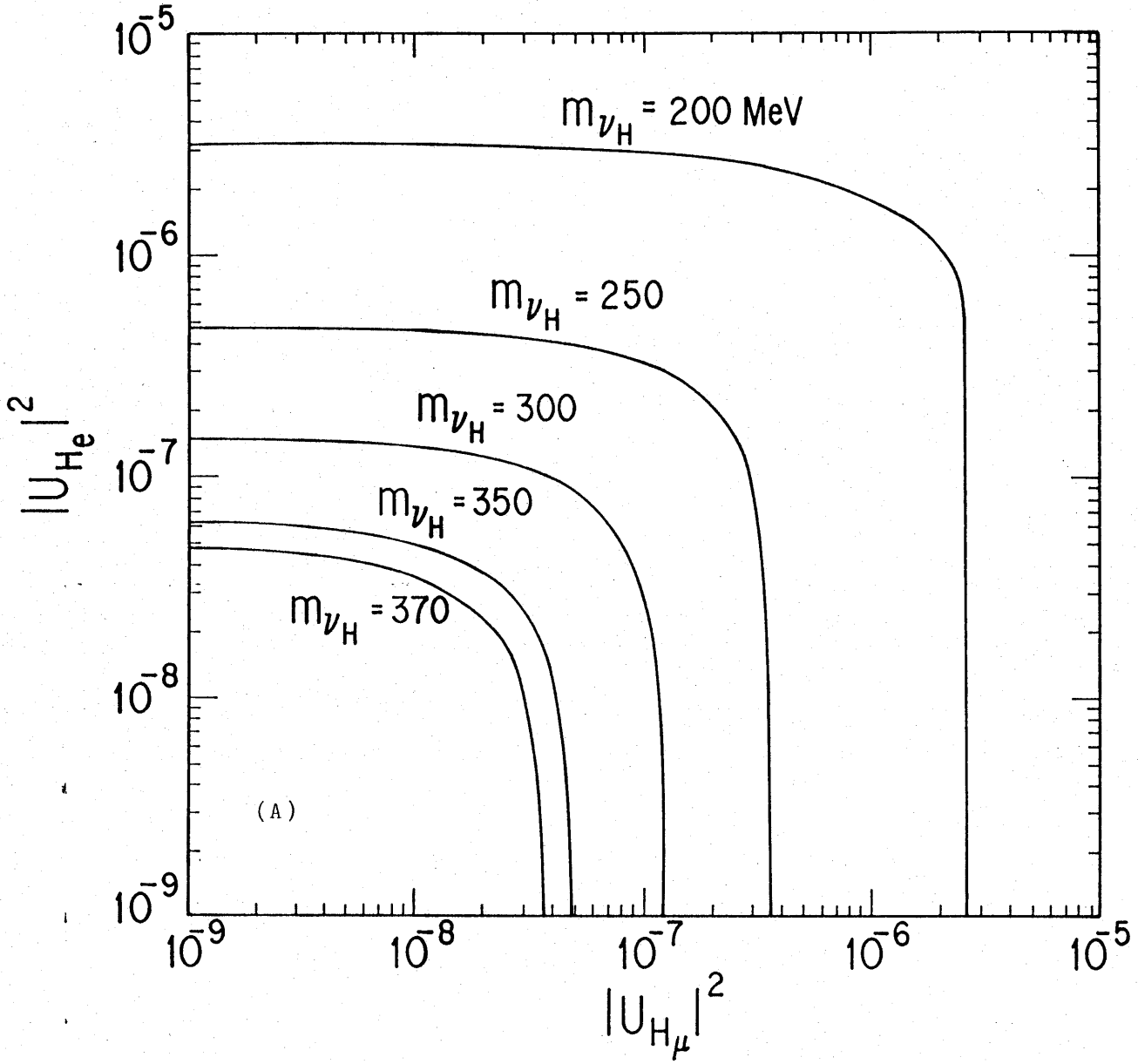
10^{-5}
10^{-6}
10^{-7}
10^{-8}
10^{-9}
$|U_{He}|^2$
m_{ν_H} = 200 MeV
m_{ν_H} = 250
m_{ν_H} = 300
m_{ν_H} = 350
m_{ν_H} = 370
(A)
10^{-9}
10^{-8}
10^{-7}
10^{-6}
10^{-5}
$|U_{H\mu}|^2$

Figure 4.8

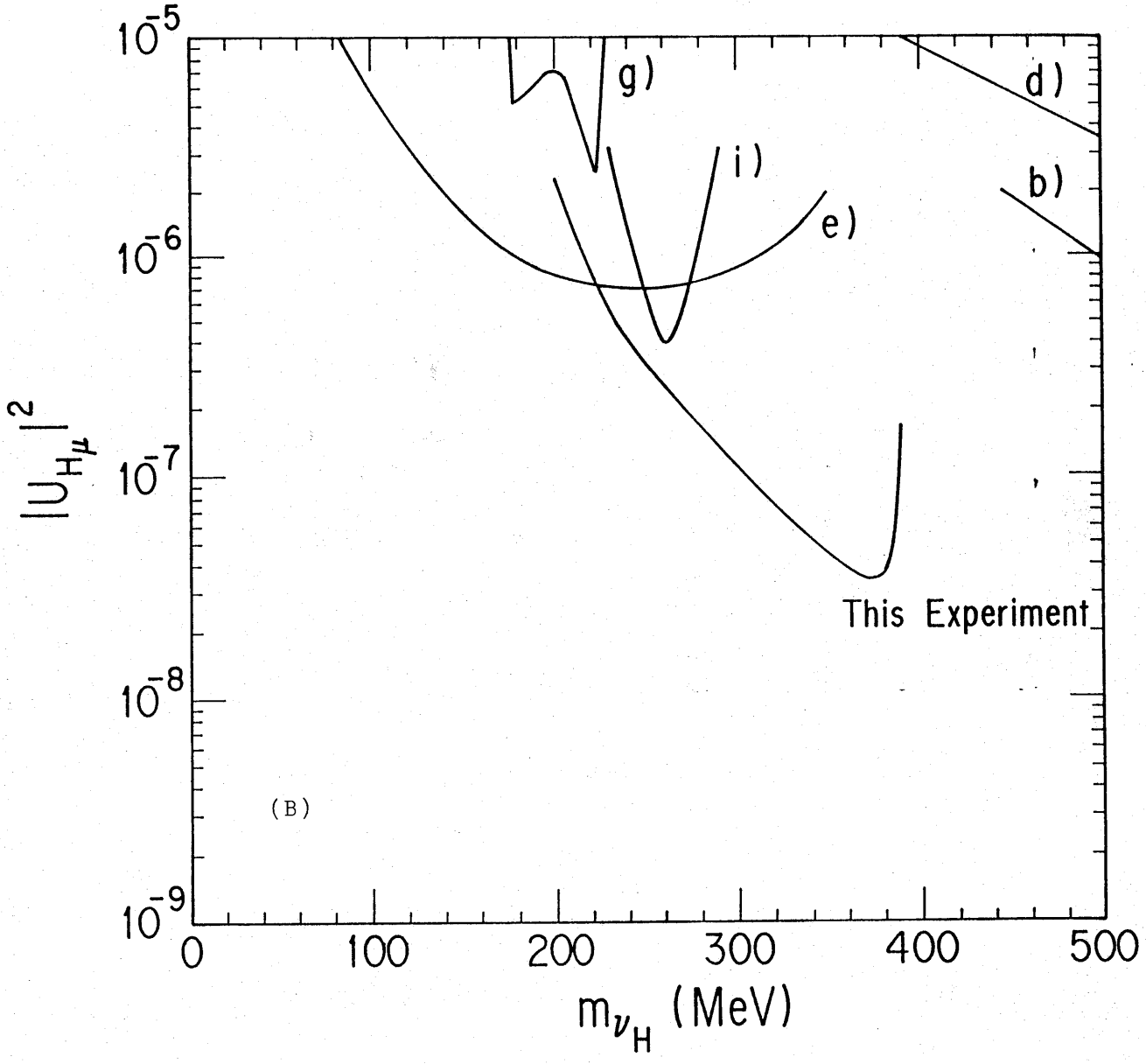
10^{-5}
10^{-6}
10^{-7}
10^{-8}
10^{-9}
$|U_{H\mu}|^2$
g)
d)
i)
b)
e)
This Experiment
(B)
0
100
200
300
400
500
m_{ν_H} (MeV)

Figure 4.8

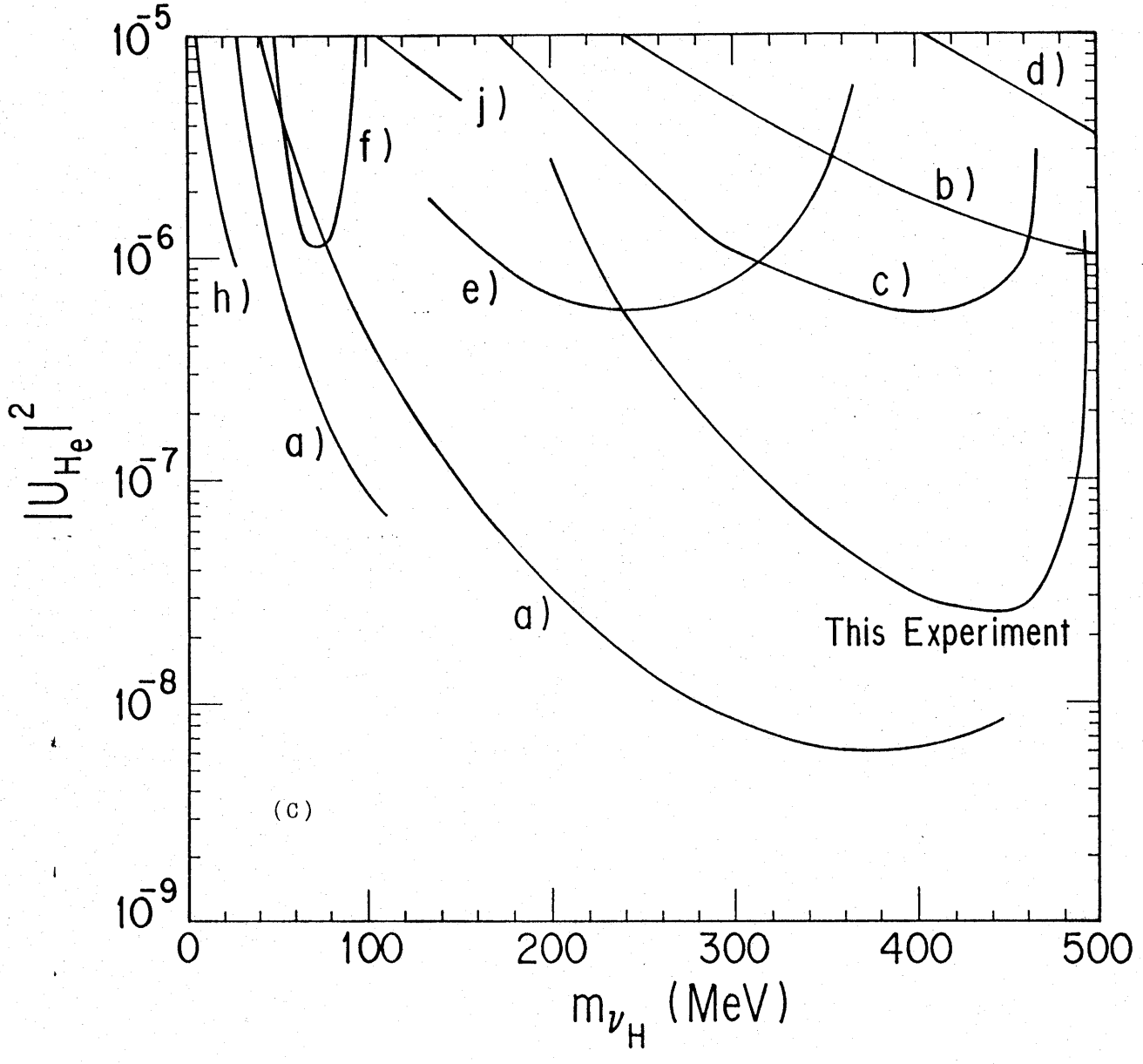
10^{-5}
10^{-6}
10^{-7}
10^{-8}
10^{-9}
$|U_{He}|^2$
0
100
200
300
400
500
m_{ν_H} (MeV)
a)
a)
b)
c)
d)
e)
f)
h)
j)
This Experiment
(c)

Figure 4.8